INVESTIGATIONS OF SURFACE AND SUBSURFACE INITIATED FAILURES OF ROLLING CONTACT FATIGUE

by

Zamzam Golmohammadi

A Dissertation

Submitted to the Faculty of Purdue University

In Partial Fulfillment of the Requirements for the degree of

Doctor of Philosophy

Department of Mechanical Engineering

West Lafayette, Indiana

May 2020

THE PURDUE UNIVERSITY GRADUATE SCHOOL
STATEMENT OF PRELIMINARY REPORT APPROVAL

Dr. Farshid Sadeghi, Chair

Department of Mechanica Engineering

Dr. Marisol Koslowski

Department of Mechanical Engineering

Dr. Charles M. Krousgrill

Department of Mechanical Engineering

Dr. Rodney Trice

Department of Materials Engineering

Approved by:

Dr. Nicole L. Key

This dissertation is dedicated

to my parents

Zahra Shapoori and Sadrollah Golmohammadi

and my husband

Mehdi Jokar

ACKNOWLEDGMENTS

First of all, I would like to thank my major advisor Professor Farshid Sadeghi for providing me the astonishing opportunity to join his laboratory and work on challenging projects. He has guided me through difficulties in both my professional and personal life. I would also like to thank Prof. Marisol Koslowski, Prof. Charles Krousgrill, and Prof. Rodney Trice for serving on my advisory committee.

I would like to thank all my past and present friends at Mechanical Engineering Tribology Laboratory (METL) for their help and support. They provided a productive and friendly environment to work. I would especially like to thank Aditya Walvekar for his discussion and input during my work in METL.

I would like to thank Dr. Kuldeep Mistry and Dr. Young Kang from Timken Company for their financial support and interest in this work.

I would like to express my gratitude to my family specially my parents. They have always been the strongest support to me and they deserve my deepest appreciation for their love, devotion, and sacrifices.

Last but certainly not least, I'd like to thank my amazing husband, Mehdi, for his love, support, and patience.

TABLE OF CONTENTS

LIST OF TABLES

LIST OF FIGURES

NOMENCLATURE

Symbol	Units	Description
E	GPa	Elastic modulus
E'	GPa	Equivalent stiffness
H	GPa	Hardening modulus
ν		Poisson's ratio
S_y	GPa	Yield Strength
S_{us}	GPa	Ultimate strength in shear
σ	GPa	Stress
σ_{max}	GPa	Maximum von Mises stress over a fatigue cycle
σ_m	GPa	Mean stress due to the presence of residual stresses
$\Delta\tau$	GPa	Shear stress range along the Voronoi grain boundaries
τ_0	GPa	maximum orthogonal shear stress
z_0	μm	Depth of τ_0
τ_{r0}	GPa	Resistance stress
m		Material parameters
S_0	GPa	Material parameters
q		Material parameters
τ_f	GPa	Fatigue strength coefficient
$-\frac{1}{B}$		Fatigue strength exponent
H_v	Kgf/mm^2	Vickers hardness
ε^P		Plastic strain
$\dot{p}$		Accumulated equivalent plastic strain over a fatigue cycle
P_{max}	GPa	Maximum Hertzian pressure
(x_c, y_c)	μm	the coordinate of the center of the Hertzian pressure
a	μm	Half contact width (3D model)
b	μm	Half contact width (2D model)
N	cycle	Number of Fatigue cycle

N_{ref}	cycle	Refurbished cycles
N_{crit}	cycle	Fully damaged fatigue cycle
L_{10}	cycle	Basic life rating
W	N	Applied load to the contact
P_a	N	Dynamic equivalent load
C_a	N	Basic dynamic load rating
D		Damage variable
μ_s		Coefficient of friction
D_w	μm	Ball diameter
Z_1		Number of balls
r	μm	Radius of spheres
D'	μm	Equivalent diameter
S_h	μm	Dent sharpness
P_r	μm	Pile up ratio
b_m		bearing type factor
f_c		a coefficient based on processing accuracy and material

ABSTRACT

Rolling contact fatigue (RCF) is a common cause of failure in tribological machine components such as rolling-element bearings (REBs). The two most dominant modes of RCF failure are surface originated pitting and subsurface initiated spalling, both of which have been studied in this investigation. Surface originated pitting is characterized by the initiation of a crack at a surface irregularity i.e. dents or scratches. In this study, a coupled multibody elastic-plastic Voronoi finite element (FE) model was developed based on the continuum damage mechanics (CDM) to investigate the effects of surface defects, such as dents on RCF. The contact pressure, internal stresses and strains were determined using the coupled FE model. The spall patterns and Weibull slopes obtained from the numerical model were found to be in good agreement with the experimental observations from the open literature. The results demonstrated that the sharper the edges and higher the pile-up of the dent profile caused higher pressure spikes and consequently reduced the RCF life.

Subsurface initiated spalling mechanism dominates when bearings are operated under clean lubricated conditions and smooth surface finishes. In this failure mode, micro-cracks originate below the surface at material inhomogeneities such as an inclusion and propagate towards the surface. The fatigue life due to the surface defects is shorter compared to subsurface initiated spalling. In order to allow bearings to reach their critical damage mode (subsurface initiated spalling) and useful estimated life, surface-originated damage in components of REBs can be repaired. In this study, the effects of refurbishing on RCF failure for case carburized bearing steel are experimentally and analytically investigated. A thrust bearing test apparatus (TBTA) was designed and developed to characterize the rolling contact fatigue behavior of different materials. The experimental results for the case carburized AISI 8620 steel demonstrated that the refurbishing process extended the fatigue life of the test specimens. It was also observed that the remaining useful life of the refurbished specimens was improved by increasing the depth of the regrinding. For the analytical investigation, a 2D elastic-plastic FE model was developed to predict the RCF life for pristine and refurbished specimens of case carburized steel using CDM. The effect of the carburizing process (e.g., variations in hardness and residual stresses) were incorporated in the FE model. A sectioning approach was used to simulate the point contact using the 2D model. The

analytical results for the pristine and refurbished case carburized steel corroborated well with the experimental results obtained from TBTA for different grinding depths.

The 2D RCF model was then extended to a 3D efficient elastic-plastic FE model to predict the RCF lives of through hardened AISI 52100 steel at high loading conditions. In order to simulate the RCF for high loads, variations of contact configuration observed in the experimental work were implemented in the 3D model. The experimental results using TBTA demonstrated that the track width increased during RCF cycles, which caused a reduction in the contact pressure due to plastic strains. The compressive residual stresses due to the plastic deformation were also incorporated in the damage evolution law. The estimated RCF lives of through hardened domains corroborated well with the experimental results at high load conditions.

The developed 3D efficient FE model was then extended to investigate the effects of refurbishing on RCF behavior of through-hardened bearing steel. In order to simulate the bearing refurbishment, a layer of the 3D material microstructure was removed from the top surface while the damage state of each element at a specific loading cycle prior to refurbishing was preserved as an initial damage value in the domain. The refurbished domains were then subjected to RCF cycles until a crack reached the top surface designated final fatigue life. In order to investigate the effects of the regrinding depth, fatigue cycles prior to refurbishing and applied loads on the fatigue failure of the through-hardened bearing steel in a circular contact, a parametric study was performed. The numerical results revealed that deeper refurbishing depth and greater fatigue cycles before refurbishment increased the total fatigue life.

1. INTRODUCTION

1.1 Background

Fatigue is the failure of machine components subjected to cyclic loads that are below the ultimate or yield strength of the material. In components such as rolling element bearings (REBs), gears, cam-followers, and rail-wheel contacts, rolling contact fatigue (RCF) is the major cause of failure. RCF is characterized by crack initiation and propagation caused by the alternating contact stresses over a small volume. Rolling contact fatigue manifests through various mechanisms that eventually lead to failure, however, surface originated pitting and subsurface initiated spalling are the predominant modes [1,2]. These prevailing failure modes in bearings and rotating machinery depends on surface quality, installation and maintenance, lubricant cleanliness, material quality etc. A comprehensive understanding of the fatigue process is crucial to predict life and mitigate damage so that components can be repaired or replaced before a catastrophic failure [3].

When contacting surfaces are smooth, free of defects and operate under clean lubricated conditions, subsurface originated spalling mechanism dominates [1,2]. This failure mode occurs when micro-cracks initiate below the surface at material inhomogeneities such as non-metallic inclusion and propagate towards the surface forming a relatively large spall. These cracks are mostly found to initiate in the region of maximum shear stress reversal below the surface [4]. Figure 1.1 depicts the subsurface initiated cracks in RCF.

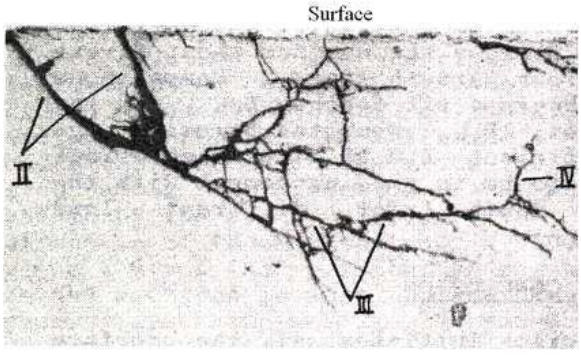

Figure 1.1: Subsurface initiated spalling in rolling contact fatigue [4]

In recent years, subsurface initiated spalling has significantly reduced due to major enhancements in lubrication cleanliness, materials and manufacturing processes [5]. However, surface-initiated pitting continues to persist in REBs. The most common cause of this failure is debris contaminations in lubricants. Rolling over debris through the contact causes indentations on the rolling surfaces. The resulting surface irregularities cause high stress concentrations which can lead to surface crack initiation. The surface cracks then propagate downward in the material at shallow angles [6]. When they reach a critical length or depth, the cracks branch up towards the free surface and form spalls leading to fatigue failure [7]. Mechanism of surface originated pitting is shown in Figure 1.2.

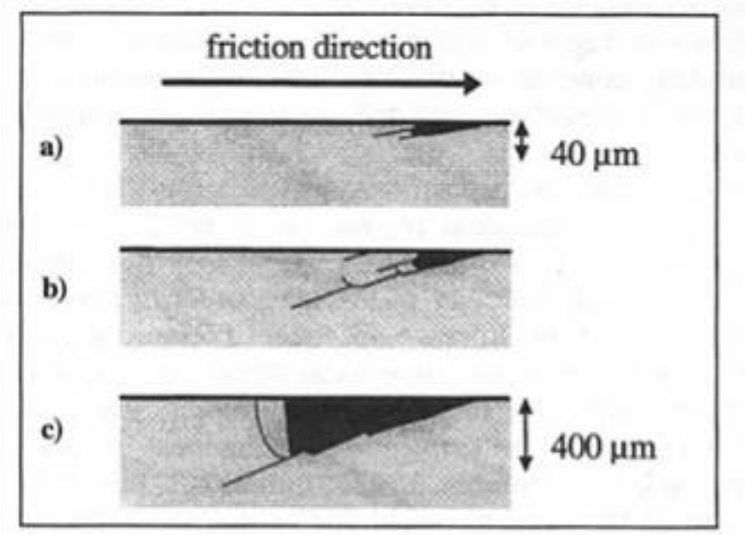

Figure 1.2: Mechanism of surface originated pitting [7]

1.2 Rolling Contact Fatigue vs. Classical Fatigue

The investigation of rolling contact fatigue is more challenging as compared to classical fatigue due to some key distinctions. The most important differences can be listed as,

1. In rolling contact fatigue, the state of stress at a point of material during a loading cycle is non-proportional. Contrary to classical fatigue, the stress components do not rise and fall in the same sequence of the applied contact load. Figure 1.3 demonstrates the stress history experienced by a material point at the maximum orthogonal shear stress during a contact

loading cycle. As can be seen, the shear stress is the only stress component which undergoes reversal, while normal stresses always remain compressive.

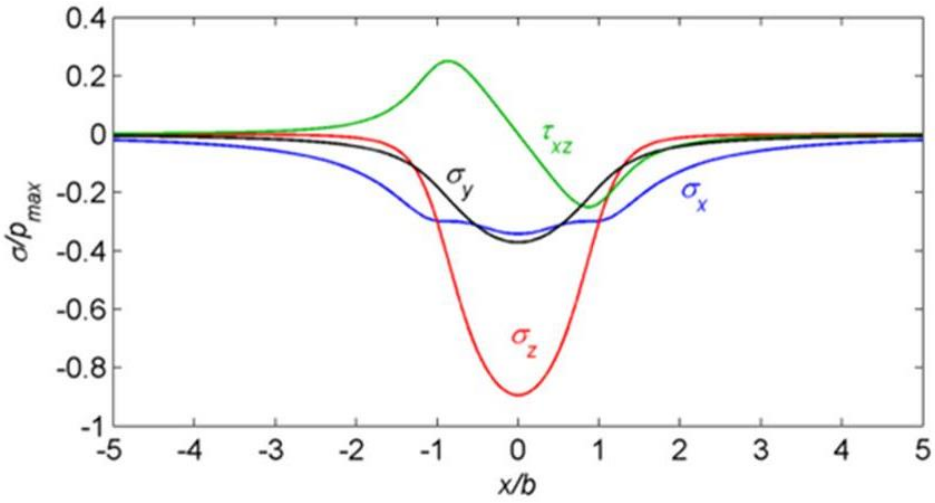

Figure 1.3: Stress history experienced by a material point at the maximum orthogonal shear stress as Hertzian line contact passes over the surface.

2. Contrary to most classical fatigue phenomena, RCF is typically a multi-axial fatigue mechanism. In non-conformal contacts, the state of stress is complex and multi-axial (Figure 1.3). The principal stresses below the central point of contact are governed by the Hertzian contact theory [7]. Furthermore, the directions of the principal stresses are constantly changed during the stress cycle. Consequently, planes subjected to critical levels of stress must be determined by considering the stress history during an entire RCF load cycle.

3. There is a significant compressive component of hydrostatic stress (Figure 1.3) in the rolling contacts which tends to inhibit Mode I crack growth. The crack propagation in RCF is dominated by mode II crack however, there is not sufficient information regarding how compressive hydrostatic stress affects this failure mode.

4. In classical fatigue testing, e.g. uniaxial or torsion fatigue, specimens are subjected to loadings that produce bulk stresses. Hence, a large volume of the material is damaged and failed. However, the stresses in RCF are highly localized within the non-conformal contact

regions, e.g. a rolling element on a bearing raceway. Typical bearing contact widths are on the order of 100 – 1000 μm. Consequently, the phenomenon of RCF occurs in a very small portion of the material.

5. The damage evolution of RCF leading to a fatigue spall involves localized plastic deformation and development of residual stresses, and therefore the ability to compute the stress fields that accounts for cyclic loading and traction effects, and acknowledge microstructural changes, is an essential tool to quantify RCF damage.

The above points are some of the reasons classical fatigue results cannot be directly translated to RCF. Therefore, many researchers have been interested in the investigation of the RCF phenomenon over the last century. The next section presents a review of RCF models for surface and subsurface initiated failures.

1.3 Review of RCF models for studying surface originated pitting

The mechanism of surface originated RCF failure under pure rolling conditions has been investigated in terms of the various surface defects such as debris dents, grinding furrows, handling nicks, surface inclusions, and peeling damage. These surface flaws act as points of stress concentration and produce locally intensified contact stress that lead to a surface crack. In order to propagate the point-surface-origin modes of damage, other factors besides surface defects are essential. The tensile stress on the contacting surfaces expedites surface crack propagation by opening the crack and allowing the lubricant to penetrate into the crack. In this failure mode, gross sliding with rolling contact can also cause an arrowhead-shaped spall.

Surface defects such as dents are one of the most common causes of surface originated pitting. When the smallest solid particle carried by the lubricant is larger than the film thickness, dents can be formed on the surface. These solid particles in the lubricant can appear from external sources such as the environment or internal sources such as component wear or manufacturing debris. The numbers of surface dents depend on the filter rating, sealing technology, and environmental cleanliness. All harmful particles cannot be removed from lubricant due to the compromise between filter performances, weight, size, and cost. Hence contact surfaces should be designed to resist surface dents.

The importance of lubricant cleanliness and the influence of solid particles in the lubricant on rolling contact fatigue has been studied over the years [5,8–15]. Tallian [16] was among the first to demonstrate the importance of lubricant cleanliness for bearing life both from experimental and theoretical aspects. Many experimental investigations [8–10,14,15,17,18] have been carried out to determine the role of contaminants on RCF life of bearings. The main conclusion from these studies was that the lubricant contamination has a detrimental influence on the bearing fatigue life. The life reduction will be dependent on the filtration level or the contaminant content. Many researchers [14,17,19–25] have also presented experimental results on the effects of artificial surface dents on RCF. Tallian [16,26] and Nelias et al. [25] indicated the effects of slide-to-roll ratio on the location where the spall was initiated in the presence of surface dent. Depending on the direction of the traction force, spall could initiate at the trailing or leading edges of the dent. Ueda and Mitamura [27] confirmed these findings and experimentally studied the mechanism of dent initiated flaking using ball-on-rod and twin-disk RCF test rigs. Dommarco et al. [28] demonstrated the influence of material pile up around an artificial dent on RCF life. In their study, RCF life was increased by a factor of two with the same failure mechanism after machining off the material pile up at the dent shoulders. Makino et al. [21] and Matsunaga [22] studied the effects of defect shape on RCF crack initiation and propagation. These studies indicated that the fatigue life decreased by increasing defects depth. Nelias and Ville [5,29] investigated the influence of debris dents shape and size on RCF failure and contact pressure distribution. Moreover, Coulon et al. [30] experimentally measured the pressure profile within the contacts using Raman micro-spectrometry. Furthermore, other experimental studies have been conducted for better understanding of the mechanism of generating debris dent, spall initiation and RCF failure under different operating conditions [24,31,32].

Many researchers [15,19,33–42] have investigated the changes in the pressure distribution and subsequent stress fields due to the debris dent for dry and elastohydrodynamic lubricated contacts. Ioannides and Harris [36] developed a model to predict the RCF life of bearings due to localized stresses in the dents region. Ko and Ioannides [37] proposed an elastic-plastic numerical model to analyze the subsurface stresses due to debris denting in bearing steel. In their analysis, the induced residual stresses due to indentation were calculated using the finite element method (FEM). However, the contact pressure used in their analysis was fixed as Hertzian and not calculated from contacting bodies. Therefore, the effect of plastic strain and subsequent hardening

due to indentation were neglected. Ai and Lee [35] and Ai and Cheng [43] studied sliding influence on spall formation. Howell et al. [44] studied a rolling contact over four differently sized dents using FE model. In this study, the influence of dent dimensions on the fatigue failure location and the pressure distribution were studied for dry contact. Their model simulated the rolling contact by repeating the pressure at a single point whereas in experiments, the roller moves continually along the path of rolling. Hence, the actual contact pressure distribution, internal stresses and strains, the material hardening, etc. were not accounted in the model.

In recent years damage mechanics has been extensively used by a number of investigators to study RCF [45–49]. Xu et al. [50–52] developed a finite element model based on the continuum damage mechanics to study dent-initiated spalling under rolling/sliding EHL conditions. In this model, plastic strain and residual stress due to indentation were neglected and no subsurface damage was included. Miller [53] demonstrated the influence of bearing steel material microstructure on early crack propagation and the significant scatter observed in RCF. Warhadpande et al. [54] presented a damage mechanics based Voronoi elastic finite element model to study the effects of dents and fretting wear in EHL line contacts. In order to determine the fatigue life and define a failure criteria for the effects of surface defects on RCF, a number of investigators [18,23,37] have suggested that the stress concentration at the dent shoulder is the cause for spall initiation. Johnson and Bower [55,56] postulated that plastic strain accumulations is the cause for spall initiation and propagation rather than the stress concentrations at the crack tip. As the plastic strains continue to increase due to cyclic loading, the micro-cracks continue to propagate causing a large scale rolling contact fatigue spall. Mura et al. [57] developed a crack initiation model based on the dislocation energy dipole approach. Cheng et al. [58] extended Mura's model and predicted fatigue life by correlating the model parameters with experimental results.

1.4 Review of RCF models for studying subsurface initiated spalling

Several experimental and analytical investigations have been conducted on characterizing the rolling contact fatigue behavior of materials. Over the past few decades, subsurface initiated spalling has been studied in more detail as compared to surface originated failure. The majority of the RCF subsurface models that have been developed can be classified as empirical, analytical and computational models (Sadeghi et al. [59]).

1.4.1 Empirical Models

The probabilistic empirical models provide a statistical characterization of RCF based on variables obtained from extensive full-scale bearing fatigue testing. One of the initial bearing life models which serves as the basis for the first bearing life standards [60] and many subsequent models for REBs was proposed by Lundberg and Palmgren [61,62]. They presumed that fatigue cracks originate from weak points of the material in the vicinity of maximum orthogonal shear stress. Assuming stochastic distribution of these material weak points by using the Weibull strength theory, Lundberg and Palmgren proposed the probability of survival, *S* for a particular stresses volume *V* of bearings subjected to *N* fatigue cycles

$$ln\frac{1}{S} \sim \frac{N^e \tau_0^c V}{z_0^h} \tag{1.1}$$

where τ_0 is the maximum orthogonal shear stress, z_0 is the depth of τ_0 and the parameters c, e and h are experimental material constants. The parameter e is the Weibull slope of the experimental RCF life data. Substituting actual bearing dimensions and applied load in Equation (1.1), a load-life equation was obtained which later became the basis of the first bearing life standard in the industry [60],

$$L_{10} = \left(\frac{C}{P}\right)^p \tag{1.2}$$

where L_{10} is the life cycles for 10% probability of failure, C is the bearing dynamic load rating, and P is the equivalent load on the bearing. The exponent p is 3 for ball bearings having elliptical contact area, 10/3 for roller bearings having modified line contact areas and 4 for pure line contacts.

Ioannides and Harris [14] proposed a new model to predict bearing lives in order to improve the Lundberg-Palmgren (LP) model with few modifications. They assumed fatigue crack initiation at any point in the material. Therefore, each discrete material volume will have its own survival probability. Consequently, the overall failure risk of the bearing is determined by integrating the failure risk over each volume. Furthermore, a fatigue limit was incorporated in the model which no bearing failure occurred below that threshold. The equation is given by

$$ln\frac{1}{S} = AN^e \int_{V_R} \frac{(\sigma - \sigma_u)^c}{z^h} dV\,, \quad \sigma > \sigma_u \tag{1.3}$$

where σ is the stress quantity occurring at depth z, σ_u is the stress threshold, and A is an empirical constant.

Using LP model (Equation (1.1)), it can be seen that the bearing life for a given survival probability S is related to the critical shear stress as;

$$\mathrm{N} \propto \frac{z_0^{h/e}}{\tau_0^{c/e} V^{1/e}} \tag{1.4}$$

This indicates that the effective stress-life exponent, *c/e*, depends on the dispersion in the fatigue life data. However, this relationship is in contradiction to exponents published in the literature. Therefore Zaretsky [63] modified the LP model [61] by eliminating the dependency of the stress-life exponent on the Weibull slope *e*, and also removing the depth parameter. In addition, the critical stress quantity is changed to the maximum shear stress. Zaretsky [63] equation is given as;

$$\ln\frac{1}{S} \sim \tau_0^{ce} N^e V \tag{1.5}$$

1.4.2 Analytical Models

In contrast to the empirical models, analytical life models [64,65] consider the physical mechanisms responsible for RCF. These models account for either crack initiation or crack propagation in order to predict the life. The first analytical model to study the RCF problem was developed by Keer and Bryant [66] who used fracture mechanics to estimate fatigue lives for rolling/sliding Hertzian contacts. Bhargava et al. [67] developed a model based on the accumulated plastic strain in strain hardening materials under cyclic contact. Cheng et al. [58] presented a micromechanical model based on the dislocation pileup theory to study crack initiation in the contact fatigue. It was assumed that the micro-cracks nucleated in slip bands located in material grains. Vincent et al. [68] proposed a similar model for crack initiation based on the dislocation pileup approach. Their model took into account the effect of all stress components and also incorporated residual stress effects. Lormand et al. [69] extended the Vincent et al. model

[68] to incorporate crack propagation according to Paris law. It was assumed that the crack propagation occurs due to shear stress (mode II propagation). The compressive stress component (σ_n) acting on the crack faces was taken into account by defining a Coulomb friction stress

$$\tau_{eff} = |\tau - c\sigma_n| \tag{1.6}$$

where c is a coefficient of friction and the value of 0.4 was selected although no justification was provided. Jiang and Sehitoglu [70] predicted RCF lives for crack initiation using the elastic-plastic finite element model that included the effects of cyclic ratcheting in conjunction with a multiaxial fatigue criterion. Total damage D was assumed to be the summation of fatigue damage (D_f) and ratcheting damage (D_r). It was found that the maximum of the total damage occurred at a depth of maximum orthogonal shear stress range, which is in agreement with the LP theory.

1.4.3 Computational Models

The analytical models are based on a homogeneous description of the material microstructure to predict RCF life. Since, the microstructural features are not directly included in these life prediction approaches, the stochastic nature of RCF cannot be captured. However, rolling contact fatigue lives of bearings are known to show dispersion due to the spatial scatter in material strengths, grain orientation, and inclusion distribution.

Raje et al [71] presented a statistical model to predict life dispersion in REBs by taking the material microstructure explicitly into account. The fatigue life (*N)* was assumed to be related to the critical stress (τ) and the corresponding depth (z)

$$N \sim \frac{z^r}{\tau^q} \tag{1.7}$$

The advantage of this RCF model was the independence on empirical Weibull regression parameters. Since this model incorporated the material microstructure characteristics, the variation in the critical stress τ and corresponding depth z caused the scatter in the fatigue lives. It was assumed that fatigue damage occurs along the weak planes (grain boundaries) and the plane which experiences the maximum shear stress reversal is the critical plane. This assumption is similar to several multi-axial fatigue criteria proposed in the literature [72–74].

This approach is limited to estimating relative life and does not obtain an absolute life for a particular domain. Raje et al. [75] further improved this limitation by incorporating a continuum damage mechanics to simulate the gradual material degradation under rolling contact fatigue. Damage was implemented through the internal damage variable D in the discrete element model through degradation of the springs. Damage evolution rate was assumed to occur according to an equation of the following form

$$\frac{dD}{dN} = \left[\frac{\Delta\tau}{\tau_r(1-D)}\right]^m \tag{1.8}$$

where $\Delta\tau$ is the critical stress range acting along the inter-element joint, τ_r and m are constant material parameters that are experimentally determined. Jalalahmadi and Sadeghi [76] developed the Voronoi finite element method (VFEM) based fatigue model. In this model, the randomness in the material microstructure is represented using Voronoi tessellation. They found that introducing heterogeneity in the material model by randomly distributing material flaws and varying the elastic properties enhanced the fatigue life scatter. Jalalahmadi [47] also improved the model by incorporating CDM to simulate the RCF similar to the mentioned model [75].

These RCF models utilized a two-dimensional simplification of the material microstructure. However, Weinzapfel et al. [77] extended the damage mechanics based RCF model by incorporating a 3D Voronoi Tessellation as a more realistic representation of the subsurface material topology. Since constructing the model in a three-dimensional framework increase the computational expenses; Bomidi et al. [78] implemented several strategies to enhance the computational efficiency of Weinzapfel's et al. [77] model. Further, Warhadpande et al. [79] and Bomidi et al. [80] included the effect of plasticity to accurately capture the stresses in the contact region under high loads in 2D and 3D RCF model.

1.5 Scope of this Work

As described earlier, many machine components are vulnerable to rolling contact fatigue. The complexity of the state of stress in the contact region makes the rolling contact fatigue study a challenging research task. Further, the progresses in steel production and processing techniques to enhance the fatigue life of the material bring new areas of research. Surface-originated damage in components of REBs plays an important role in RCF failure and fatigue life. However, these

defects can be repaired by regrinding the surface. In order to eliminate the aforementioned restrictions from previous studies and carry out an in depth analysis of surface and sub-surface initiated rolling contact fatigue spalling, the current work extends and improves the proposed fatigue models.

In Chapter 2, a coupled multibody Voronoi elastic plastic finite element model incorporating with damage mechanics approach is developed to study the effects of surface defects such as dents on RCF life. The residual stresses due to the debris denting process are also incorporated in the model. Further, a parametric study is conducted to study the effects of dent sharpness, pile up ratio and applied load on RCF life. In Chapter 3, the experimental and analytical investigations of the effects of refurbishing on RCF life for case carburized steel are studied. A thrust bearing test apparatus was designed and developed to simulate the RCF. On the other hand, a 2D elastic plastic FE model is developed to estimate the RCF life of pristine and refurbished case carburized domains. The analytical results are compared with experiments obtained from TBTA at two grinding depths. In Chapter 4, the 3D RCF model developed by Weinzapfel et al. [77] and Bomidi et al. [80] is modified by improving the computational efficiency. In order to predict the RCF life under high loading conditions, a variation of contact width observed in experiments, contact pressure, and also residual stresses due to the accumulation of plastic strains are incorporated in the model. In a continuation of Chapter 4, the efficient 3D RCF model is extended to study the effect of refurbishing on rolling contact fatigue behavior for the through-hardened material in Chapter 5. In this chapter, the refurbishing process is simulated by cutting the top layer of the 3D microstructure domain. A parametric study is conducted to evaluate the effects of refurbishing depths, fatigue cycles prior to refurbishing and applied loads. Finally, Chapter 6 provides a summary of major achievements of this work and proposed future work.

2. A COUPLED MULTIBODY FINITE ELEMENT MODEL FOR INVESTIGATING EFFECTS OF SURFACE DEFECTS ON ROLLING CONTACT FATIGUE

2.1 Introduction

Rolling contact fatigue is a common cause of failure in components such as rolling-element bearings (REBs), cam & followers, gears, etc. Well lubricated and properly maintained REBs will primarily fail due to RCF produced by alternating contact stresses [81]. There are two main modes of RCF failures, subsurface initiated spalling and surface originated pitting [1,2]. When bearings are operated under clean lubricated conditions and smooth surface finishes, subsurface originated spalling mechanism dominates [1,2]. This failure mode occurs when micro-cracks initiate below the surface at material inhomogeneities such as inclusion and propagate towards the surface forming a relatively large spall. In recent years, subsurface initiated spalling has significantly reduced due to major enhancements in lubrication cleanliness, materials and manufacturing processes [5]. However, surface-initiated pitting continues to persist in REBs. The most common cause of this failure is debris contaminations in lubricants. Over rolling a debris through the contact causes indentations on the rolling surfaces. These surface irregularities in the form of dents or scratches cause high stress concentrations which can lead to surface crack initiation. These surface cracks propagate downward in the material at shallow angles which form spalls leading to fatigue failure.

In the current analysis, a coupled multibody elastic plastic Voronoi FE model was developed based on the continuum damage mechanics to study the effects of surface dents on RCF life, spall initiation and propagation. The contact pressure and internal stresses and strains were obtained using the coupled multibody system. This allowed for accurate contact pressure and internal stresses due to different dents sizes, profiles and damage within the materials. The over rolling process of a debris in heavily loaded lubricated contact was modeled by pressing a rigid indenter on an elastic plastic substrate. The dent profile from the micro indentation process (i.e. different indentation depth, load, etc.) was then introduced on the surface of a semi-infinite elastic plastic finite element while the corresponding mating surface was rolled over the surface to determine the pressure between the bodies in contact. The Voronoi tessellation was used in the dented semi-infinite domain to capture the effects of microstructure topology in RCF simulation.

2.2 Modeling Approach

In this investigation, a 2D coupled multibody elastic plastic finite element model was developed to investigate the effects of surface defects on spall initiations, propagation and RCF life. In the following sections, microstructure model, FEM simulation of multibody system and the RCF continuum damage model based on accumulated plastic strains are described.

2.2.1 Coupled Finite Element Model

A 2D plane strain elastic plastic finite element model was developed using the commercially available ABAQUS software to simulate the contact between the roller and raceway in rolling element bearings. The multibody FE model was used to determine the contact pressure and the corresponding stresses, strains and damage during each over rolling process. Figure 2.1 illustrates the geometry of the equivalent contacting pristine (without dent) bodies and the corresponding dimensions. The contact between the roller and the semi-infinite domain was defined based on "master-slave" algorithm as described in ABAQUS. The Lagrange Multiplier approach was used to include the effects of friction between the contacting bodies. A friction coefficient of 0.05 was used to capture the condition for a well lubricated contact [82,83]. An over rolling pass was simulated by subjecting the semi-infinite domain to a rolling motion of the top body from -2.5b to 2.5b in 51 steps, where b is contact half-width.

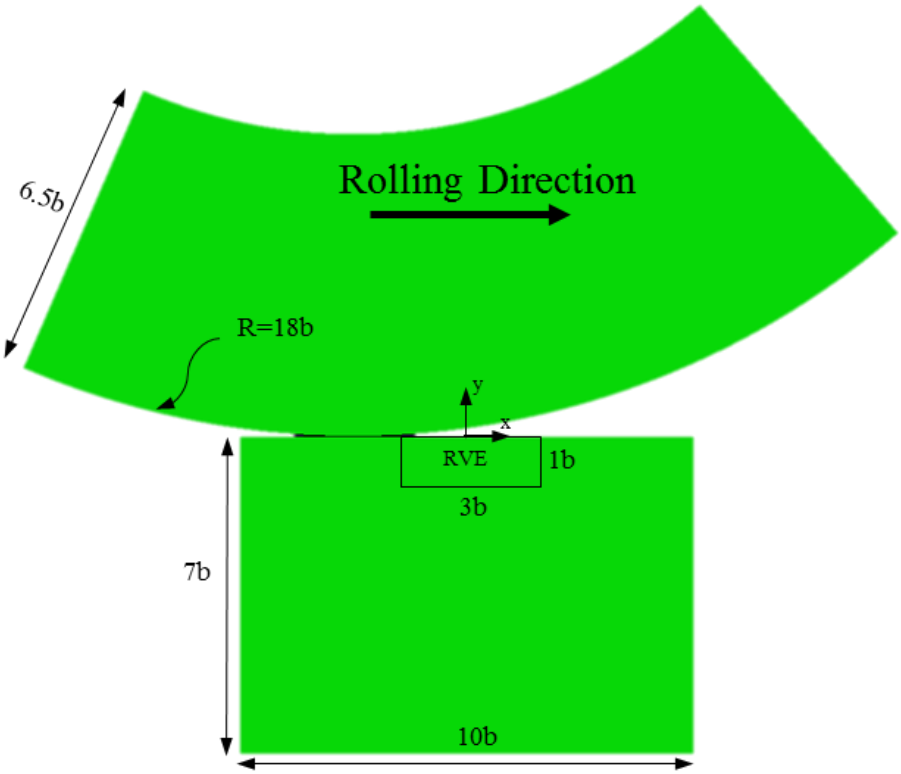

Figure 2.1: Geometry of roller and the flat domain in contact for RCF simulation (b is half contact width)

Figure 2.2 depicts the flowchart of the FE model developed for this investigation. The simulation starts with the discretization of the domain using Voronoi tessellation. The discretized domain was then used by ABAQUS to simulate a micro-indentation process. In this simulation, a rigid cylindrical indenter was pressed against a semi-infinite elastic plastic domain to generate a surface dent and induce plastic strains and residual stress due to indentation. After that, the roller (top body) was rotated over the top of the semi-infinite domain to simulate the rolling contact. The resulting contact pressures, stresses and accumulated plastic strains due to the dent was passed to the continuum damage mechanics model to update the damage variable for each element. This process was continued until a crack initiated and a spall propagated to the surface.

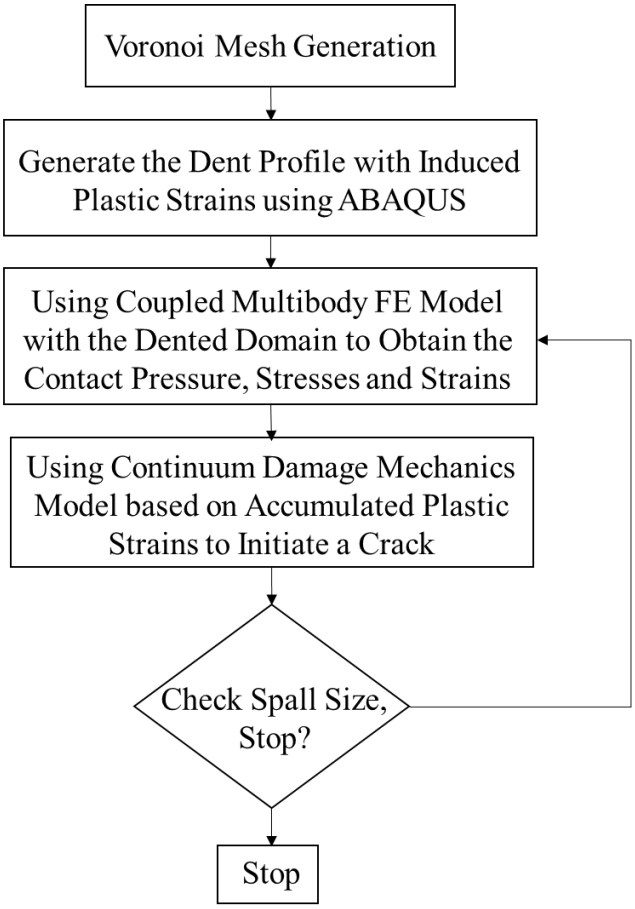

Figure 2.2: Flowchart for developed FE model with the effect of surface dent

2.2.2 Material Microstructure Topology

Voronoi tessellations have been widely used to simulate microstructure of polycrystalline materials [84,85]. This approach has been utilized in numerous investigations [47,86–91] to model fatigue life scatter. In the Voronoi tessellation, a set of seed points are randomly placed in the Euclidian space. The space is then divided into regions of material which are closest to a given seed point. These generated regions are called Voronoi cells. Voronoi cells and their boundaries represent the grain and grain boundaries respectively in the material microstructure [47,54,79,92]. To insure that the Voronoi microstructure matches the measurements of a typical bearing steel, the average diameter of Voronoi cells is set to a given mean grain size (i.e. 10 μm for steel) [47,75]. In order to reduce the computational efforts in the RCF simulation, the dimensions of the microstructure topology are confined to the representative volume element (RVE) [78,93]. The RVE is defined as the critically stressed area during a rolling pass. In this study, the Voronoi

tessellations were implemented only in the semi-infinite domain, the remaining regions beyond the RVE were meshed using a square Voronoi tessellations with constant strain tetrahedron (CST) elements.

2.2.3 Fatigue Damage Model

In the current study, continuum damage mechanics was used to describe the degradation of material due to micro crack initiation and propagation [45,46]. In CDM, fatigue failure is defined by the damage variable D. Damage variable D has a range between 0 (undamaged material) to 1 (fully damaged state). In this simulation it was assumed all the elements were undamaged at the beginning of simulation (first pass) and as the loading passes increased, the damage variable D gradually increased to reach a threshold level ($D_c = 1$). Then intergranular fatigue cracks were defined in the microstructure model at the grain boundaries using a Node release approach [54,78,94]. The cracks were propagated during RCF cycles and when the connected cracks reached to the surface from two ends, a spall was formed on the surface. Please note that, the elements inside the spall were removed from the simulation.

The evolution of damage at a material point is governed by an appropriate rate law. For elastic material, damage is only dependent on the state of stress. However, for elastic-plastic material, damage is dependent on the accumulated plastic strain. In this modeling, pressure spikes at the dent shoulder cause local stress concentrations and local plastic deformations while the rest of the domain behaves elastically. Hence, the von Mises plasticity model with linear kinematic hardening was employed in the FE model to incorporate the effects of material plasticity. For a detailed description about this plasticity model, please refer to [79,80,93]. Furthermore, the crack initiation due to the dent is a function of plastic strain [50,51,55,56]. Hence, two different damage rate laws are used in this model simultaneously.

Many researchers [36,95,96] have used the von Mises stress as a critical stress in fatigue life analyses. Furthermore, it is assumed that the grain boundaries constitute weak planes along which the fatigue damage can be advanced. The elastic damage evolution law [48,49] is defined as

$$\frac{dD}{dN} = \left[\frac{\sigma_{Mises}}{\sigma_{r0}(1-D)}\right]^{m} \tag{2.1}$$

where N is the number of cycle, σ_{Mises} is the maximum von Mises along the Voronoi grain boundary, σ_{r0} and m are material parameters that must be experimentally determined. σ_{r0} is the resistance stress [48] that represents the ability of a material to resist the damage accumulation.

The damage law based on the accumulation of plastic strain is given by [45]:

$$\frac{dD}{dN} = \left[\frac{\sigma_{\text{Mises}}^{2} R_v}{2ES_0(1-D)^2}\right]^{q} \dot{p} \tag{2.2}$$

where R_v is the triaxiality coefficient, $\dot{p}$ is the accumulated equivalent plastic strain over a fatigue cycle, S_0 and q are material dependent parameters, and E is the undamaged modulus of elasticity.

The triaxiality coefficient is defined as follows

$$R_v = \frac{2}{3}(1+\nu) + 3(1-2\nu)\left(\frac{\sigma_h}{\sigma_{Mises}}\right)^{2} \tag{2.3}$$

where σ_h is the hydrostatic stress over a fatigue cycle and ν is the Poisson ratio. The constant material parameters (σ_{r0}, m,S_0, and q) used in Equations (2.1) and (2.2) were determined using experimental torsional SN curve [47,79,80,88,93]. The torsion SN results for through-hardened AISI 52100 bearing steel [97] shown in Figure 2.3 was used in this model to evaluate the damage parameters.

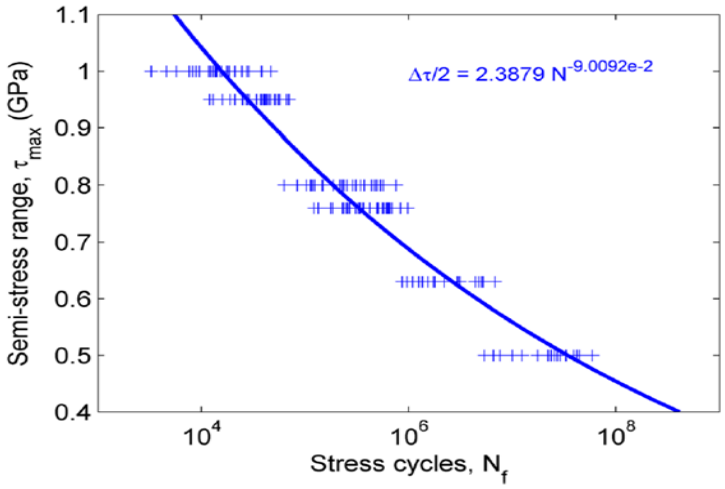

Figure 2.3:Experimental Torsion S-N data and power law fit to the data for through hardened bearing steel JIS SUJ2 (AISI 52100 variant) from [75]

As shown in Figure 2.3, torsional fatigue SN results closely follow Basquin's law. A power law fit in the form of Equation (2.4) was applied to the experimental data (Figure 2.3) in order to determine the Basquin parameters.

$$\frac{\Delta\tau}{2} = \tau_f N_f^{-\frac{1}{B}} \quad where\ \tau_f = 2.3879\ GPa\ \ and\ \ B = 11.099 \tag{2.4}$$

where $\Delta\tau$ is the shear stress range, N_f is fatigue cycles, τ_f is fatigue strength coefficient and $\left(-\frac{1}{B}\right)$ is fatigue strength exponent.

The von Mises stress in terms of state of stress at a point is given as;

$$\sigma_{Mises} = \left(\frac{1}{2}[(\sigma_{11}-\sigma_{22})^2 + (\sigma_{22}-\sigma_{33})^2 + (\sigma_{33}-\sigma_{11})^2 + 6(\sigma_{23}^2+\sigma_{31}^2+\sigma_{12}^2)]\right)^{\frac{1}{2}} \tag{2.5}$$

The stress tensor for the torsional fatigue test in terms of shear stress reversal ($\Delta\tau$) can be written as;

$$\sigma = \begin{bmatrix} \sigma_{11} & \sigma_{12} & \sigma_{13} \\ \sigma_{21} & \sigma_{22} & \sigma_{23} \\ \sigma_{31} & \sigma_{32} & \sigma_{33} \end{bmatrix} = \begin{bmatrix} 0 & \frac{\Delta\tau}{2} & 0 \\ \frac{\Delta\tau}{2} & 0 & 0 \\ 0 & 0 & 0 \end{bmatrix} \tag{2.6}$$

Substituting from Equation (2.6) in Equation (2.5), the equivalent von Mises stress can be written as;

$$\sigma_{Mises} = \sqrt{3}\,\tau = \frac{\sqrt{3}\Delta\tau}{2} \tag{2.7}$$

Now by substituting Equation (2.7) in Equation (2.4), the equivalent Basquin's law in terms of von Mises stress is obtained.

$$\sigma_{Mises} = \sqrt{3}\,\tau_f N_f^{-\frac{1}{B}} \tag{2.8}$$

Integrating the elastic damage rate law (Equation (2.1)) from undamaged state (*N = 0* and *D = 0*) to fully damaged state (*N = N_f* and *D = 1*):

$$N_f = \frac{1}{m+1}\left[\frac{\sigma_{r0}}{\sigma_{Mises}}\right]^m \quad \rightarrow \quad \sigma_{Mises} = \sigma_{r0}\left[\frac{1}{m+1}\right]^{\frac{1}{m}} N_f^{-\frac{1}{m}} \tag{2.9}$$

Equating Equations (2.8) and (2.9), the material parameters (σ_{r0}, m) for the elastic rate law can be obtained.

$$m = B \quad , \quad \sigma_{r0} = \sqrt{3}\tau_f (B+1)^{\frac{1}{B}} \tag{2.10}$$

In order to calculate S_0 and q for plastic damage rate law (Equation (2.2)), the same approach was used. The Equation (2.2) was integrated from an undamaged state to a fully damaged state and then equated with Equation (2.8), we obtain;

$$\sqrt{3}\left(\tau_f N_f^{-\frac{1}{B}}\right) = \frac{\left(\frac{2ES_0}{R_v}\right)^{1/2}}{[2(2q+1)\Delta\varepsilon_p]^{1/2q}} N_f^{-1/2q} \tag{2.11}$$

Here, $\Delta\varepsilon_p$ in Equation (2.11) is the range of plastic strain corresponding to σ_{Mises} over one fatigue cycle [45]. $\Delta\varepsilon_p$ can be determined in terms of σ_{Mises} , yield strength S_y and the hardening modulus H as shown in Figure 2.4 [93]:

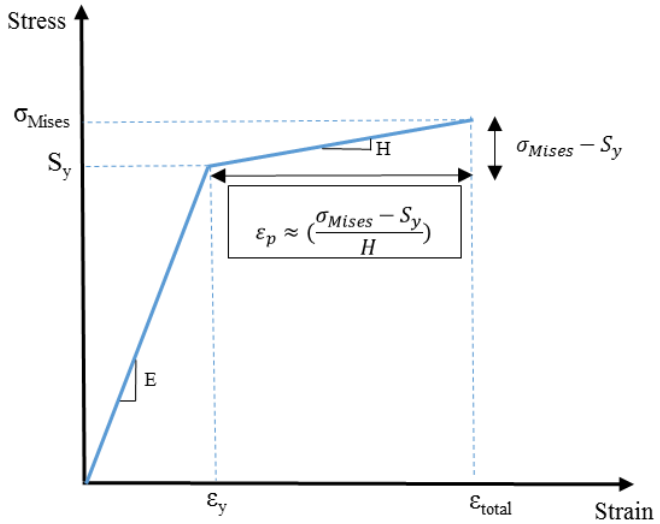

Figure 2.4: Bilinear profile of cyclic stress strain curve to calculate plastic strains corresponding to applied stresses over one fatigue cycle ($\Delta\varepsilon_p$)

$$\Delta\varepsilon_p = 2\left(\frac{\sigma_{Mises} - S_y}{H}\right) \tag{2.12}$$

Please note that the hydrostatic stress is zero in torsion fatigue test, therefore the triaxiality coefficient can be written as $R_v = \frac{2}{3}(1+\nu)$. Furthermore, plastic strain is observed in the low cycle fatigue regime, thus two different values for N_f ($N_1 = 10$ and $N_2 = 1000$) were chosen from this portion of SN curve. Substituting these two cycles in Equation (2.11) and dividing these equations to eliminate S_0, we obtain

$$q = \frac{B}{2}\,\frac{ln\left(\frac{N_2\Delta\varepsilon_{p_2}}{N_1\Delta\varepsilon_{p_1}}\right)}{ln\left(\frac{N_2}{N_1}\right)} \tag{2.13}$$

The value of S_0 can be obtained by substituting q into Equation (2.14)

$$S_0 = \frac{\frac{2}{3}(1+\nu)\sigma_{Mises1}^2\left[2(2q+1)\Delta\varepsilon_{p_1}N_1\right]^{\frac{1}{q}}}{2E} \tag{2.14}$$

Please note that, at the chosen cycles ($N_1 = 10$ and $N_2 = 1000$), the von Mises stresses are always higher than yield strength, therefore the calculated plastic strains is always a positive constant value for these cycles. The calculated material parameters of AISI 52100 steel are listed in Table 2.1.

Table 2.1: Material damage parameters for AISI 52100 steel evaluated using Torsion SN data (Figure 2.3)

Material property	Value
Material grain diameter (μm)	10
Elastic modulus (GPa)	200
Poisson's ratio	0.3
Hardening modulus (GPa)	10
Yield Strength (GPa)	2.06
σ_{r0} (GPa)	5.18
m	11.1
S_0 (GPa)	0.0641
q	3.2

The damage rate law equations (Equations (2.1) and (2.2)) and constitutive relationships are required to solve simultaneously for each element in RCF modeling. In present investigation, the jump-in-cycles procedure developed by Lemaitre [45] was utilized. In this method, the material damage state and the stress-strain response of the model were assumed to be constant over a block of cycles. The specific details of this method can be found in [47,79,80,88]. Furthermore, the detailed description of numerical implementation of damage rate law equations and RCF life calculation are fully described in previous studies [47,75,79,87].

2.3 Results and Discussion

The coupled multibody FE model was developed to determine the contact pressure, subsurface stresses and strains to investigate the RCF life of REBs. Figure 2.5 illustrates a Voronoi domain with a surface dent. This domain is used in the rolling contact simulation to calculate the contact pressure and accumulated plastic strains due to the dent.

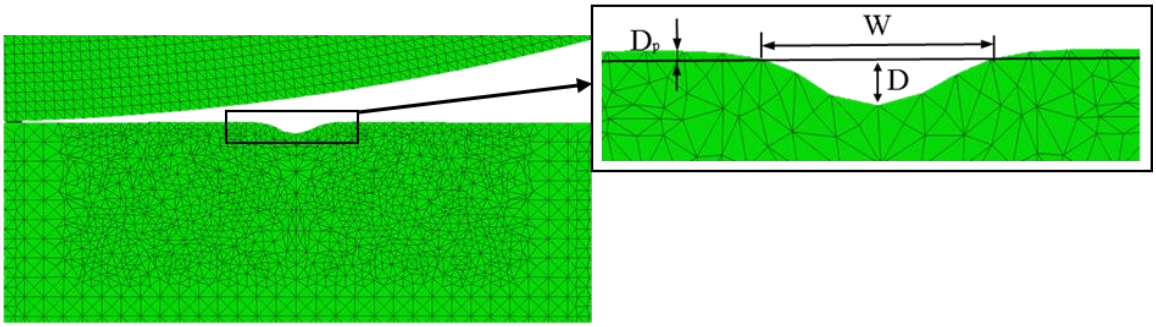

Figure 2.5: A dented Voronoi domain using indentation simulation

Figure 2.5 illustrates the dent dimensions, the depth, width and pile up for the dent are $D = 11.3\mu m$, $W = 61\mu m$ and $D_p = 1.08\mu m$, respectively. Table 2.2 lists the details of the simulation parameters.

Table 2.2: Simulation parameters of surface failure

Modeling parameter	Value
Domain width (μm)	1250
Domain depth (μm)	875
Roller radius (μm)	2747.25
Indenter diameter (μm)	50
Maximum contact pressure (GPa)	2.5
Half contact width (μm)	125

Figure 2.6 depicts the pressure distribution as the roller is rotated over the smooth and dented undamaged domains. As depicted in Figure 2.6a, the contact pressure is Hertzian and the

maximum contact pressure is 2.5 GPa for the smooth undamaged domain. Figure 2.6b illustrates the pressure distribution as the roller moves closer to the dent and when it is positioned directly above the dent. Note when the roller is positioned over the dent two pressure spikes are generated at the location of material pile up. These spikes are direct function of the dent size and material pile up.

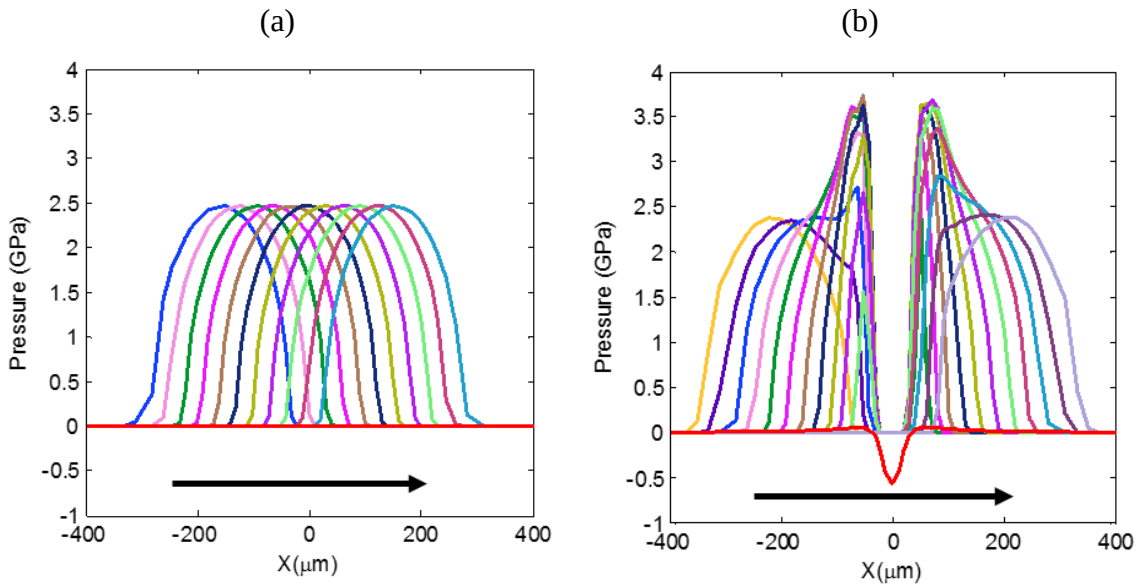

Figure 2.6: The obtained contact pressure distribution over RVE for the first cycle from multibody FE model for (a) Voronoi domain without a dent, (b) dented Voronoi domain

Figure 2.7 depicts the individual pressure distributions for different position of the roller relative to the dent. This figure is included to provide a clear description of pressure variation during an over-rolling process.

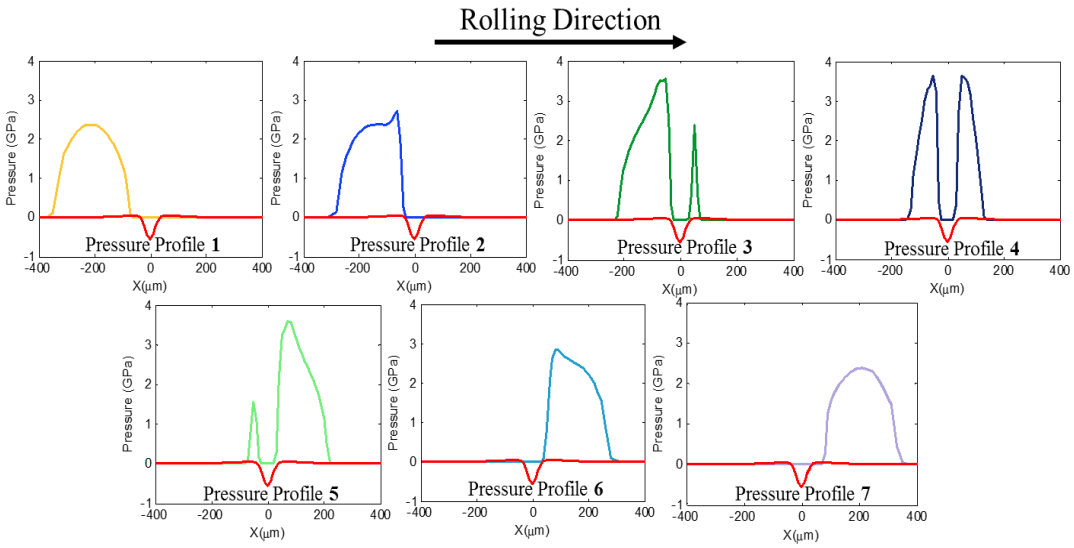

Figure 2.7: The contact pressure distribution for the first cycle as the roller moves over the dent

The von Mises stress and the accumulated plastic strains due to contact pressure profiles for pristine (undamaged) and dented surfaces are demonstrated in Figure 2.8. The maximum stresses and plastic strains in the dented domain occur on or close to the surface because of these high pressure spikes. No plastic strain is accumulated in the pristine domain for the identical applied load. The reason is the maximum von Mises for the first cycle in the pristine domain is 1.49 GPa, however, this value for the dented domain is 2.11 GPa. Where the yield strength of the material is 2 GPa.

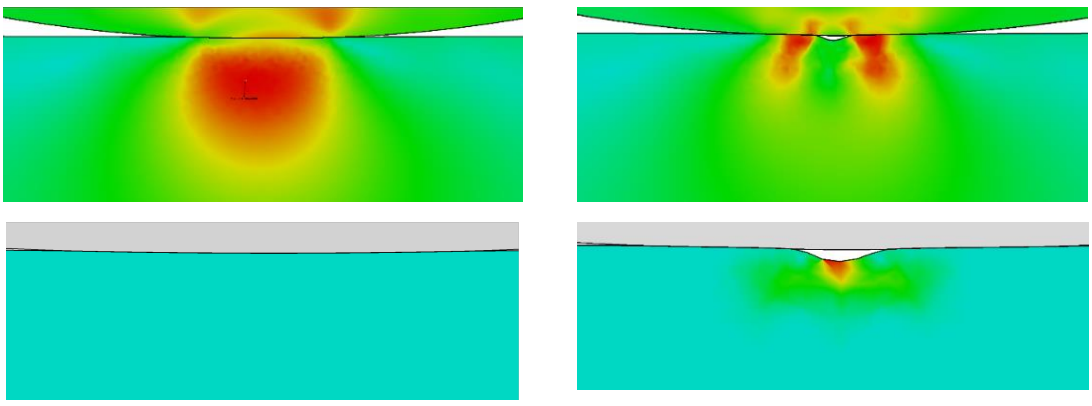

(a) (b)

Figure 2.8: The von Mises stress and accumulated plastic strains for (a) smooth Voronoi domain, (b) dented Voronoi domain

High pressure spikes along with the surface traction lead to initiate a spall close to the dent shoulder. Figure 2.9 shows the spall formations and corresponding plastic strains with increasing number of rolling contact cycles. Due to the accumulated plastic strains and high von Mises stresses near the dent, the first damaged element occurs on the surface next to the dent shoulder, hence a crack initiates (pass 10 in Figure 2.9). The cycle at which the first crack occurs is considered the initiation life. As the loading cycles increase, cracks propagate and reach surface from two ends therefore a small spall forms next to the dent (pass 20 in Figure 2.9).

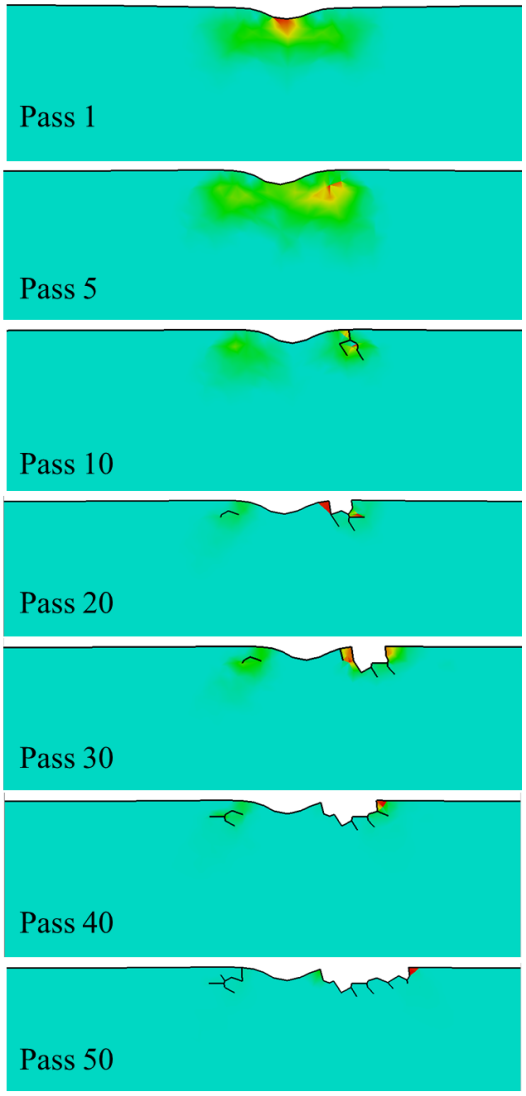

Figure 2.9: Spall initiation and propagation with corresponding plastic strains for different passes

The damaged elements form a spall and thus are removed from the computational domain, hence, the contact pressure will be affected by the modified surface profile and cause additional spalls. Figure 2.10 illustrates the contact pressure profiles and von Mises stress for these passes.

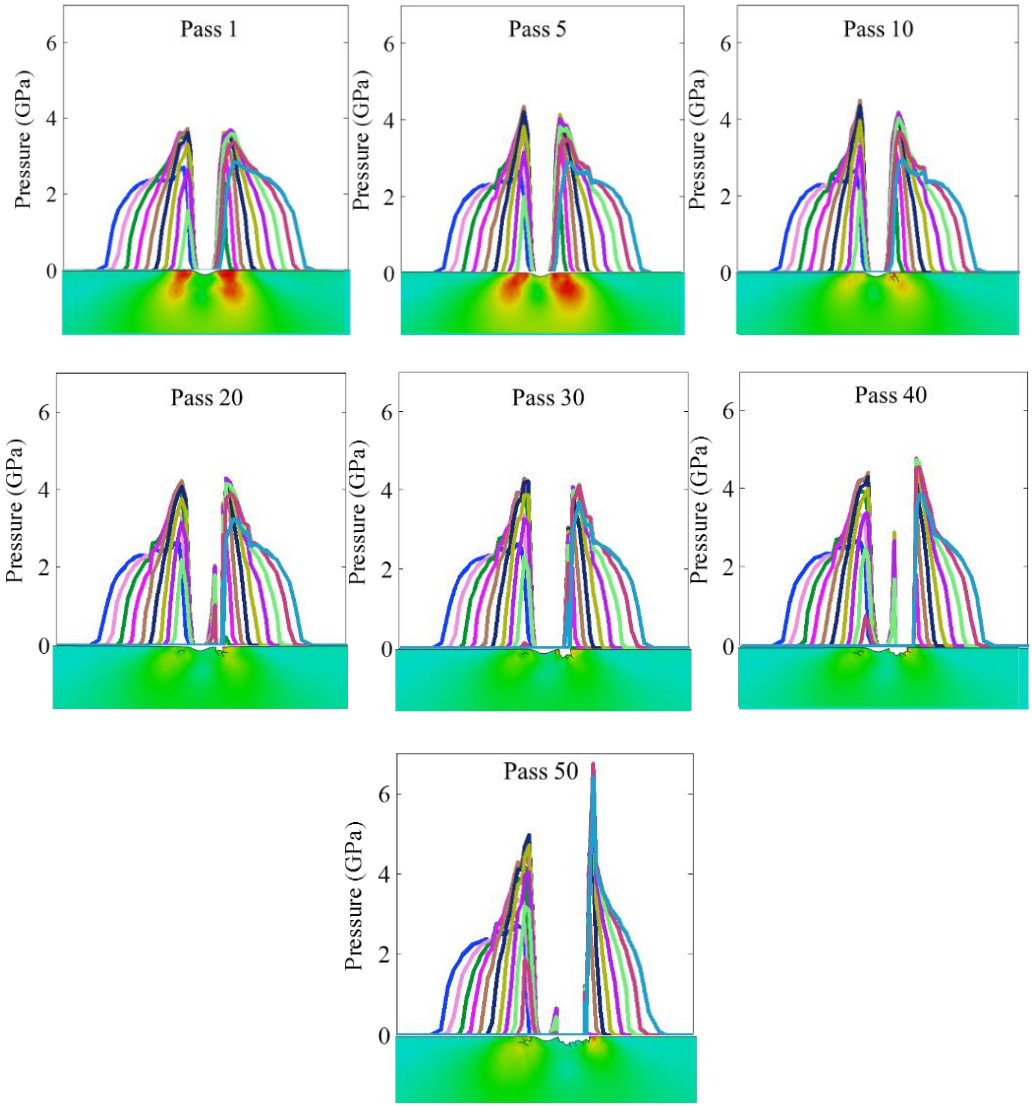

Figure 2.10: Contact Pressure and corresponding von Mises stress when roller moves over the dent for a different cycles (spall propagation)

Please note that the contact pressure profile at the dent edges is changed as compared to that in Figure 2.6 (pass 1 in Figure 2.10). These variations have occurred due to the damage propagations and spall formations around the dent profile. Also, note that the spall has formed on the trailing edge of the dent and no spall is initiated at the leading edge. When the upper body is

rolled over the dented surface, the edge of the dent which enters the contact first is referred to as "the leading edge of the dent" and the edge that comes in the contact last is "the trailing edge of the dent" [50,51]. For the current simulation, the roller rolled over the dented surface in the positive X-direction from -2.5b to +2.5b. Furthermore, the dent is located on the driven surface and the friction force acts on the semi-infinite domain in the positive X-direction. If the dent is situated on the driven surface, a spall forms in the direction of friction on the trailing edge of the dent [50,51,54]. Therefore, the numerical results obtained from the current developed model are in a good qualitative agreement with the experimental and numerical observations from the literatures.

In the current study, the spall initiation life was investigated for different dent sizes and applied loads. Thirty-three different microstructural domains were randomly generated using the Voronoi tessellation procedure to determine the RCF lives for different dent sizes. In the indentation simulation, a rigid indenter with the diameter of 50 μm was pressed against a smooth elastic plastic semi-infinite domain. Table 2.3 contains the generated dent dimensions.

Table 2.3: Dent dimensions for different indentation depths of 50 μm indenter

Indentation depth (μm)	W(μm)	D(μm)	D_p(μm)	S_h (D/W)	P_r (D_p/W)
5	31	2.5	0.26	0.081	0.008
10	31	5	0.51	0.161	0.016
20	52	11	1.01	0.211	0.019
40	70	20	1.96	0.286	0.028
60	72	35	3.47	0.486	0.048

In this investigation, the dent sharpness (S_h) and pile up ratio (P_r) are defined as

$$S_h = \frac{D}{W} \quad , \qquad P_r = \frac{D_P}{W} \tag{2.15}$$

where D is the dent depth, W is the dent width and D_p is the dent pile up. The various dent profiles are shown in Figure 2.11.

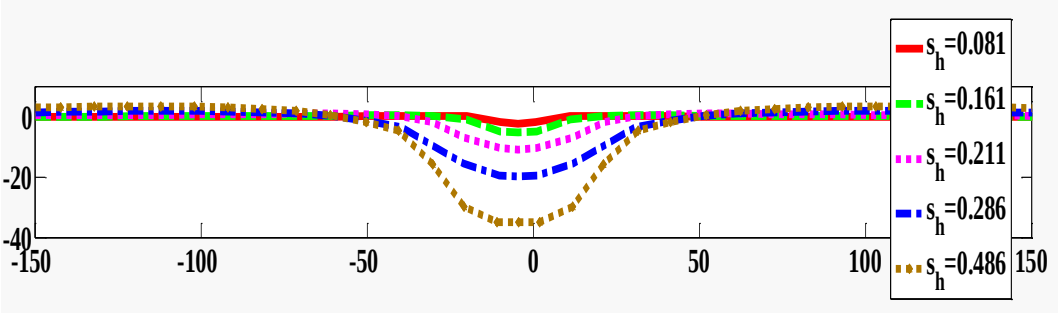

Figure 2.11: Dent profiles with different sharpness

Higher sharpness indicates steeper slope of a dent shape. Furthermore, five different loads were applied to the roller to generate different contact pressures. The contact geometry for these loading conditions are listed in Table 2.4.

Table 2.4: Different applied loads cause different contact configurations

Applied load on roller (mN)	497.87	380.13	314.16	254.47	176.71
P_{max} (GPa)	2.5	2.2	2	1.8	1.5
Half contact width ,b(μm)	125	110	100	90	75

The Weibull probability of failure for P_{max} = *2.5 GPa, 2 GPa* and *1.5 GPa* for the various sharpness and the pristine domains are depicted in Figure 2.12.

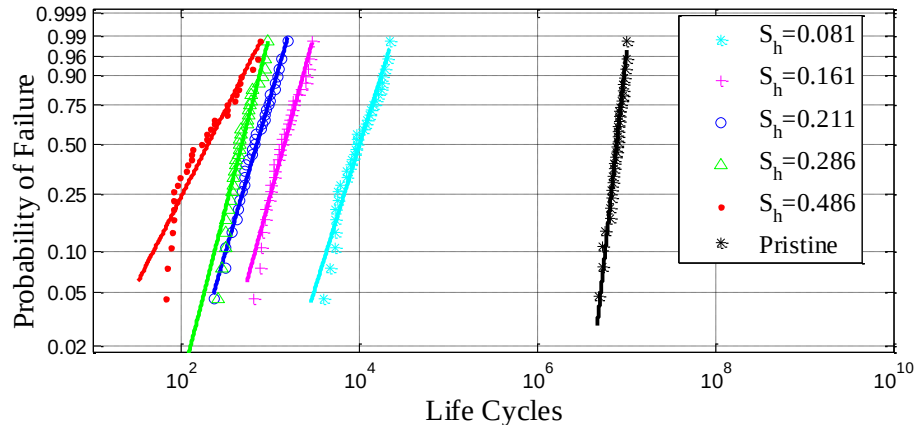

(a)

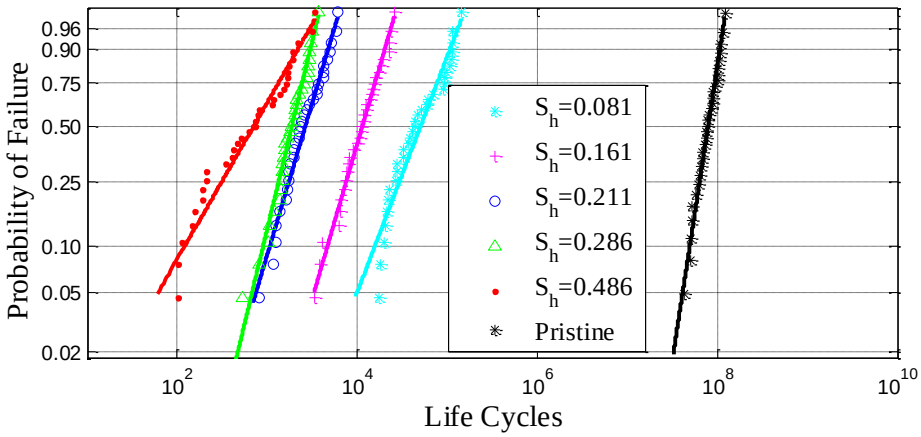

(b)

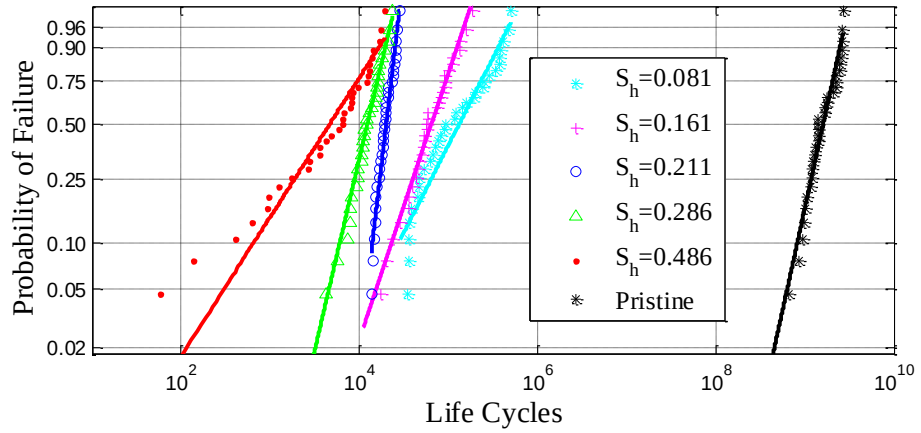

(c)

Figure 2.12: Weibull probability of RCF lives of Voronoi domains with different sharpness at a maximum contact pressure of (a) 2.5 GPa, (b) 2 GPa, (c) 1.5 GPa

The results demonstrate that the RCF life is reduced by increasing the dent sharpness for a constant load. The pressure spikes due to a dent are very sensitive to the geometry of the dent. The dent with sharper edges generate higher pressure spikes thus reduced estimated fatigue life. Furthermore, increasing the applied load causes higher contact pressures, hence higher pressure spikes at the dent edges. Larger pressure spikes accumulate more plastic strains which speed up the crack initiation process. The larger the load, the shorter the spall initiation life. The predicted L_{10} life and the Weibull slope of the initial lives for a different sharpness and loads are listed in Table 2.5. The results indicate that the average Weibull slopes for the dented domains are 2.2. Dommarco et al. [28] conducted RCF experiments on specimens with the artificial dents and found the average Weibull slope for different tests to be around 2.8.

Table 2.5: Statistical comparison of initiation life prediction between different applied loads with various sharpness

	P_{max}= 2.5GPa		P_{max}= 2GPa		P_{max}= 1.5GPa	
Sharpness	Weibull slope	Initial Life (cycles)	Weibull slope	Initial Life (cycles)	Weibull slope	Initial Life (cycles)
Pristine	6.29	5.76E+06	4.01	4.94E+07	2.81	8.24E+08
S_h=0.081	2.17	4.25E+03	1.61	1.57E+04	1.20	2.75E+04
S_h=0.161	2.47	6.69E+02	2.11	4.67E+03	1.83	2.30E+04
S_h=0.211	2.33	3.13E+02	2.07	1.07E+03	5.28	1.40E+04
S_h=0.286	2.65	2.35E+02	2.56	9.00E+02	2.63	6.02E+03
S_h=0.486	1.33	4.80E+01	1.07	1.21E+02	0.96	6.48E+02

Figure 2.13 depicts the effects of sharpness and pile up ratios on fatigue lives at various loads. By increasing the sharpness and pile up ratio, the estimated lives are decreased. The surface defects have a stronger influence on life reduction at lower applied loads due to more variations in contact pressure distribution.

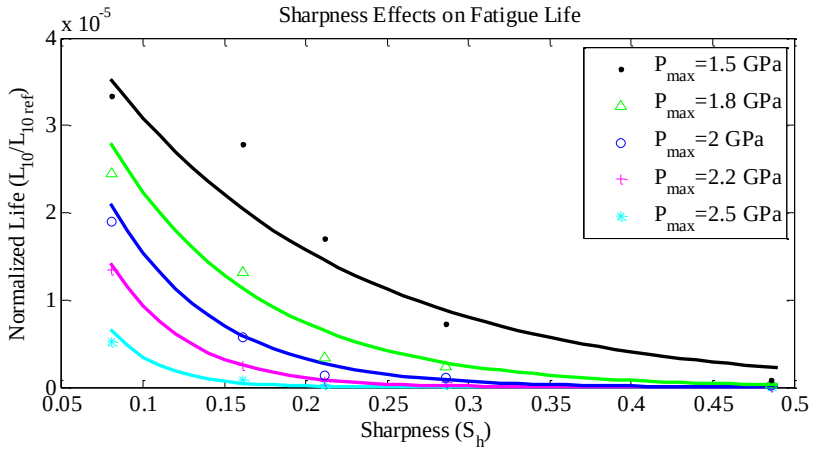

(a)

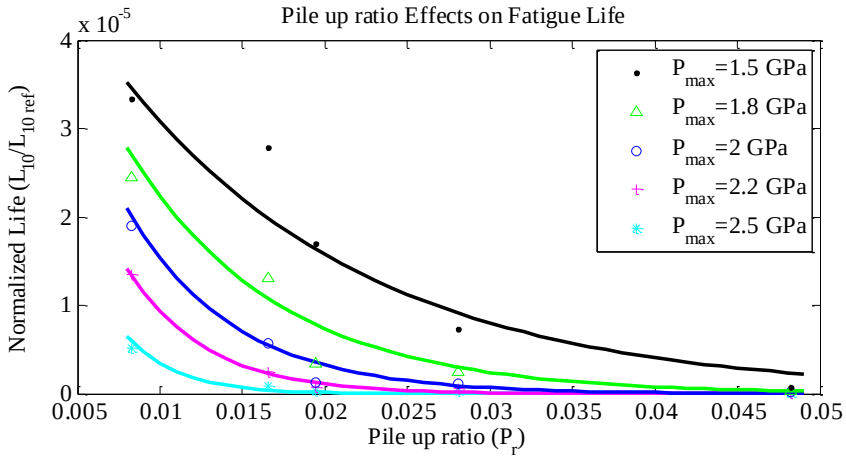

(b)

Figure 2.13: (a) Sharpness and (b) Pile up ratio effects on RCF lives at various applied loads

A relationship between L_{10} life, sharpness (S_h) and pile up ratio (P_r) for different maximum contact pressures was derived using regression analysis. The normalized L_{10} life for different sharpness is given as;

$$\frac{L_{10}}{L_{10\,Pristine_{(1.5\ GPa)}}} = a_s \mathrm{e}^{b_s S_h} \tag{2.16}$$

$$a_s = (2.5\mathrm{P}_{max} + 2.3\,) * 10^{-5}\ , b_s = -15.29{\mathrm{P}_{max}}^2 + 35.8\mathrm{P}_{max} - 26.1$$

The relationship between estimated L_{10} life and pile up ratio is given as;

$$\frac{L_{10}}{L_{10_{Pristine_{(1.5\ GPa)}}}} = a_p \mathrm{e}^{b_p P_r} \tag{2.17}$$

$$a_p = (2.5\mathrm{P}_{max} + 2.3\ ) * 10^{-5}\ , b_p = -152.86{\mathrm{P}_{max}}^2 + 357.98\mathrm{P}_{max} - 260.4$$

The estimated life using Equations (2.16) and (2.17) for different maximum contact pressure is shown in Figure 2.13. It can be seen that there is a good correlation between the numerical results and the derived equations.

2.4 Summary and Conclusions

In this investigation, a coupled finite element multibody model was developed to investigate the effects of surface defects on RCF life and spall formation based on accumulated plastic strains. In the current study, the contact pressure was obtained as a function of dent size and subsurface damage using the coupled FE multibody system. Furthermore, plasticity and microstructural effect were taken into account by developing an elastic plastic Voronoi FE model based on damage mechanics approach to predict RCF life of REBs. In order to consider the residual stresses and plastic strains due to indentation, the micro-indentation process was simulated by pressing a rigid indenter on an elastic plastic semi-infinite domain. Then a roller was rolled over the dented surface to determine the contact pressure and simulate the RCF. Numerical results demonstrated that the contact pressure distribution in the dented domain had two spikes at the dent shoulder which caused plastic strains and initiate a crack close to the dent. The mechanism of spall formation and Weibull slopes obtained from the current multibody model for dented surfaces is in good agreement with the experimental results available in the open literature [28,50,51]. The results indicate that the sharper the edges of the dent and higher the pile up cause larger pressure spikes and consequently reduced the fatigue life. Furthermore, increasing the applied load generated higher contact pressure and expedited the spall initiation process. The parametric study indicates that the sharpness and pile up ratio have an exponential RCF life reduction as a function of maximum contact pressures.

3. EXPERIMENTAL AND ANALYTICAL INVESTIGATION OF EFFECTS OF REFURBISHING ON ROLLING CONTACT FATIGUE

3.1 Introduction

Surface-originated damage in components of REBs can be repaired. In the mid-1970s, the aerospace industry began restoring bearings by grinding the surfaces of used bearings [98–100]. Since that time, bearing repair and refurbishment has become prevalent and is the standard practice in commercial aircraft applications. The popularity of this method has grown not only in the aerospace industry, but also in heavy industries [101]. Bearing repair and refurbishment can be an effective way to extend bearing life. Moreover, there are significant cost savings, since bearing refurbishing costs approximately 60% of new bearing replacement costs. Another advantage of refurbishment is the reduction in downtime, especially for custom-made bearings [101].

There are four reconditioning levels for bearing refurbishing, based on the amount of damage in the bearing components. The most basic case is category level I [102], where the corrosion is removed and the bearings are cleaned, reassembled and packaged to return for installation and service. At this level, no machining is required. At level II, the inner and outer rings are polished to remove the minimal damage on the raceways. In many cases, the raceways are heavily damaged and require level III repair, where the surfaces are ground to remove surface damage up to a depth of 0.015 inches (0.381 mm) [103]. In level III repair, the rolling elements are replaced in the bearing. When extreme material damage deeper than 0.015 inches is present, the rolling elements, cage or rolling bearing rings must be replaced with new parts. This is level IV repair. Among these four different levels of repair, level III repair is the most favorable, as it significantly enhances the fatigue lives of REBs with minimal cost. Another benefit of level III repair is to restore damaged surfaces that have defects caused by operating condition, which is a common industrial bearing damage mode [104]. This allows bearings to reach their critical damage mode and useful estimated life [105].

Few experimental and analytical investigations have been conducted on the effects of restoration on bearing life. In the past few decades, most of the experimental investigations have focused on determining the fatigue lives of pristine bearings rather than refurbished bearings. The

majority of the experimental studies for repaired bearings have been done by specific industries for particular applications [106].

Analytical investigations of refurbished bearings have been quite limited. Coy et al. [107] modified the Lundberg-Palmgren equation to estimate the fatigue life of refurbished bearings as dependent on the previous service time and grinding depth of refurbishing [108]. Based on their model, the refurbished L_{10} life prediction could be between 74% and 100% of pristine L_{10} life. This model was then extended by Zaretsky [109] to include maximum shear stress criteria. In the new model, the fatigue damage of the outer race and the damage of the inner race and rolling elements were additionally considered. Kotzalas and Eckels [106] developed an analytical model using the ISO 281:2007 standard. This model includes the entire stress field instead of the simplified stress field employed by Lundberg-Palmgren [108] and Zaretsky [109].

One restriction associated with all the previous models is assuming a prescribed constant Weibull distribution of bearing failure. Paulson et al. [105] proposed a new modeling approach, which could calculate the Weibull parameter for a group of bearings. This model used microstructure topology coupled with damage mechanics to predict the fatigue lives of refurbished bearings [105].

In this chapter, a thrust bearing test apparatus (TBTA) was designed and developed to experimentally investigate the rolling contact fatigue behavior of pristine and refurbished specimens. Case carburized AISI 8620 steel specimens were used in the experiments. First, RCF tests were conducted on the specimens to obtain the fatigue lives of pristine specimens. When the baseline L_{10} life (cycle) was determined, a second series of pristine specimens were tested in the TBTA up to 90% of the L_{10} life (cycle) of the pristine material. Some of the specimens were refurbished to a depth of 0.13b (b is the half contact width), and the rest were reground to the depth of 1.27b. The refurbished specimens were subjected to RCF until a spall was formed on the surface.

In the analytical part of this investigation, a model for predicting the fatigue life of refurbished RCF specimens was developed to incorporate the elastic-plastic material behavior of case carburized steel. A continuum damage mechanics approach was used to simulate material degradation due to fatigue. The effect of the carburizing process was included by varying the yield strength of the material linearly with the hardness and considering the residual stress distribution. In order to simulate the refurbishing process, continuum damage mechanics approach was

employed to determine fatigue damage accumulation up to a specific number of contact cycles. Then a layer of the original surface up to the grinding depth was removed from the numerical domain, while retaining the initial accumulated damage prior to refurbishing. In order to validate the model, the analytical model was used to simulate the experimental conditions. However, the contact geometry between the balls and flat AISI 8620 steel is circular. Therefore, a sectioning approach was used to simulate the circular contact using the 2D RCF model. The results of the analytical model were corroborated with the refurbishing experiments.

3.2 Experimental Investigation

In this section, the test apparatus and the specimens used in the experimental investigation are described. Furthermore, the testing procedure that replicates the bearing refurbishment process is explained.

3.2.1 Rolling Contact Fatigue Test Apparatus

In order to study the effect of refurbishing on rolling contact fatigue and analyze the materials' fatigue behavior, a thrust bearing test apparatus (TBTA) was designed and developed. The design of this test rig is influenced by the five-ball fatigue tester developed by Zaretsky et al. [110]. The TBTA depicted in Figure 3.1 consists of a five horsepower AC motor used to rotate a shaft that retains an upper race of a thrust ball bearing. The load was applied on the flat stationary specimen through a bearing housing (specimen holder) using a dead weight system attached to a lever arm. In this mechanism, the load is transferred to the specimen holder by a turnbuckle which distributes the load uniformly to all of the balls. The lower race of a thrust ball bearing was replaced with a flat specimen which was then subjected to fatigue and was used for evaluation post-grinding. An accelerometer attached to the specimen holder was used to detect the onset of a spall and suspension of the test. An average vibration level equal to 1.4 times the initial RMS vibration was defined as a threshold to stop the test. The threshold was defined based on the vibration analysis of a few specimens to find the first jump in vibration signal due to the first spall formation.

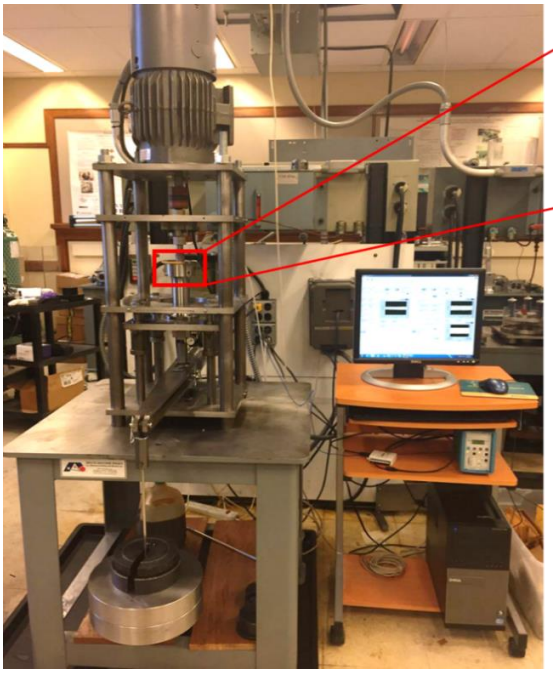

(a)

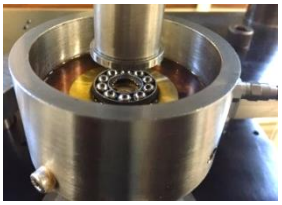

(b)

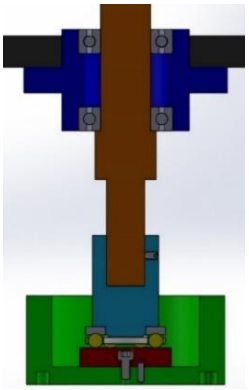

(c)

Figure 3.1: Thrust bearing test apparatus for conducting the RCF test: (a) TBTA setup, (b) specimen holder, (c) CAD model

3.2.2 Specimen Description

Flat specimens were used in order to provide an easy way to subject them to different levels of grinding. The flat specimens used in this investigation were made of case carburized AISI 8620 steel. The specimens were heat-treated and spheroidize-annealed. Figure 3.2 illustrates a schematic of the specimen. The two holes at the bottom of the specimen were included for accurate placement and alignment. The specimen's surface was carefully polished prior to testing.

Table 3.1 contains the specimen geometry, mechanical properties, surface roughness and the case depth based on Vickers hardness measurements. Figure 3.2 (c) and (d) depict the thrust ball bearing and the specimen (the lower race of the bearing) used in this study.

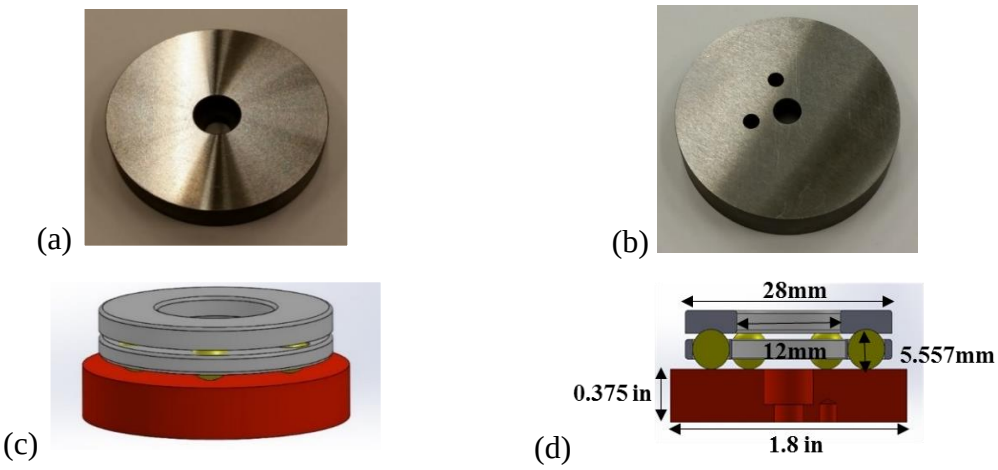

Figure 3.2: Flat specimen geometry: (a) testing surface, (b) bottom surface, (c) CAD model of thrust ball bearing, (d) section view of CAD model

Table 3.1: Specimen properties and geometry

Specimen Parameters	Value
Elastic Modulus (GPa)	210
Yield Strength at Top Surface (GPa)	2
Yield Strength at Core Region (GPa)	1.1
Specimen Diameter	1.8 in
Specimen Thickness	0.375 in
Roughness ($R_a\ \mu m$)	0.25 - 0.28
Case depth	2.5 mm

3.2.3 Fatigue Testing

The TBTA can operate at various loads and speeds with different lubricants. In order to accelerate fatigue damage for each specimen, all of the experiments were conducted at 5 GPa Hertzian contact pressure (half contact width of 190 μm). The rotational speed was set at 3450 rpm and Mobil Jet Oil II (synthetic) was used at room temperature (25°C) to lubricate the contact. The balls are made of 52100 through-hardened bearing steel. The upper race, balls and lubricant were replaced after each test. The contact specifications and experimental conditions are listed in Table 3.2.

Table 3.2: Experimental parameters and properties and geometry of thrust ball bearing

Experimental Parameters	Value
Elastic Modulus	210 GPa
Poisson's Ratio	0.3
Bearing OD	28 mm
Bearing ID	12 mm
Ball Radius	5.556 mm
Number of Balls	10
Applied Load (per ball)	374.43 N
Spindle Speed	3450 rpm
Radius of Contact, b	190 µm
Maximum Contact Pressure	5GPa

Fifteen RCF tests were conducted on AISI 8620 case carburized specimens to determine the baseline fatigue lives for pristine materials. Once the baseline L_{10} life (cycle) for the specimens was obtained, a new set of pristine specimens were subjected to RCF cycles equal to 90% of the L_{10} life of the pristine specimens. The specimens' surfaces were then ground to a certain depth. Two different depths were chosen to study the effect of grinding depth on refurbished specimens. Half of the specimens were ground to 0.13b (b is the half contact width) and the others were refurbished to 1.27b. The refurbished specimens were then tested in the TBTA until spalls were formed in the specimen.

3.3 Modeling Approach

In this investigation, a 2D elastic-plastic finite element model based on continuum damage mechanics was developed to investigate the effects of refurbishing. A sectioning approach [111] was developed to simulate circular contact using a 2D RCF model. In the following sections, the FEM model used to simulate a rolling pass, the RCF model for case carburized material, and the numerical simulation for the refurbishing process are described. For a detailed description, please

refer to Slack et al. [112], Paulson et al. [105], Walvekar and Sadeghi [93], Paulson et al. [113] and Walvekar et al. [111].

3.3.1 Simulation of a Rolling Pass

In this study, the commercially available FE solver ABAQUS was used to obtain the subsurface stress solution under the contact pressure. Due to the high loads, the contact pressure between the flat specimen and balls was considered to be Hertzian. The user subroutine UTRACLOAD was used to apply the Hertzian pressure as a non-uniform surface traction vector. Equation (3.1) defines the Hertzian pressure profile as a normal component of the surface traction.

$$p_y(x) = P_{max}\sqrt{1-\left(\frac{x-x_c}{b}\right)^2} \tag{3.1}$$

where (x_c, *0*) is the coordinate of the center of the Hertzian pressure distribution, P_{max} is the maximum Hertzian pressure, and *b* is the half-contact width.

The shear surface traction in the rolling direction is defined by a constant ratio of the normal traction.

$$t_x(x) = \mu_s|p_y(x)| \tag{3.2}$$

where μ_s is the coefficient of friction. The well lubricated nature of contact is taken into account by setting the coefficient of friction to 0.05 [82,83]. To simulate a rolling pass, the Hertzian pressure profile was translated over the surface by sequentially applying the traction in 21 steps from –2.5b to 2.5b in the rolling direction.

In this modeling approach, Voronoi tessellation [84] was used to represent geometric disorder and randomness of the material microstructure topology. In Voronoi tessellation, a space is divided into many regions around random seed points. In each region, all points are closer to the seed point of that region than the other generating points. These regions are called Voronoi cells. Voronoi cells and their boundaries represent the grain and grain boundaries, respectively, in the real microstructure [47,54,87,105] (Figure 3.3). The average diameter of the Voronoi cells was set to 10 microns, which is typical for bearing steel [114]. After the domains are generated, the Voronoi cells are meshed with constant strain triangular (CST) elements by connecting the centroid of each cell to its edges. Figure 3.4 illustrates the model geometry, and the corresponding

dimensions are listed in Table 3.3. To save computational time, the Voronoi elements were used only in the representative volume element (RVE) region, while the rest of the domain was meshed with coarse CST elements. Previous investigations [47,54,87] have used an RVE region depth of 1b. However, for this study, the RVE depth was extended to 2.4b in order to provide sufficient microstructural depth after refurbishing the domains [105].

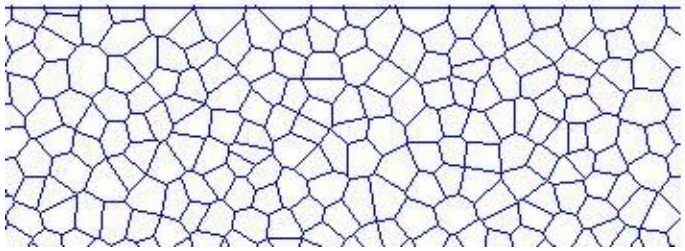

Figure 3.3: Random material microstructure generated using a Voronoi tessellation

Table 3.3: 2D model dimensions for refurbishing simulation

Dimension	Microstructure Topology Region	Simulation Domain
X (half contact width)	(-2.2b, 2.2b)	(-5b, 5b)
Y (half contact width)	(0, -2.4b)	(0, -7b)

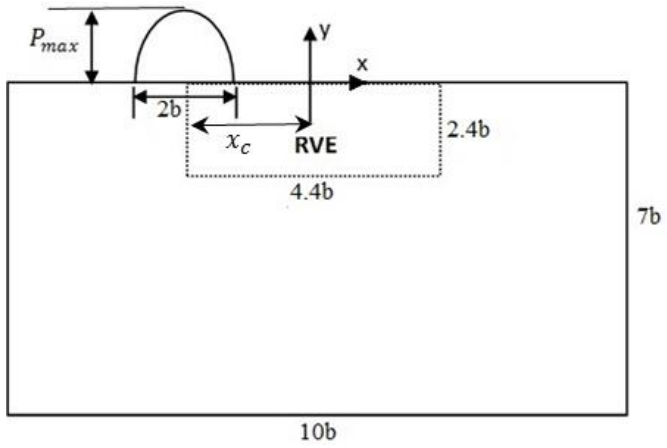

Figure 3.4: Computational domain used in FE simulation of refurbishing

The FE model simulates the operating conditions of the experimental investigation, including Hertzian pressure. The maximum Hertzian pressure during the experiments was 5 GPa, which leads to considerable plastic deformation in the subsurface region of the specimens. Therefore, an elastic-plastic material model was employed in the FE model to capture the stress-strain response accurately and simulate the effects of plasticity-induced fatigue damage. The stress-strain response of AISI 8620 can be modeled as a linear elastic and linear kinematic hardening plastic (ELKP) material [93]. The details of the von Mises plasticity model with linear kinematic hardening are presented in [79].

3.3.2 Case Carburized Steel Modeling

The specimens tested in the experimental investigation were made from case carburized steels. The carburization of steel results in a gradient in the microstructure as a function of depth that influences the mechanical properties of the material [115–119], Cahoon [120] studied the relationship between hardness and yield strength. Pavlina and Van Tyne [121] showed that there is a linear correlation between the yield strength and Vickers hardness of the steel.

$$S_y = -90.7 + 2.876H_v \tag{3.3}$$

where S_y is yield strength in MPa and H_v is Vickers hardness in units of Kg_f/mm^2.

To investigate the variations in hardness among the AISI 8620 specimens used in the experimental investigation, micro-indention tests were performed at different depths along the cross section. The results demonstrated that the hardness reached its maximum at the surface and decreased linearly to the core region, as illustrated in Figure 3.5. The case depth was found to be 2.5 mm. Based on the hardness measurements and Equation (3.3), the yield strength of the case carburized specimen was determined to be 2.06 GPa and 1.15GPa, at the top surface and the core region, respectively (Figure 3.6). In the FEA model, the hardness variations in the case carburized material were accounted for by varying the yield strength in the simulation domain with depth, as shown in Figure 3.6.

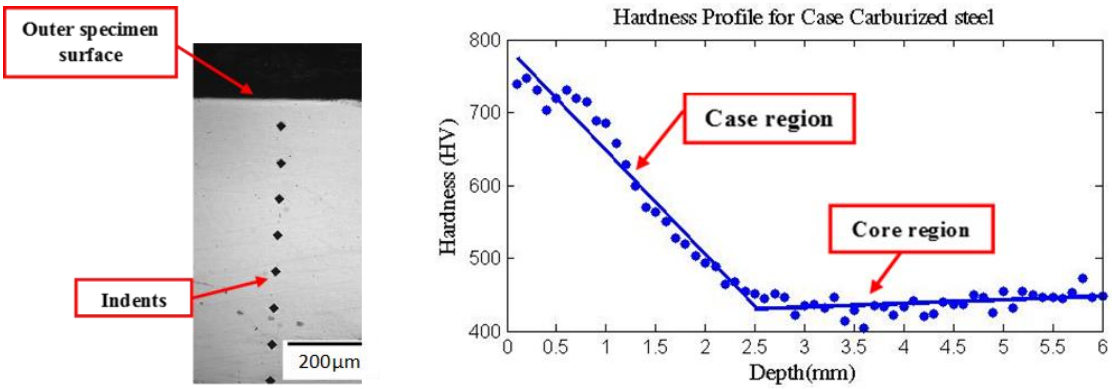

Figure 3.5: Vickers hardness measurements at different depths from the surface for a case carburized AISI 8620 steel

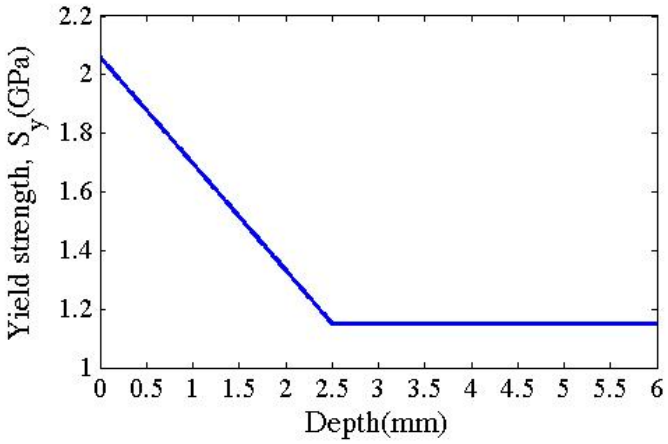

Figure 3.6: Variations of yield strength with respect to depth for pristine domain of case carburized steel in the current model

The carburization process also generates residual stresses that play an important role in the fatigue resistance of the case carburized material [122]. Parrish and Harper [123] analyzed about 70 residual stress distributions for carburized and hardened steels. Figure 3.7 depicts a typical residual stress profile for a case carburized steel. Based on their survey, the residual stress peak occurs at nearly 20% of the case depth and reduces to zero at a depth equal to the case depth of the material. Figure 3.8 depicts the residual stress distribution used in this study.

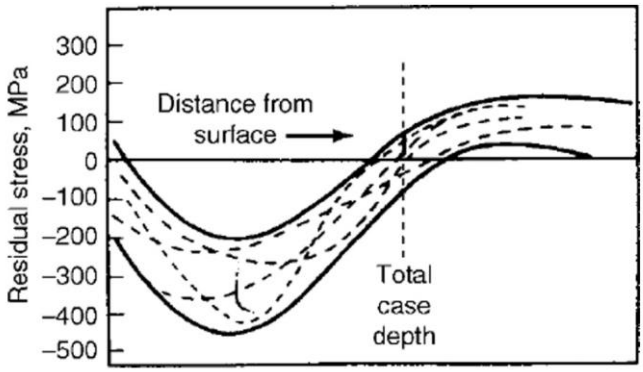

Figure 3.7: Residual stress distributions for case carburized steel [101]

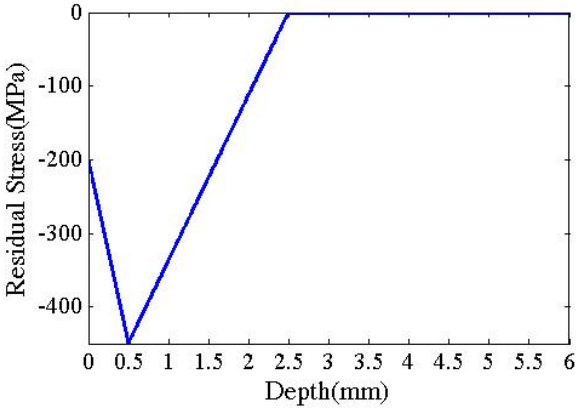

Figure 3.8: Residual stress distributions as a function of depth for pristine domain of case carburized steel

3.3.3 Fatigue Damage Model

In this investigation, modeling of material degradation due to fatigue is based on the continuum damage mechanics approach for rolling contact fatigue [45,124]. The theory of damage mechanics attempts to model the microscopic mechanisms of fatigue damage in an empirical fashion. In order to capture the effect of damage on the mechanical response of a material, a damage variable D is employed in the constitutive equations.

In high cycle fatigue, the evolution of damage for the elastic material is dependent only on the state of stress. However, if the material undergoes yielding, the damage is dependent on the accumulated plastic strain along with the state of stress. Hence, two different damage evaluation laws are simultaneously used in this model.

For high cycle fatigue, a commonly used form of the damage evaluation for purely elastic is [48],

$$\frac{dD}{dN} = \left[\frac{\Delta\sigma}{\sigma_r(\sigma_m) \times (1 - D)}\right]^m \tag{3.4}$$

where N is the cycle number, $\Delta\sigma$ is the critical alternating stress causing fatigue damage, σ_m is a mean stress, and σ_r and m are material parameters that must be experimentally determined. σ_r is the resistance stress [48] that represents the ability of a material to resist damage accumulation. Based on previous research [47,75,79,80], the stress range causing damage during rolling contact fatigue is the shear stress reversal, which acts along the grain boundaries. Shen et al. [125] developed a damage rate law incorporating the effect of mean stress resulting from the presence of residual stresses. Hence, the damage accumulation rate under rolling contact loading is

$$\frac{dD}{dN} = \left[\frac{\Delta\tau}{\tau_{r0}(1 - \frac{\sigma_m}{S_{us}})(1 - D)}\right]^m \tag{3.5}$$

where $\Delta\tau$ is the shear stress range along the Voronoi grain boundary, τ_{r0} is resistance stress, σ_m is a mean stress due to the presence of residual stresses, and S_{us} is the ultimate strength in shear.

The damage law for material undergoing yielding [45,93] is given by

$$\frac{dD}{dN} = \left[\frac{\sigma_{\max}^2}{2ES_0\left(1 - \frac{\sigma_m}{S_{us}}\right)^2 (1 - D)^2}\right]^q \dot{p} \tag{3.6}$$

where σ_{max} is the maximum von Mises stress over a fatigue cycle, $\dot{p}$ is the accumulated plastic strain over a fatigue cycle resolved along the grain boundary, E is the undamaged modulus of elasticity, and S_0 and q are material dependent parameters.

The material parameters (τ_{r0}, m and S_0, q) employed in the elastic and plastic damage rate laws (Equations (3.5) and (3.6)) must be determined experimentally. In this study, it is assumed that the damage mechanisms for RCF and torsion fatigue are equivalent, since the fatigue damage

under rolling contact conditions and torsional fatigue are both caused by the action of shear stresses. Therefore, the fatigue damage parameters are evaluated from the stress-life (SN) data for a material in torsional fatigue. The procedure to calculate damage parameters from the torsion SN curve is provided in [47,79,80,93].

Figure 3.9 demonstrates the torsion SN curve for AISI 8620 steel [114]. Using the same approach as [93], the damage parameters for case carburized steel are extracted. Note that crack initiation in torsion fatigue experiments occurs at the surface, and the majority of the total fatigue life is the initiation life [114]. Hence, the values of σ_m (the residual stress) and S_{us} at the surface of case carburized material are used to calculate the material damage parameters. The values of these parameters at the surface of the case carburized specimens are listed in Table 3.4.

Table 3.4: Material damage parameters at the surface of case carburized specimens evaluated using torsion SN data (Figure 3.9)

Material Property (at the surface)	AISI 8620 Specimen
Vickers Hardness	750
Yield Strength (GPa)	2.06
τ_{r0} (GPa)	5.286
m	13.16
S_0 (GPa)	0.0587
q	4.67

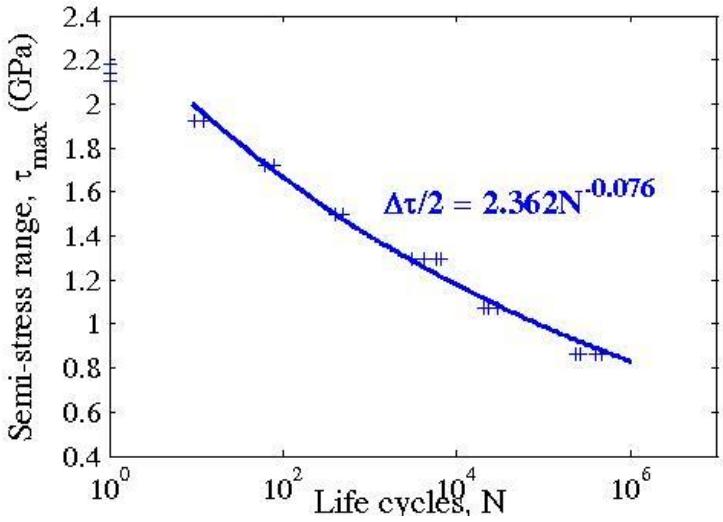

Figure 3.9: Experimental torsion SN data and power law fit to the data for case carburized AISI 8620 steel from [92]

As described earlier, the yield strength of the case carburized steel varies with depth (Figure 3.6). Since variation in yield strength has an influence on the torsion SN curve of the material, the damage parameters also vary with depth. It was assumed that the fatigue strength coefficient varies linearly with yield strength, while the slope of the SN curve (i.e., the fatigue strength exponent) remains the same for the same material [93]. Consequently, τ_{r0} and S_0 — which are dependent on fatigue strength coefficient — vary with respect to the yield strength [93]. Figure 3.10 depicts the variations with yield strength in these damage parameters for AISI 8620. However, the damage parameters *m* and *q* depend only on the slope of the SN curve. Therefore, they do not vary with yield strength [93].

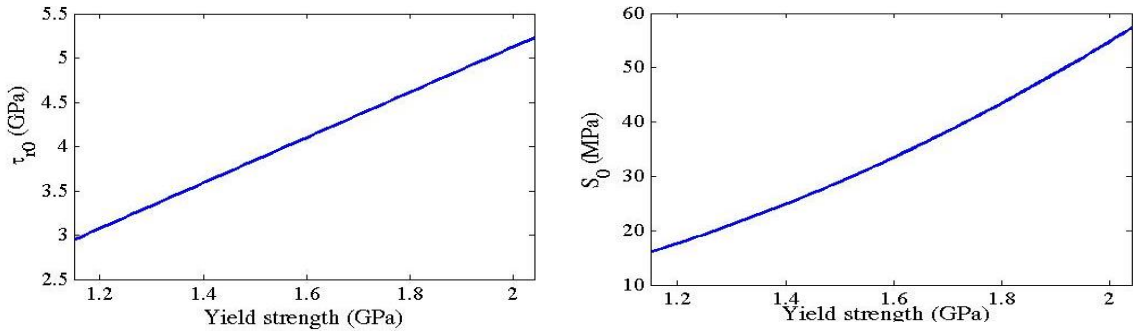

Figure 3.10: Variation of damage parameters τ_{r0} and S_0 with respect to yield strength for case carburized AISI 8620 steel

The rolling contact fatigue analysis requires the simultaneous solution of the damage evolution equation (Equations (3.5) and (3.6)) and constitutive relationships for each element. In the current investigation, a standard "jump-in-cycles" algorithm developed by Lemaitre [45] was employed, wherein the stress-strain response of the model and the damage value are assumed to be constant over a block of cycles. The specific details of this algorithm can be found in [47,79,105]. At the beginning of the simulation, undamaged conditions are considered for all the elements. Once the damage value reaches 1, the element is fully damaged. The final failure occurs when the damage reaches the surface of the domain.

3.3.4 Simulation of Refurbishing Process

The bearing refurbishment is simulated in two steps. The first step is to determine the specific number of cycles at which the domain should be refurbished (refurbishing cycles) and the damage associated with each element in the domain before refurbishing. In order to determine the refurbishing cycles, 33 microstructural domains were generated and subjected to rolling contact fatigue cycles until complete failure (crack reached the surface). The L_{10} life was determined and the refurbishing cycles were set to 90% of the L_{10} life. Then, the accumulated damage for each element of the domain at refurbishing cycles was calculated. Further details can be found in [105].

Bearing refurbishment was simulated by removing a layer of material from the top of the microstructural domain following the process described in [105]. The accumulated damage in the remaining domain (calculated in the first step) was retained to account for the initial loading passes on the domain. The refurbished domains were then subjected to repeated RCF load passes until final failure. In order to preserve the original size of the simulation domain, constant strain elements were added to the bottom of the domain. Details of this approach can be found in [105].

As described earlier, the yield strength and residual stresses in case carburized steel vary with depth from the surface. Yield strength and residual stress distribution in the refurbished case carburized domains are different from those of the pristine domains because a portion of the material is removed from the top layer of the domain [113]. Figure 3.11 illustrates the variation with depth of yield strength and residual stresses for the refurbished domain of case carburized steel. Please note that, the depth from the surface was plotted on the x axis. Therefore, the depth for the refurbished domain was measured from the reground surface. Hence the yield strength and residual stresses distribution for the refurbished domains were shifted to the left compared to the

distributions for the pristine domains. These variations are included in the RCF simulation of refurbished domains used to obtain fatigue lives. Note that the variations in yield strength and residual stress distribution in the material due to the grinding process were neglected in the present model.

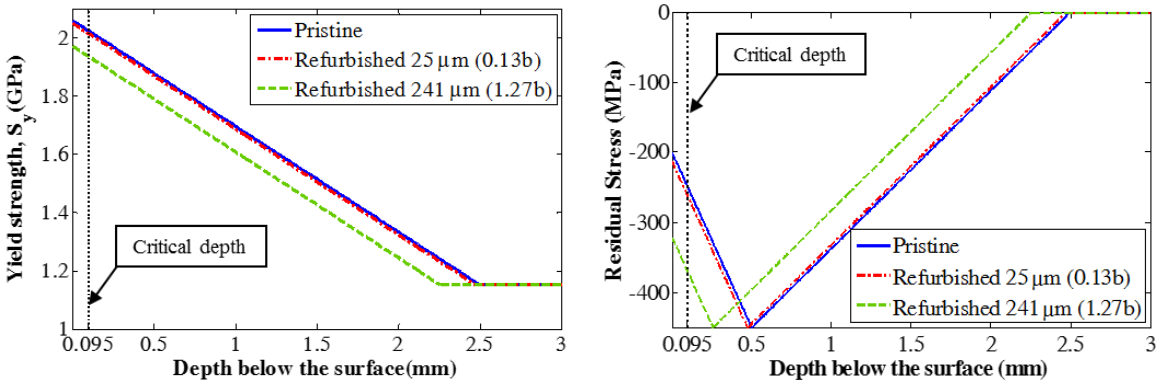

(a) (b)

Figure 3.11: Yield strength and residual stress distribution as a function of depth for refurbished domain of case carburized AISI 8620 steel for different grinding depths

3.3.5 Sectioning Approach

In the RCF experiments performed on the thrust bearing test apparatus, the test specimens experience spherical Hertzian pressure due to the circular contact geometry. However, the 2D RCF model assumes line contact and cylindrical pressure. Therefore, a novel sectioning approach is proposed to simulate circular contact using the 2D model.

In this approach, the spherical Hertzian pressure distribution is divided into different 2D pressure sections along the rolling direction. The distance between each section is chosen to be equal to the average grain size of bearing steel materials (10 µm). Figure 3.12 depicts the spherical Hertzian pressure profile and 2D sections for circular contact. Half of the pressure profile is considered because of symmetry. Each pressure section is implemented in the 2D RCF model described earlier to obtain the fatigue life of that section. The fatigue lives are averaged to obtain the RCF life for the 3D pressure profile [111].

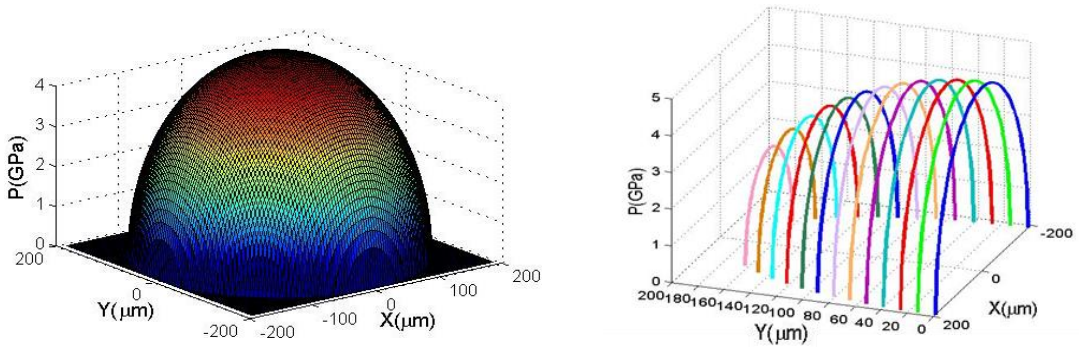

Figure 3.12: Hertzian pressure profile for point contact: (a) 3D distribution, (b) 2D pressure sections

The spall shapes observed in the experiments indicate that catastrophic damage occurs when the RCF damage spreads to a certain distance perpendicular to the rolling direction [111]. To explain this behavior, the subsurface stresses were investigated for spherical Hertzian pressure. Figure 3.13 depicts the distribution of different components of the shear stresses beneath the surface. It is noted that there is a region of high shear stresses near the end of the pressure contact that coincides with the region of catastrophic damage in the experiments. Thus, it is concluded that the distance between the centerline and the maximum shear stress perpendicular to the rolling direction is a critical distance. The critical distance determines how many pressure sections should be considered in the sectioning approach.

For this reason, the pressure sections beyond the critical distance are not considered in the sectioning procedure. Using the analytical equations for the subsurface stresses under contact conditions similar to those of the experiments, this distance was found to be equal to 0.86 times the half contact width (contact radius). This approach was implemented to calculate the RCF lives of both the pristine and refurbished domains of case carburized AISI 8620.

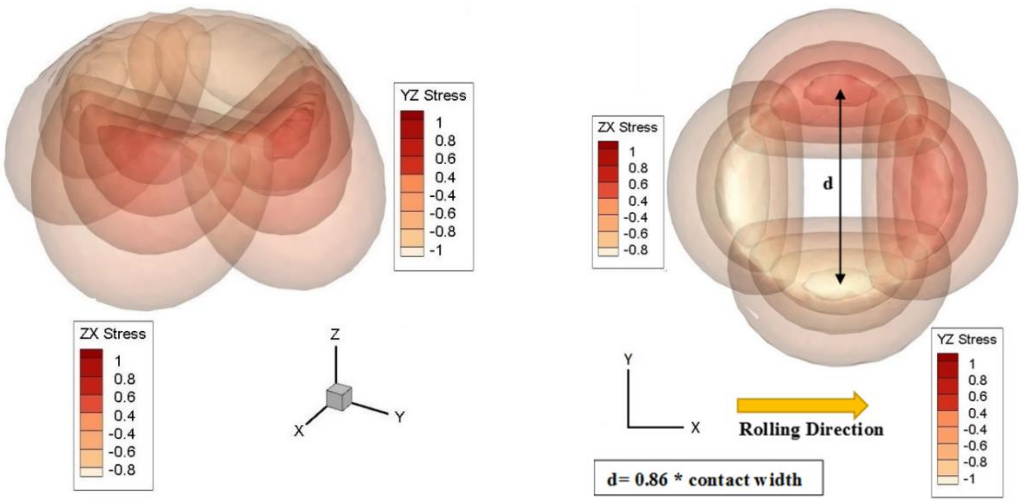

Figure 3.13: Top view and isometric view of subsurface shear stresses due to spherical Hertzian contact pressure profile

3.4 Results and Discussion

3.4.1 Experimental Results

Rolling contact fatigue experiments were conducted using the TBTA on pristine and refurbished specimens made of case carburized AISI 8620 steel to study the effect of bearing refurbishment on RCF lives. The maximum Hertzian pressure for all experiments was 5 GPa. The half contact width (b) was 190µm and the grinding depths for refurbishing were 25µm and 241µm. The specimen geometry and experimental conditions are listed in Table 3.2 and Table 3.3, respectively. A two-parameter Weibull distribution was used to determine the L_{10} life. The Weibull probabilities of the pristine and refurbished specimens with two different grinding depths are depicted in Figure 3.14. The L_{10} lives for the original and refurbished AISI 8620 specimens calculated from Weibull probability plots are listed in Table 3.5. The calculated L_{10} life of pristine specimens is 10.1 million cycles and the Weibull slope is 1.59. A low Weibull slope indicates more scatter in life; the observed Weibull slope is within the range typically observed in RCF experiments (0.7 to 3.5) [126].

Table 3.5: Experimental results for case carburized specimens (RCF life)

Test Type	Pristine	Refurbished at 25 µm	Refurbished at 241 µm
Number of Tests	15	11	15
Hertzian Pmax (GPa)	5	5	5
Half Contact Width (µm)	190	190	190
Weibull Slope	1.59	1.01	1.61
L_{10} Life (cycles)	1.01E + 07	2.44E + 06	1.37E + 07

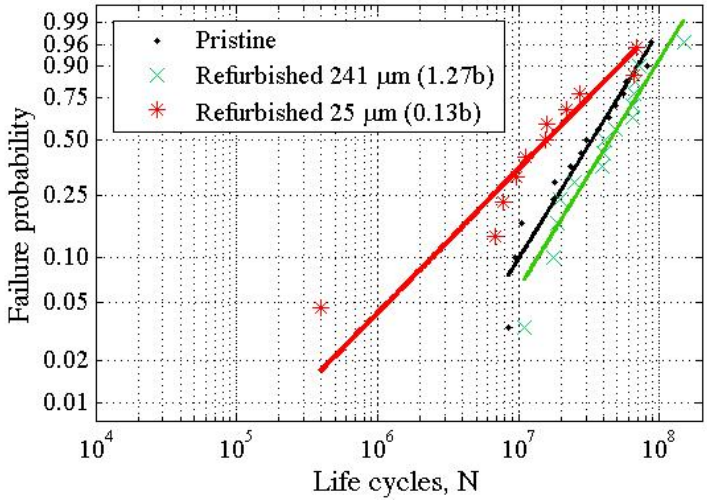

Figure 3.14: Weibull probability of failure for AISI 8620 specimens from experiments

Figure 3.14 demonstrates that the fatigue lives of the specimens refurbished to 241 µm were at least comparable to the fatigue lives of the pristine specimens, whereas in the case of refurbished depth of 25 µm, the fatigue lives decreased compared to the pristine specimens. This behavior can be explained as follows.

Two competing phenomena play a role in determining the influence of refurbishing depth on the fatigue life of the refurbished case carburized specimens. In the case carburized material, the yield strength — and, consequently, the fatigue resistance — reduce from the surface to the core. During refurbishing, the harder top layer of material is removed so the softer material with

less fatigue resistance bears the load, which reduces the RCF life. Therefore, according to this phenomenon, greater refurbishing depth has a negative impact on fatigue life.

On the other hand, the life of the refurbished specimens is also dependent on the amount of damaged material that remains in the specimens after refurbishing. Analysis of failed rolling components subjected to RCF reveal that the subsurface cracks often initiate in the region of the maximum orthogonal shear stress reversal, which is 0.5b [1,75,108,127]. By regrinding the surface of the specimens to a greater depth (e.g., > 0.5b), most of the damaged region in the specimens is removed. Thus, increasing refurbishing depth removes the damaged area and can increase the RCF life of the refurbished specimens.

From the experimental results, it can be concluded that the effect of the first phenomenon (variation of the yield strength with depth) on the RCF lives is negligible for the experimental conditions investigated in this study. This could be because the refurbishing depths (25 μm and 241 μm) used in this investigation are considerably smaller than the case depth of the specimen, which is 2500 μm (Figure 3.5). Therefore, the material properties of the refurbished specimens are similar to those of the original specimens. This was confirmed by performing micro-indentation tests on pristine as well as refurbished specimens. Figure 3.15 depicts the variations of hardness with respect to depth before and after refurbishing for both grinding depths.

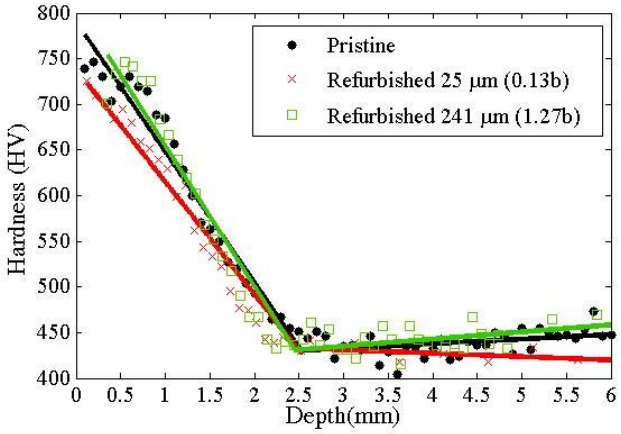

Figure 3.15: Vickers hardness measurements at different depths from the surface for the refurbished case carburized AISI 8620 steel at two different grinding depths

In addition to studying the effects of refurbishing on the fatigue lives of the test specimens, the spall shapes of the specimens at different grinding depths were evaluated under an optical profilometer. The typical spall shapes observed in the pristine and refurbished specimens are illustrated in Figure 3.16. Table 3.6 contains the spall dimensions for the AISI 8620 specimens. The location of maximum shear stress in circular contact is about 0.5b below the surface [127], and the averaged spall depth from experiments on pristine specimens is near 80μm (0.5b). This demonstrates that alternating shear stress causes subsurface-originated spalling in rolling contact fatigue. Moreover, the shapes and dimensions of the spalls observed in the pristine and refurbished specimens resemble each other. All the spalls on the refurbished AISI 8620 specimens for both grinding depths were evaluated and the dimensions were measured. The spall depth and length on both refurbished specimens are close to those of the pristine. Figure 3.16 and Table 3.6 demonstrate this similarity.

Table 3.6: Spall dimensions of AISI 8620 steel

Parameter	Pristine	Refurbished at 25 μm	Refurbished at 241 μm
Spall Size (length, height)	393.75*74.9 μm	411*90 μm	444.86*60 μm
Spindle Speed	3450 rpm	3450 rpm	3450 rpm
Ball Material	Chrome steel	Chrome steel	Chrome steel
Number of Balls	10	10	10
Oil Type	Mobil jet oil II	Mobil jet oil II	Mobil jet oil II
fatigue life	5.8E + 07	2.153E + 07	3.93E + 07

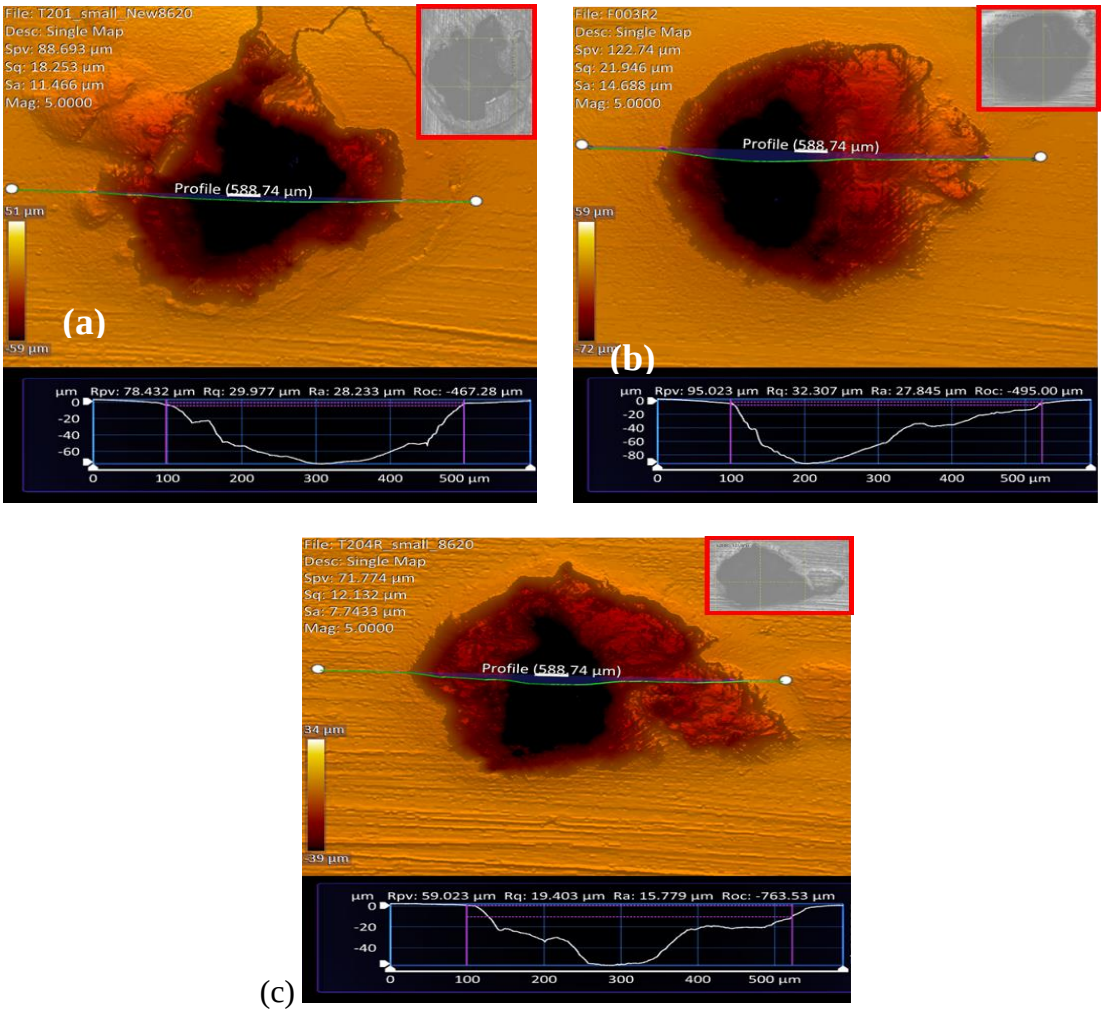

Figure 3.16: Spall shape of a specimen: (a) pristine case carburized steel, (b) refurbished case carburized steel with grinding depth of 25µm, (c) refurbished case carburized steel with grinding depth of 241µm

3.4.2 Analytical Results

A 2D elastic-plastic FE model and the sectioning approach were used to predict the fatigue life of case carburized AISI 8620 pristine and refurbished domains for circular contact. Table 3.7 contains the parameters and material properties used in this simulation. To compare the analytical results to experimental results, the maximum pressure and half contact width for the 3D Hertzian pressure profile, and also the grinding depth for refurbishing, were chosen to be the same as the experiments. In order to characterize the fatigue life scatter of the refurbished specimens, 33 microstructure domains were randomly generated using the Voronoi tessellation procedure. As

described earlier, for each domain 18 pressure profile sections were separately passed over the top surface of the microstructure and the fatigue lives of all pressure sections were averaged to determine the RCF life for that domain. The L_{10} life for pristine domains as per two-parameter Weibull distribution was 2.45E + 07. Therefore, the accumulated damage up to cycle number 2.20E + 07 (i.e., 90% of L_{10} life) was calculated for each domain. After that, the refurbishing procedure was applied as described in the previous section, and the fatigue lives of the refurbished domains were obtained.

The life distributions of the pristine and refurbished domains of case carburized AISI 8620 steel at two grinding depths are depicted in Figure 3.17. It can be observed that the estimated lives of pristine and refurbished domains are in good agreement with the experimental results.

Table 3.8 and Table 3.5 contain the Weibull slopes and L_{10} lives for the analytical and experimental results, respectively. The Weibull slopes for the analytical RCF lives of the pristine and refurbished domains at grinding depths of 25μm (0.13b) and 241μm (1.27b) are 3.82, 4.10, and 5.44, respectively. The larger Weibull slopes obtained from the analytical results compared to the experiments indicate less scatter in the fatigue lives. This difference could stem from the assumptions of the analytical model. To simplify the FE model, isotropic uniform material properties were assumed, and the effects of material defects, inclusions and micro voids were neglected while simulating the material microstructure.

Table 3.7: Material properties used in the simulation

Parameters	Value
Undamaged Elasticity Modulus, E	200 GPa
Hardening Modulus, M	10 GPa
Poisson's Ratio, ν	0.3
Material Grain Diameter, d_g	10 μm
Maximum Hertzian Pressure, P_{max}	5 GPa
Contact Half Width, b	190 μm
Surface Coefficient of Friction, μs	0.05
Yield Strength at the Surface	2.06 GPa
Yield Strength in the Core Region	1.15 GPa

Table 3.8: Analytical results for AISI 8620 steel at 5 GPa

Test Type	Analytical (Pristine)	Analytical (Refurbished) 25μm (0.13b)	Analytical (Refurbished) 241μm (1.27b)
Number of Specimens	33	33	33
Weibull Slope	3.82	4.1	5.44
L_{10} Life (cycles)	2.45E+07	2.10E+07	3.18E+07

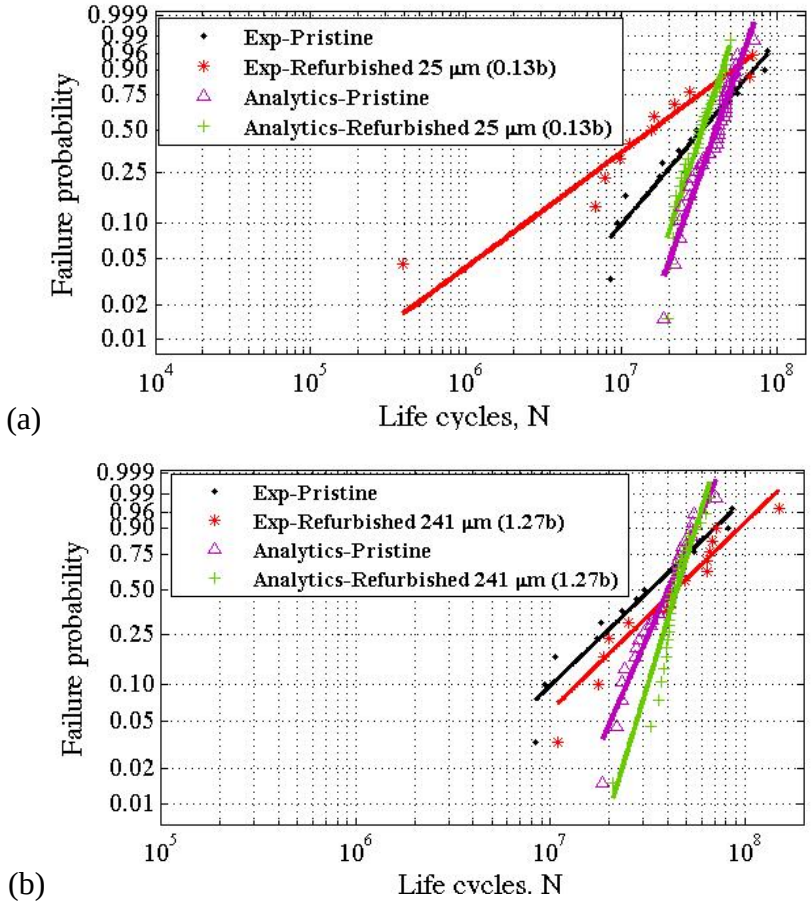

Figure 3.17: Life distribution of pristine and refurbished domains of AISI 8620 steel with grinding depth of (a) 25μm (0.13b) and (b) 241μm (1.27b)

It should be noted that the analytical results suggest that the RCF lives for the refurbished domain are enhanced by increasing the grinding depth. Factoring into this enhancement are the accumulated damage, yield strength and residual stress profile of the refurbished domain. As described earlier, yield strength and residual stress for carburized steel vary with depth, so these

parameters have different effects on the performance of pristine and refurbished materials at different grinding depths. Figure 3.11 depicts the variation of yield strength and residual stress with depth for the pristine and refurbished domains, as well as the depth of maximum shear stress reversal (0.5b). As the grinding depth increases, the yield strength at the critical depth decreases, which tends to reduce the RCF life of the refurbished domain. On the other hand, the increase in residual stress at the critically stressed regions enhances the fatigue resistance of the refurbished domain. Moreover, grinding depth also affects the range of the accumulated fatigue damage in the refurbished material. If the grinding depth is more than the critical depth (0.5b), most of the material damaged during the fatigue cycles prior to refurbishing is removed.

For refurbished domains with a 25 μm grinding depth, the distribution of the yield strength and residual stress in the refurbished domain does not vary significantly from that of the pristine domain (Figure 3.11), but most of the damaged material remains in the refurbished domain. Therefore, the fatigue lives of these refurbished domains are lower than those of the pristine domain. Conversely, for the refurbished domain with a 241 μm grinding depth, the yield strength and the compressive residual stress of the refurbished domain at the critical depth (0.5b = 0.095 *mm*) are 1.94 GPa and 368.3 MPa, respectively, compared to the pristine domain (2.03 GPa and 247 MPa). It is to be noted that the increase in the compressive residual stress at the critical depth in the refurbished domain is significantly higher than the reduction in the yield strength. Furthermore, most of the damaged parts are removed from the surface (the critical depth is 0.095 *mm*). Consequently, the refurbished domains with a grinding depth of 241 μm were predicted to have longer lives than the pristine domains. This behavior at different values of grinding depth is consistent with the experimental results.

Analytical spall shapes were generated using the following procedure: Each pressure profile section generates a 2D cross section of the spall similar to the one depicted in Figure 3.18. Thus, the sectioning approach produces different cross sections of the 3D spall shape. The 3D spall surface is created by interpolating these 2D cross sections.

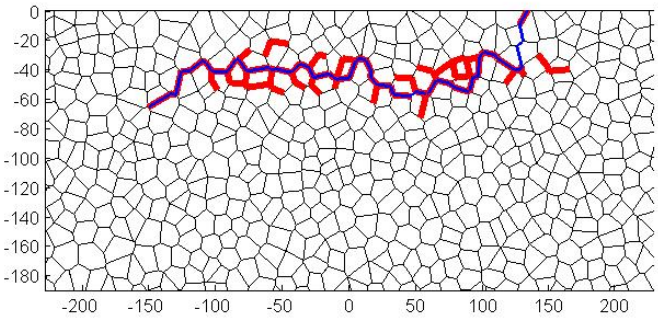

Figure 3.18: Spall shape for one section of pressure profile for AISI 8620

Figure 3.19 demonstrates an example result of this process for pristine AISI 8620 steel. It can be observed that the analytically generated spall resembles the experimental spall shape. Typically, the spalls observed in experiments with the smoother surface have greater length and depth than the analytically generated spalls. But the RCF tests cannot be stopped immediately after the spall is formed, and the continued loading expands the size of the spall in all directions. Additionally, the impact of the steel balls on the damaged region smoothens the spall surface. This may explain the differences between the experimental and analytical spall shapes in topology and size.

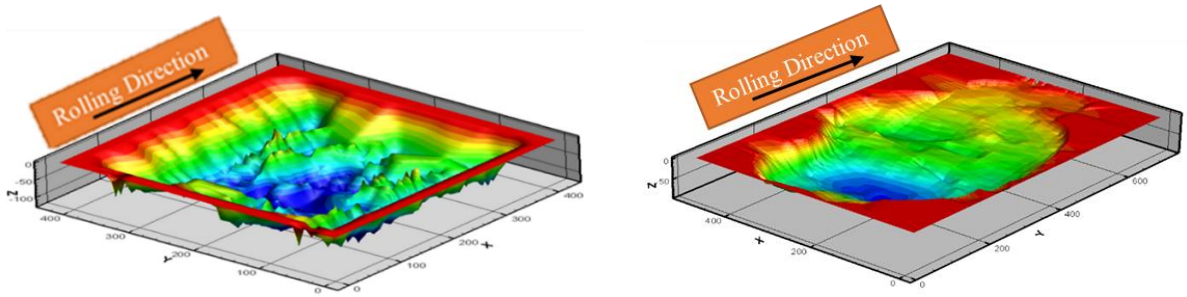

(a) (b)

Figure 3.19: 3D spall shape: (a) generated using sectioning approach in 2D FE model for AISI 8620 pristine, (b) experimental observed for AISI 8620 pristine

3.5 Summary and Conclusion

The objectives of this study were to experimentally and analytically investigate the effects of refurbishing on AISI 8620 case carburized steel. A thrust bearing test apparatus (TBTA) was designed and developed to determine the RCF lives of pristine and refurbished flat specimens. The

experimental results demonstrated that the refurbishing process extended the remaining useful life of the test specimens. It was observed that the RCF lives of the refurbished specimens approached the fatigue lives of the pristine specimens at the greater grinding depth since most of the damaged material is removed. However, it should be noted that this conclusion is valid only for the conditions where the case depth of the specimens is significantly higher than the contact half-width and refurbishing depths.

In the analytical investigation, a 2D elastic-plastic FE model based on damage mechanics was developed to predict the RCF lives of pristine and refurbished AISI 8620 case carburized steel specimens. A sectioning approach was used to simulate the point contact using the 2D line contact model. The estimated RCF lives of both pristine and refurbished domains corroborated well with the experimental results for different grinding depths.

Analysis of the experimental and analytical results suggests that the RCF lives of refurbished specimens depend on the relative depth of regrinding, the contact half-width and the case depth of the material. It was observed that increasing the depth of the regrinding enhances the remaining useful life of the refurbished test specimens. Consequently, a well-designed refurbishing process can improve the life expectancy of case carburized bearings.

4. A 3D EFFICIENT FINITE ELEMENT MODEL TO SIMULATE ROLLING CONTACT FATIGUE UNDER HIGH LOADING CONDITIONS

4.1 Introduction

Most of the mentioned numerical RCF models in chapter one utilized a two-dimensional simplification of the material microstructure. Weinzapfel et al. [77] extended the damage mechanics based RCF model by incorporating a 3D Voronoi Tessellation for material microstructure. Bomidi et al. [78] implemented several strategies to improve the efficiency of Weinzapfel's et al. [77] modeling approach. Warhadpande et al. [79] and Bomidi et al. [80] included the effect of plasticity to accurately capture the stresses in the contact region under high loads.

These models were developed to predict the RCF life of REBs in elastic or elastic-plastic conditions. Moyar and Sinclair [128] demonstrated that cyclic loading during RCF can lead to cummulative plastic deformation. Radhakrishnan et al. [129] experimentally investigated and indicated that plastic deformation affected the track width during RCF. Radhakrishnan and Ramanathan [129], Moyar and Sinclair [23] and Lorösch [130] showed that as plastic strain accumulated with increasing fatigue cycles, dimensions of the contact geometry changed and track width gradually increased. Furthermore, Bhattacharyya et al. [131,132] developed an experimental and numerical approach to predict accumulation of plastic strain in RCF. Donzella, et al. [133] demonstrated that plastic deformation induced compressive residual stresses in the contacting bodies. Merwin et al. [134] obtained residual stresses due to contact pressure in an elastic-plastic model. Warhadpande et al. [135] considered residual stresses due to high preloads from FEM RCF model and compared their results with experimental measurements. These studies highlight the significance of considering the effect of plastic deformation accumulation and the induced residual stresses in rolling contact fatigue. Therefore, in this investigation, a combined experimental and numerical approach was developed to estimate the fatigue life of bearings under high load conditions.

In this chapter, the TBTA was used to conduct high load RCF experiments on through hardened AISI 52100 steel specimens. Another series of specimens were then tested for different

numbers of RCF cycles. In these tests, the variations of contact width due to plastic deformation were measured using an optical surface Profilometer. In the analytical part of this investigation, a 3D efficient elastic-plastic model was developed to estimate the RCF lives of through hardened steel at a high load condition. A new meshing approach was developed to enhance the computational efficiency of the 3D model for line and circular contacts. The current model includes the effects of variation of contact pressure and residual stresses due to the plastic deformations. The results from the analytical model corroborate well with the experiments under high load conditions.

4.2 Experimental Investigation

This section describes the thrust bearing test apparatus, specimens and the experimental procedure for the RCF tests.

4.2.1 Thrust Bearing Test Apparatus

In order to study the rolling contact fatigue of through hardened steel material and also to investigate the effect of high applied loads on contact configurations during fatigue cycles, the thrust bearing test apparatus (TBTA) described in section 3.2.1, Figure 3.1, was used.

4.2.2 Specimen Description

AISI 52100 through hardened steel flat specimens were used in this investigation. The specimens were heat-treated, spheroidize-annealed and tempered martensite with less than 15% retained austenite. Figure 4.1 depicts the flat specimen geometry and a CAD bearing contact with the flat specimen. The test surface was carefully ground and polished prior to testing. Table 4.1 contains the mechanical and geometric properties of the specimens.

(a)

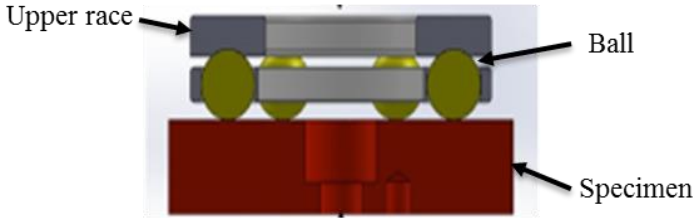

(b)

Figure 4.1: Flat specimen geometry: (a) testing surface, (b) Schematic of the contacting bodies

Table 4.1: Specimen properties and geometry

Specimen Parameters	Value
Elastic Modulus (GPa)	210
Poisson's Ratio	0.3
Yield Strength (GPa)	2.0
Specimen Diameter (in)	1.8
Specimen Thickness (in)	0.375
Specimen Roughness ($R_a\ \mu m$)	0.25 - 0.28

4.2.3 RCF Test Procedure and Results

In order to accelerate the RCF testing, the experiments were conducted at high loads. Based on the geometry of bodies in contact, the calculated Hertzian circular contact width and maximum pressure were 380 µm and 5GPa respectively. The spindle speed was set at 3450 rpm and the lubricant used is Mobil Jet Oil II (synthetic). The upper race and balls in the cage were components of 51201 thrust ball bearing, single direction. The balls are made of AISI 52100 through-hardened bearing steel. Flat specimen, the upper race, and balls were replaced with a new set for each test. Table 4.2 contains the experimental conditions, the dimensions of the balls and the upper race. Twenty-one RCF tests were conducted to determine the baseline fatigue life scatter of the flat through hardened specimens.

Table 4.2: Experimental Parameters

Experimental Parameters	Value
Bearing OD (upper race)	28 mm
Bearing ID (upper race)	12 mm
Ball Radius	5.556 mm
Number of Balls	10
Applied Load (per ball)	374.43 N
Spindle Speed	3450 rpm
Oil type	Mobil Jet Oil II (synthetic)

The scatter in the fatigue lives of bearings is generally characterized by the Weibull distribution slope. Smaller Weibull slopes indicate more scatter in the data. Figure 4.2 depicts the Weibull probability plots for the RCF lives of the AISI 52100 flat specimens obtained from the experiments.

Table 4.3 contains the Weibull slopes and L_{10} lives of the same. The L_{10} life is 9.13 million cycles and the Weibull slope is 1.53. It is to be noted that the Weibull slope is in the range typically observed in RCF experiments (0.7 - 3.5) [126].

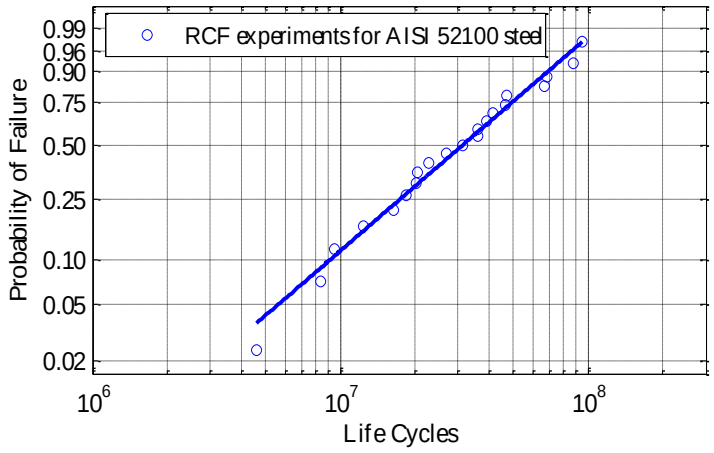

Figure 4.2: Weibull Probability plot of RCF lives for Through hardened AISI 52100 steels obtained from thrust bearing test apparatus.

Table 4.3: Comparison of experimental and analytical results of RCF with effects of plastic deformation

	Number of Tests	Weibull slope	L_{10} life (cycles)
Experimental	21	1.53	9.13E+06
Analytical (a = 50 μm)	33	1.91	1.72E+07
Analytical (a = 207 μm)	33	1.91	7.41E+06

The yield strength of the flat specimens used in this investigation is 2GPa. Based on the maximum shear stress theory, plastic deformation will occur when the maximum Hertzian pressure (P_{max}) is greater than 3.3GPa. The P_{max} during the experiments was 5GPa, which lead to a considerable plastic deformation in the specimens. In order to investigate the effects of plastic deformation on the contact configuration, a new set of RCF tests were performed on the 52100 flat specimens. Each test was conducted until a specified number of cycles. Four RCF tests were performed for each prescribed cycle number (10^3, 10^4, 10^5, and 10^6 cycles). A track was formed on the specimen's surface corresponding to the specified number of fatigue cycles. The surface profile of each track was evaluated using an optical Profilometer to examine the variation in the track profile as a function of RCF cycles. Figure 4.3c illustrates the surface track profiles for various fatigue cycles. The results indicate that the depth and width of the tracks increased as a function of cycles. Figure 4.3a and Figure 4.3b demonstrate that the initial grinding patterns remained on the surface during RCF tests. This indicates that a sufficient lubricant film separated the ball and flat specimen. Hence, wear was not responsible for increasing the track width during fatigue cycles [128].

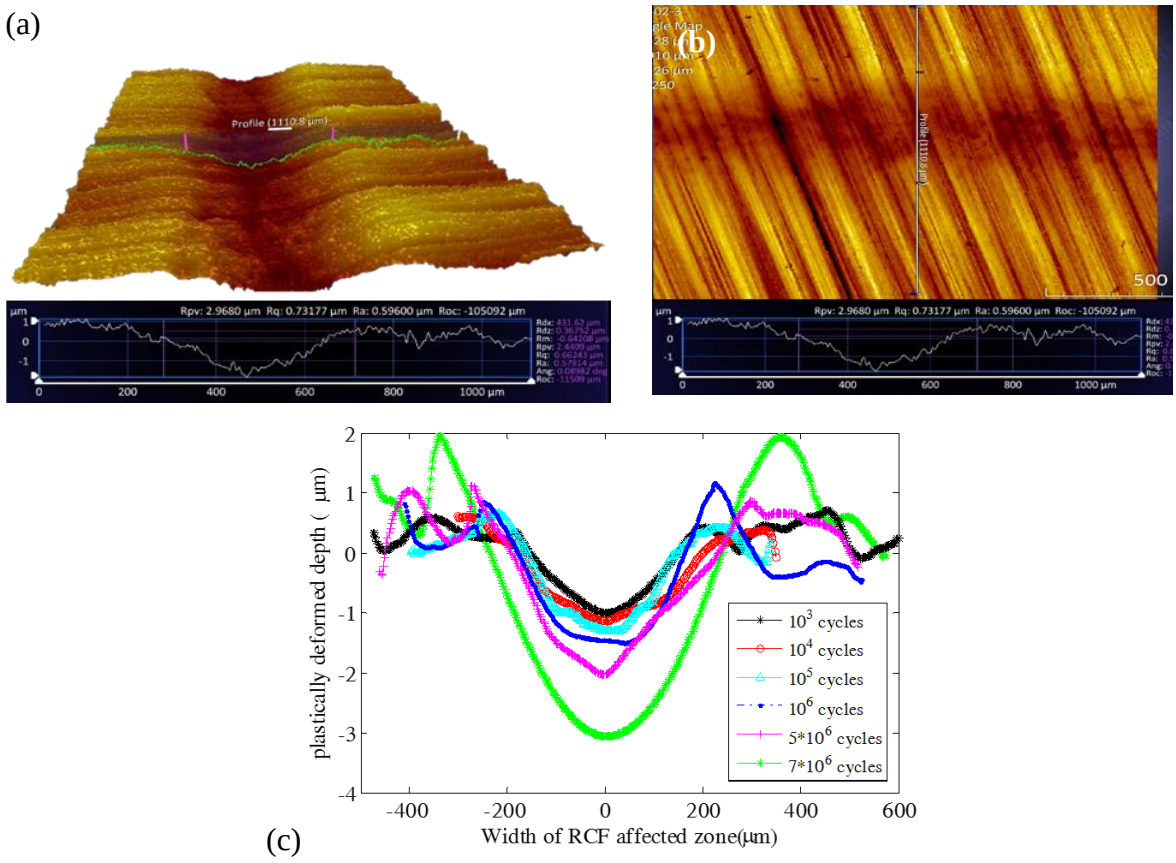

Figure 4.3: Experimental RCF track profile analyzed using an optical surface Profilometer (a) 3D view of the surface track profile at 10^5 cycles (b) top view at 10^5 cycles (c) at different test cycles

The results demonstrate that the accumulation of plastic deformation with RCF cycles is the cause for this increase [131]. Furthermore, the plastic strain accumulation below the contact region increases by the ratcheting phenomena [128–132].

In order to substantiate this hypothesis and observation, an elastic-plastic FE model was developed using ABAQUS to simulate a ball in contact with a flat under the same conditions as experiments. Figure 4.4a depicts the 2D axisymmetric model used for this simulation. A cyclic load was applied to the ball to determine the effects of load on surface profile/deformation. The stress-strain response of AISI 52100 was modeled as a linear elastic and linear kinematic hardening plastic (ELKP) material [93,136], where $E = 200\ GPa$, hardening modulus, $H = 10\ GP$a and the yield strength, $S_y = 2\ GPa$. The results indicate that the depth and the width of the deformation increased with increasing cycles due to the accumulation of plastic strain in the contact region. In

the first few cycles, the depth of plastic deformation increased quickly however, the rate of this increase decreased due to the plasticity. Figure 4.4c illustrates a comparison between the elastic plastic deformations obtained from the FE simulation and the experimental results at two different cycles.

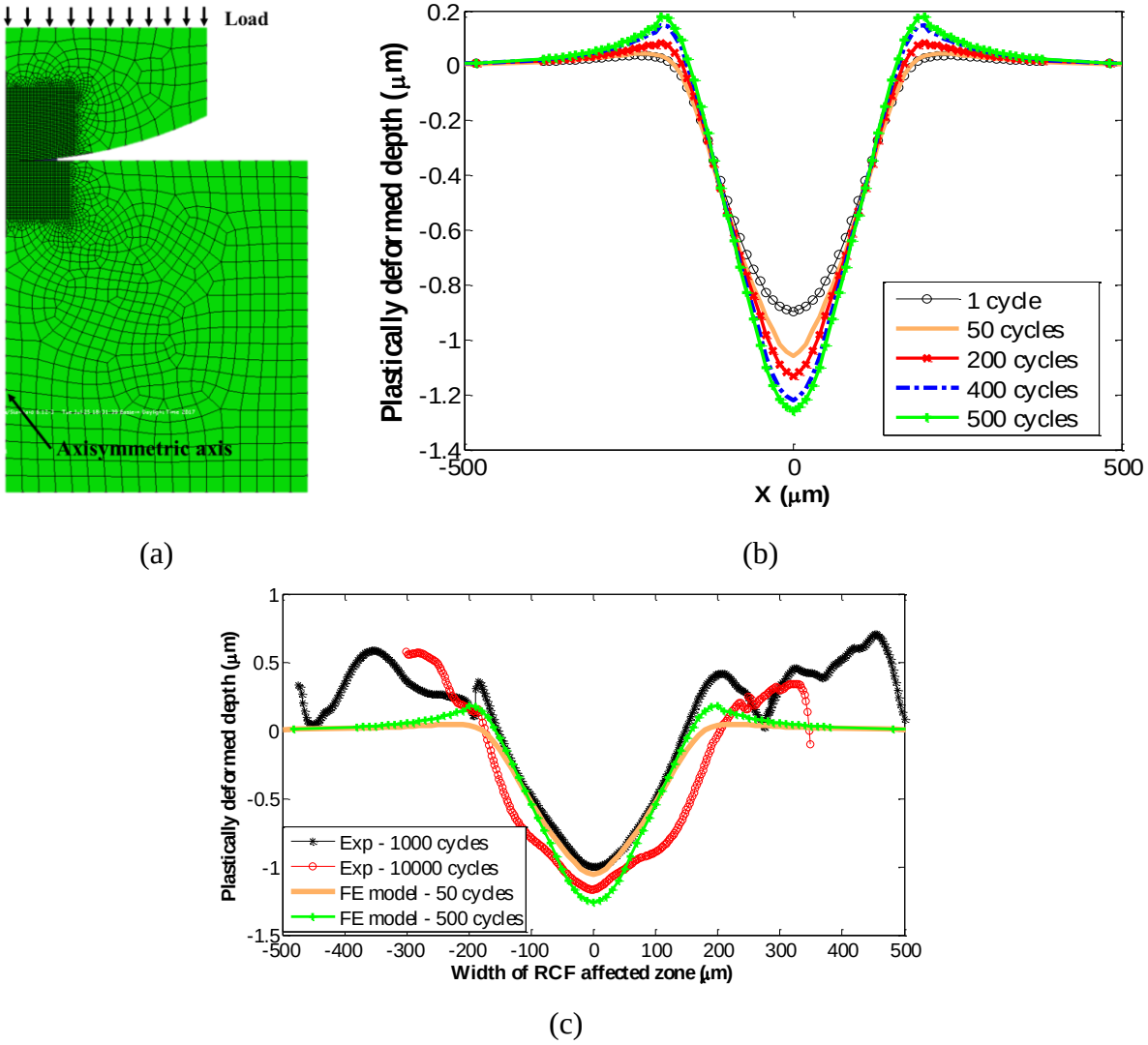

Figure 4.4: (a) 2D axisymmetric model for simulation of circular contact (b) plastically deformed surface in contact simulation at different cycles (c) comparison of RCF surface profile of experiments and FE elastic- plastic model at two different cycles

The results demonstrate that the depth and the width of the plastically deformed surface profile obtained from ABAQUS FE Model are quite comparable to the experimental results. Therefore, the cause of a track width and depth increase is due to high loads. It is to be noted that

the number of cycles obtained from the simulations are different from the experimental cycles. That is, the surface profiles obtained from the FE simulations depict more deformation in fewer cycles than the experiments. This difference can be attributed to phase transformations in the material due to rolling contact fatigue [137,138]. These transformations have influences on mechanical and microstructure [137–139] properties of the materials. Furthermore, the stress-strain model used in this study does not capture the strain-hardening in AISI 52100 specimen accurately. In addition, the trace of balls on the specimen's surfaces may not be the exact same tracks in fatigue cycles due to the surface profile deformation, the apparatus vibrations, subtle differences in ball diameter and specimens surface roughness, etc. Moreover, the surface profile evolutions occur in the specimens while the balls are rolling continually on the specimens whereas the FE model simulates only the surface deformation due to repeating contact at a single point. These may account for the variation in analytical and experimental results at the specific cycle.

Figure 4.5 illustrates the evolution of measured track width with RCF cycles. In each specimen, the track width was determined by averaging twelve different measurements of the surface track profile at different locations. The experimental results show that the contact width increases as cycles increase. In this study, the applied load remained constant for the duration of the RCF tests. The progressive increase in the contact widths with increasing cycles (Figure 4.5) will influence the contact pressure experienced by the test specimens. The contact geometry was assumed circular contact (ball on flat surface) during the RCF experiments in order to calculate the contact pressure distribution. However, this contact altered to an elliptical contact due to the surface plastic deformation.

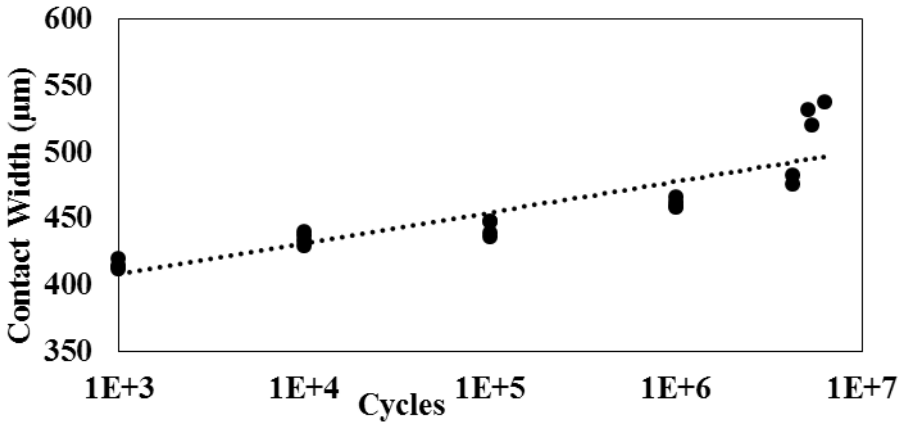

Figure 4.5: Variation of Contact width with RCF cycles

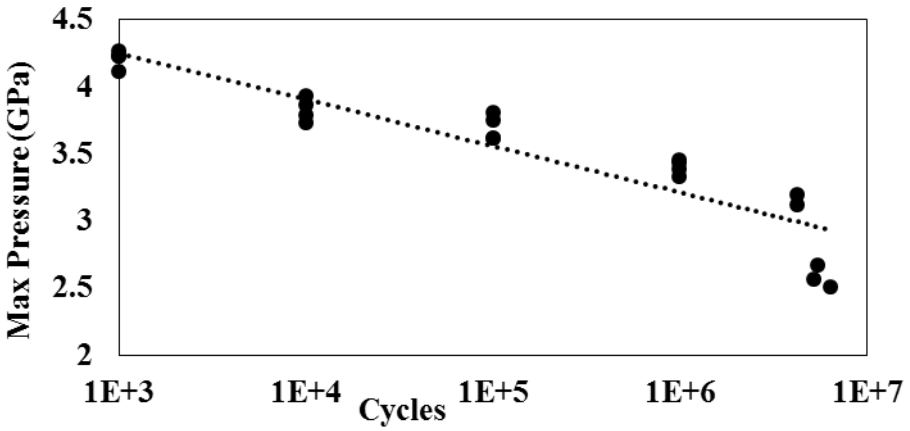

Figure 4.6: Variation of Hertzian Pressure with RCF cycles

The Hertzian maximum pressure between the ball and flat specimen was calculated using [7]:

$$P_{max} = \frac{3W}{2\pi a^2} \tag{4.1}$$

where W is the load, a is the radius of the circular contact between the ball and the flat specimen. The measured contact widths obtained from the experiments (Figure 4.5) were substituted in Equation (4.1) to obtain the corresponding maximum Hertzian pressure during RCF cycles. Figure 4.6 shows the maximum calculated pressure reduction as a function of cycles. The averaged contact width at 1000 cycles was 414 µm and the corresponding P_{max} is 4.2 GPa using Equation (4.1). As the plastic deformation continues to accumulate, the track width gradually increased to 461 µm at 1 million cycles. Beyond 1 million cycles, the contact width seems to increase at a higher rate to 540 mm at 6.4 million cycles corresponding to a maximum pressure of 2.5 GPa. It is speculated as the cycles increase, material at the center have work hardened and thus the periphery to the contact region deform [131,132]. This reduction in P_{max} prolongs the RCF lives of the specimens. The experimental results corroborate well with other published work [128–132]. It should be noted that, the actual contact width ($2a$) and pressure (P_{max}) for the first contact cycle differs from the calculated hertzian contact parameters (P_{max} = 5 GPa, $2a$ = 380 µm) due to plastic deformation [130].

4.3 Analytical Investigation

In this study, a 3D elastic-plastic finite element model based on the continuum damage mechanics was developed to predict RCF life of REBS. In the following sections, microstructure model, simulation of a rolling pass, the RCF damage model for through hardened material incorporating the effects of pressure variation and residual stresses due to plastic deformation are described. For a more comprehensive model description, please refer to Slack et al. [112], Weinzapfel et al. [77,88,92], Bomidi et al. [80], and Walvekar et al. [111].

4.3.1 Microstructure Topology Model

In the current investigation, Voronoi tessellation [84,85] was utilized to simulate the randomness and geometric disorder present in the material microstructure. This geometric representation of microstructure has been widely used in numerical investigations [86,87] to capture its effects on fatigue life dispersion. In this approach, a set of randomly generated seed points are placed in the Euclidian space. This space is then divided into cells with the criterion that every point in a specific cell is closer to the seed point of that cell than any other seed points. These generated cells are called Voronoi cells. The Voronoi cells and their boundaries represent the grain and grain boundaries, respectively, [47,54,77,87]. The average diameter of the Voronoi cells was set to 10 microns, which is the measured average grain size in bearing steels [114].

An improved version of the material microstructure generator [92] was developed to construct the 3D domain from Voronoi tessellations. Note that there were some patchy meshes due to Voronoi tessellation; however, the mesh was regionalized by eliminating the shortest edges of the Voronoi cells [92,140]. Therefore, the minimum angle of the elements was limited to above 20 degrees to ensure the quality of the elements [140]. The representative volume element (RVE) is the critically stressed area during a rolling pass, hence, the RVE was only meshed using Voronoi tessellation [78]. The regions beyond the RVE were meshed using cubic Voronoi tessellation with constant strain tetrahedron (CST) elements. The dimensions of the 3D model for line and circular contacts are listed in Table 4.4. To simulate an infinitely wide material subjected to an infinitely wide pressure distribution in the line contact loading, periodicity boundary condition was applied transverse to the direction of rolling [92]. Therefore, the width of the line contact model was restricted to the contact width to reduce computational efforts.

Table 4.4: 3D Model dimensions

Dimension	Microstructure topology region (RVE region)		Simulation domain	
	Point Contact	Line Contact	Point Contact	Line Contact
X (length)	(-1.55*a*, 1.55*a*)	(-1.55*a*, 1.55*a*)	(-4*a*, 4*a*)	(-5*a*, 5*a*)
Y (width)	(0, 1.55*a*)	(-0.5*a*, 0.5*a*)	(0, 3*a*)	(-0.5*a*, 0.5*a*)
Z (depth)	(-1.55*a*, 0)	(-1.55*a*, 0)	(-3*a*, 0)	(-4*a*, 0)

After a computational domain has been developed, the Voronoi cells were discretized into tetrahedral elements for finite element analysis. A new meshing strategy was developed to reduce the computational effort while retaining an acceptable accuracy in the subsurface stress field. In order to generate the tetrahedral mesh for this study, the faces of each grain were divided into Delaunay triangles connected to the center of the Voronoi grain. However, in the previous approach [77,80,88,92], the central node of each face was connected to the face vertices to generate triangles on a grain face and then connected to the center of the grain. Figure 4.7 illustrates these differences in meshing approach.

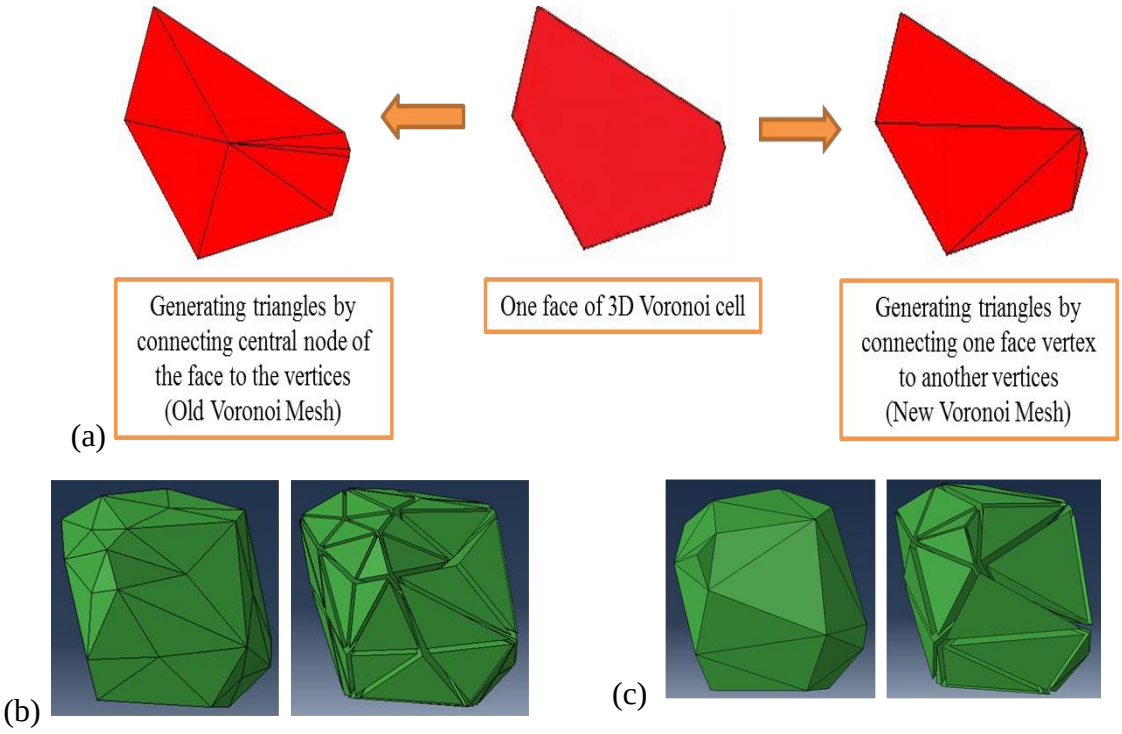

Figure 4.7: different strategies to mesh a Voronoi grain (a) generating triangle on the grain face to form the bases of the tetrahedral mesh shown in 3D Voronoi grain and exploded view (b) previous model (c) new model

With these modifications, the number of elements used to approximate the solution in the FEM was significantly reduced and subsequently the computational time was decreased. The subsurface stresses and computational effort of the current model were evaluated and compared with the previous model [78] for line and circular contacts. Figure 4.8 illustrates the 3D domains used in the current model.

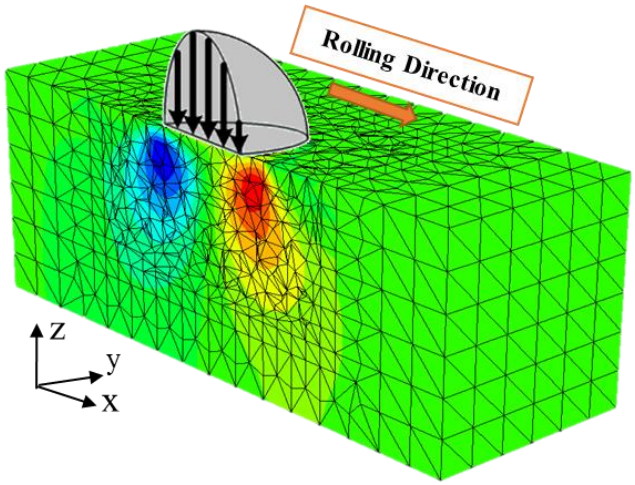

(a)

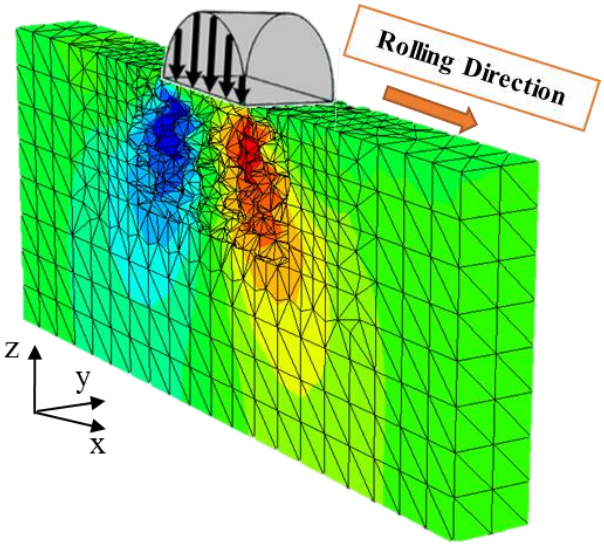

(b)

Figure 4.8: 3D Microstructure topology model (a) circular contact domain (b) line contact domain

4.3.2 Simulation of a Rolling Pass

ABAQUS finite element was employed to determine the subsurface stress distribution in a Hertzian contact. The normal surface traction for the circular and line contact defined by Equations (4.2) and (4.3) respectively were applied using ABAQUS subroutine UTRACLOAD.

$$p_z(x,y) = P_{max}\sqrt{1-\left(\frac{x-x_c}{a}\right)^2-\left(\frac{y-y_c}{a}\right)^2} \tag{4.2}$$

$$p_z(x,y) = P_{max}\sqrt{1-\left(\frac{x-x_c}{a}\right)^2} \tag{4.3}$$

where (x_c, y_c) is the location of the center of the Hertzian pressure distribution, (x, y) is the coordinate where the pressure is evaluated, P_{max} is the maximum Hertzian pressure, and a is the half-contact width (contact radius). The pressure distribution was translated over the surface at 21 discrete steps from $-2a$ to $2a$ in the rolling direction to simulate a rolling pass. The shear surface traction in the rolling direction is prescribed by;

$$t_{xy}(x,y) = \mu_s|p_z(x,y)| \tag{4.4}$$

where μ_s is the coefficient of friction and was set to 0.05 for a well lubricated contact [82,83]. The boundary conditions for the 3D microstructure model for line and circular contact are listed in Table 4.5. All displacements on the lower boundary of the model were fixed, and periodicity constraints were required in the rolling directions to effectively simulate the response of a semi-infinite, elastic half space [92]. It is noted that due to symmetry only half of the domain was modeled for circular contact which allowed significant savings in computational effort.

Table 4.5: 3D Model boundary conditions

Model	Extent					
	-X	+X	-Y	+Y	-Z	+Z
Point Contact	Periodic	Periodic	(Y=0) Symmetric	Fixed	Fixed	Surface traction
Line Contact	Periodic	Periodic	Periodic	Periodic	Fixed	Surface traction

The von Mises plasticity with linear kinematic hardening was employed in the FE model to incorporate the effects of material plasticity [79,136]. Furthermore, the variation of maximum pressure and contact width with fatigue cycles were included in the RCF modeling. The calculated maximum pressures (Figure 4.6) obtained from the experimental contact widths (Figure 4.5) were averaged at each specific cycle and then utilized in this simulation. Figure 4.9 depicts the 2D hemispherical pressure distributions for circular contact at different numbers of cycles. Note that,

the maximum pressure (P_{max}) of the first contact cycle is lower than the calculated Hertzian contact pressure (P_{max} = *5 GPa*) due to plastic deformation beneath the contact region. The contact width continues to increase for elastic-plastic material due to the presence of plastic strains in the contact region and consequently this increase reduces the maximum pressure [130]. The maximum pressures in the modeling in Figure 4.9were obtained from Figure 4.6.

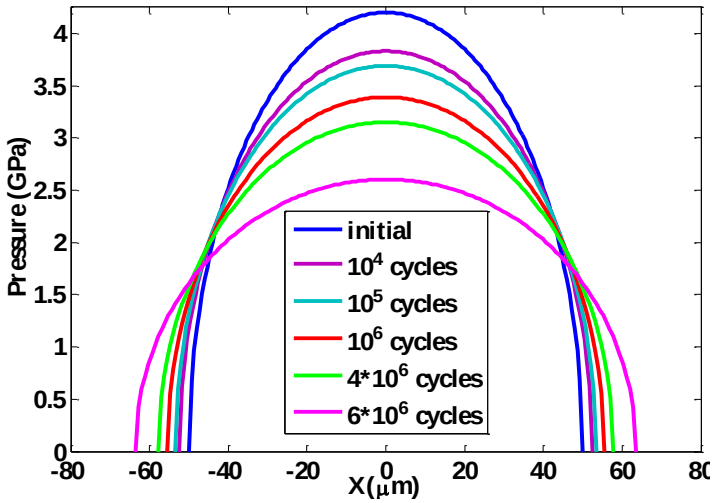

Figure 4.9: Variation of 2D sections of Hertzian Pressure profile with RCF cycles

4.3.3 Fatigue Damage Model

In this investigation, the continuum damage mechanics (CDM) was implemented to describe the material degradation due to rolling contact fatigue [45,46]. Damage mechanics attempts to model the influence of microscopic failure on the homogenized response of a material through the use of the damage variable, D. In high cycle fatigue, the evolution of damage at a point in the material is provided by an appropriate rate law. In elastic materials, the damage evolution is dependent only on the state of stress. However, if the material undergoes yielding, the damage is dependent on the state of stress as well as on the accumulated plastic strain. Hence, two different damage rate laws were used in this investigation. The plastic strains induced in the material can form as residual stresses [135,141] and these stresses can vary during RCF cycles due to the accumulation of plastic strains [142,143]. Therefore, the damage evolution laws were

modified, incorporating the effects of mean stresses due to the presence of residual stresses resulting from plastic deformations.

As described in the previous investigations [1,26,62,75], it is believed that shear stress reversal is the critical stress responsible for RCF. Furthermore, it is assumed that the grain boundaries constitute weak planes along which the fatigue damage can be advanced. Therefore, the elastic damage evolution law under rolling contact loading is [125] can be written as;

$$\frac{dD}{dN} = \left[\frac{\Delta\tau}{\tau_{r0}(1-\frac{\sigma_m}{S_{us}})(1-D)}\right]^m \tag{4.5}$$

where N is the number of cycle, $\Delta\tau$ is the shear stress reversal along the Voronoi grain boundary, τ_{r0} and m are material parameters that must be experimentally determined, σ_m is a mean stress due to the presence of residual stresses and S_{us} is the ultimate strength in shear. τ_{r0} is the resistance stress [48] that represents the ability of a material to resist the damage accumulation.

The plastic strain based damage law is given by [45,80,93]:

$$\frac{dD}{dN} = \left[\frac{\sigma_{\max}^2}{2ES_0\left(1-\frac{\sigma_m}{S_{us}}\right)^2(1-D)^2}\right]^q \dot{p} \tag{4.6}$$

where σ_{max} is the maximum von Mises stress over a fatigue cycle, $\dot{p}$ is the accumulated equivalent plastic strain over a fatigue cycle, S_0 and q are material dependent parameters and E is the undamaged modulus of elasticity.

In order to determine the mean stress in the Equations (4.5) and (4.6), the residual stresses due to plastic strains were obtained as follows [135]

$$\sigma_x^{res} = -\frac{E}{(1+\nu)(1-2\nu)}\left[(1-\nu)\varepsilon_x^P + \nu\varepsilon_y^P + \nu\varepsilon_z^P\right]$$

$$\sigma_y^{res} = -\frac{E}{(1+\nu)(1-2\nu)}\left[(1-\nu)\varepsilon_y^P + \nu\varepsilon_x^P + \nu\varepsilon_z^P\right] \quad (4.7)$$

$$\sigma_z^{res} = -\frac{E}{(1+\nu)(1-2\nu)}\left[(1-\nu)\varepsilon_z^P + \nu\varepsilon_y^P + \nu\varepsilon_x^P\right]$$

where E is the undamaged modulus of elasticity, ν is the Poisson ratio, and ε_i^P is the plastic strain in the direction of i. The hydrostatic component of the residual stresses is considered as the mean stress used in Equations (4.5) and (4.6)

The material parameters (τ_{r0}, m, S_0 and q) in Equations (4.5) and (4.6) were determined using experimental data from torsion fatigue. Figure 2.3 illustrates the experimental torsion SN curve for through-hardened AISI 52100 bearing steel [97]. The procedure to evaluate the damage parameters from the torsion SN curve is provided in [47,79,80,88,93]. Note that there is no mean stress due to residual stress for this torsion SN curve. The material parameters of AISI 52100 specimens are listed in Table 4.6.

Table 4.6: Material damage parameters for through hardened AISI 52100 specimens evaluated using Torsion SN data (Figure 2.3)

Material property	Value
Material grain diameter (μm)	10
Elastic modulus (GPa)	200
Poisson's ratio	0.3
Hardening modulus (GPa)	10
Yield Strength (GPa)	2
τ_{r0} (GPa)	5.979
m	11.1
S_0 (GPa)	0.0899
q	3.2

The rolling contact fatigue simulation requires solving the damage rate law equations (Equations (4.5) and (4.6)) and constitutive relationships simultaneously for each element. For the numerical implementation of the RCF modeling, a modified version of the iterative jump-in-cycles procedure developed by Lemaitre [45] was utilized. In this approach, the stress-strain response of the model and the material damage state are presumed to be constant over a block of cycles. The specific details of this algorithm can be found in [79,80,88,144]. Furthermore, once the damage value of an element reaches one, a crack initiation occurs in this model. After that, cracks propagate through the material microstructure and when the first crack reaches the surface, the simulation ends.

4.4 Results and Discussion

The main purpose of this investigation were to develop a 3D efficient finite element model based on the damage mechanics to corroborate the analytical and experimental results obtained from the TBTA. However, in order to achieve these objectives, an efficient 3D model based on the new meshing strategy was developed. This model was then evaluated and compared with the results from previous investigations in order to determine the accuracy and efficiency of the new model.

The 3D elastic-plastic RCF damage model described in the previous section was compared to the previous model [78,80] for validation. The subsurface stresses for the Hertzian line and circular contacts were determined for material properties listed in Table 4.6. Figure 4.10Figure 4.11(a, c) and 4.11 (a, c) illustrate the subsurface von Mises and orthogonal shear stresses contours for the circular and line contact pressure distributions, respectively. The variation of internal stresses (σ_x, σ_y, σ_z, and τ_{max}) along the centerline for the circular and line contacts were compared with previous models' results [78] and the elasticity theory [7]. Figure 4.10Figure 4.11(b, d) and 4.11 (b, d) depict these comparisons. The resulting stress fields for line and circular contact at two different locations demonstrated that the stress fields were nearly identical regardless of the location of the applied load. For circular contacts, the stresses of the current model are in a good agreement with the previous model and with the analytical solutions. For the line contact, the σ_x and τ_{max} showed some slight differences from the analytical results however, the results demonstrated similar trends with the results from the previous model [78].

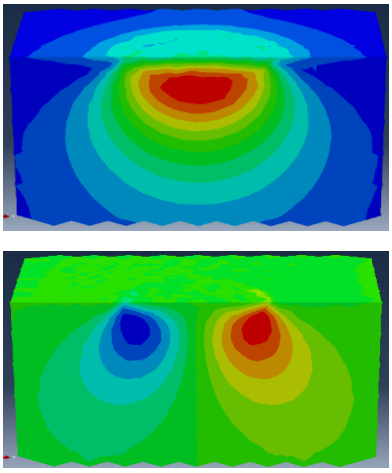

(a)

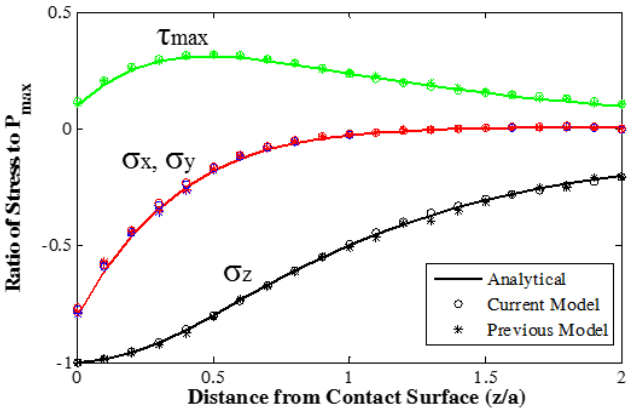

(b)

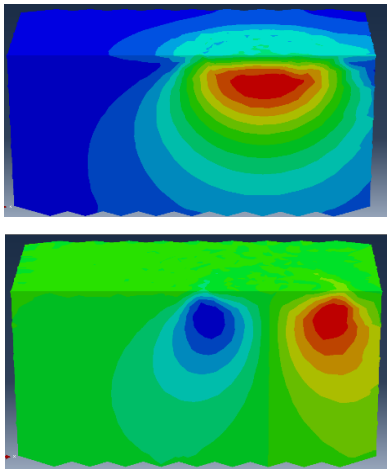

(c)

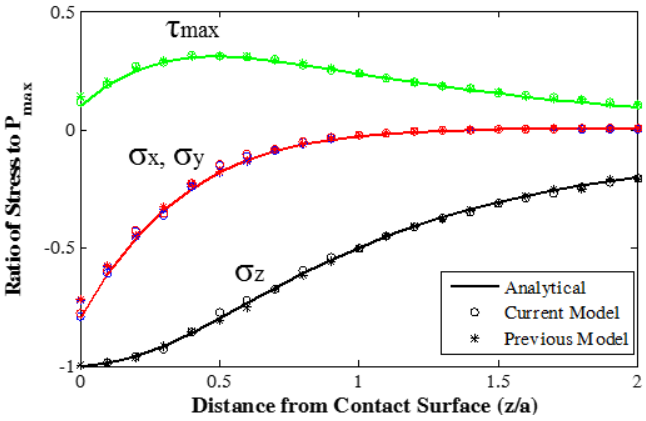

(d)

Figure 4.10: The subsurface stresses for circular contact at y=0 (a) von Mises and orthogonal shear stresses at x_c=0 (b) comparisons of the internal stresses along the centerline at x_c=0 (c) von Mises and orthogonal shear stresses at x_c=a (d) comparisons of the internal stresses along the centerline at x_c=a

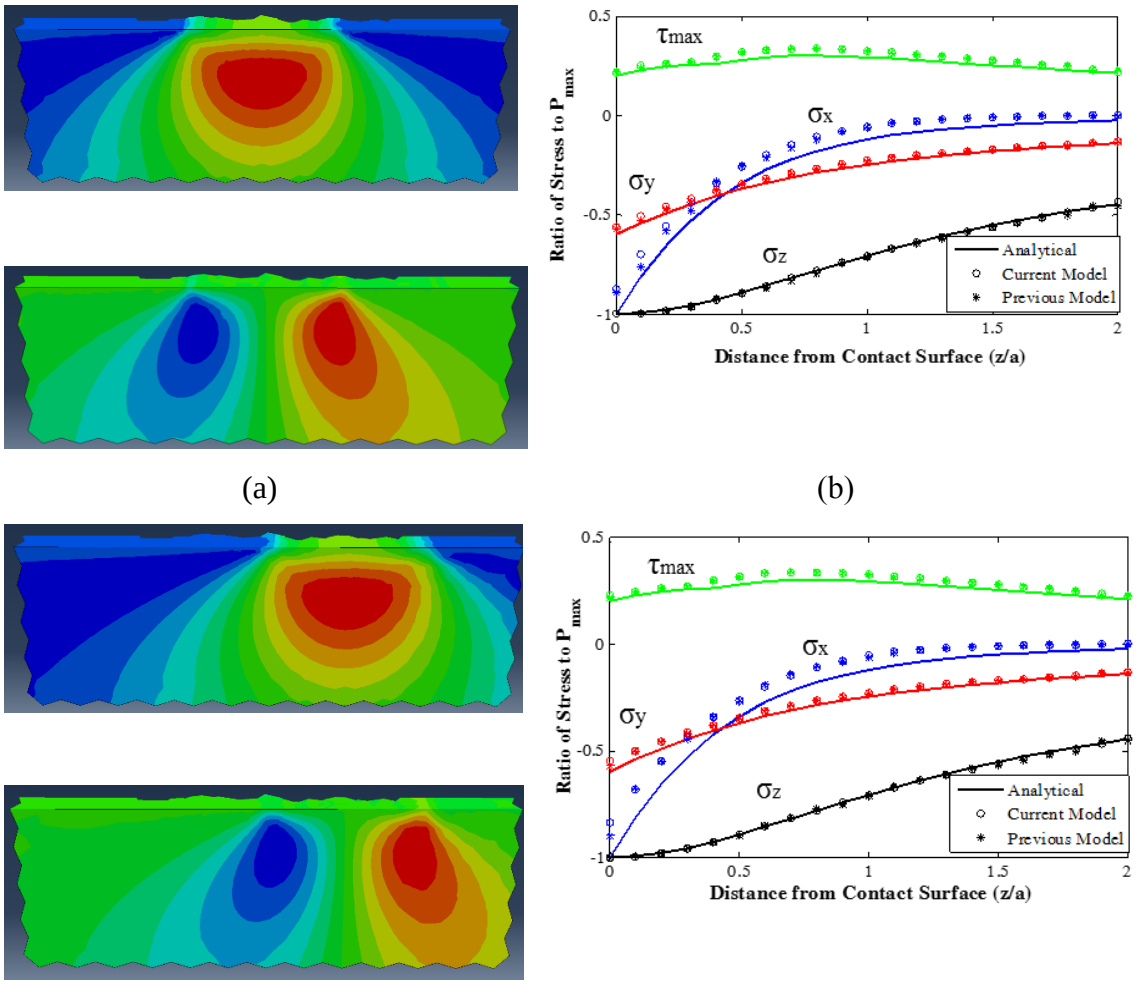

Figure 4.11: The subsurface stresses for line contact at y=0 (a) von Mises and orthogonal shear stresses at x_c=0 (b) comparisons of the internal stresses along the centerline at x_c=0 (c) von Mises and orthogonal shear stresses at x_c=a (d) comparisons of the internal stresses along the centerline at x_c=a

Note for better comparison with theory, the model dimensions and mesh density need to be significantly increased to have a slight improvement in the stress fields for line contact results [80,92]. The root mean squared (RMS) errors in these comparisons at various locations of applied contact pressure are listed in Table 4.7. The RMS error for the current model is close to the previous model's error [78]. Hence, the prediction of the internal stress fields in the current model are in good agreement with Hertzian line and circular contact loading.

Table 4.7: RMS Error of the model results in comparison with analytical solutions at different load locations

Model		σ_x	σ_y	σ_z	τ_{max}
X=0 , Y=0	Line Contact _ current mesh	7.220E-02	2.150E-02	7.800E-03	2.710E-02
	Line Contact _ old mesh	5.990E-02	1.680E-02	7.900E-03	2.700E-02
	Circular Contact _ current mesh	1.480E-02	1.810E-02	1.390E-02	9.200E-03
	Circular Contact _ old mesh	1.070E-02	1.250E-02	9.700E-03	7.800E-03
X=*a* , Y=0	Line Contact _ current mesh	7.650E-02	2.290E-02	8.300E-03	2.790E-02
	Line Contact _ old mesh	7.040E-02	2.100E-02	7.700E-03	2.730E-02
	Circular Contact _ current mesh	1.230E-02	1.550E-02	1.040E-02	8.100E-03
	Circular Contact _ old mesh	1.890E-02	2.120E-02	7.200E-03	1.130E-02

The advantage of the current modified microstructural model is a significant reduction in computational expenses to simulate an RCF cycle. Table 4.8 contains the comparison of the computational time for a single load pass between the current and previous models for both circular and line contacts. The results indicate that the simulation time for a single load pass was decreased by 70% for the circular contact and 44% for the line contact.

Table 4.8: Comparison of computation time for a single load pass

Model	CST Element	LST Element	Integration Points	Run time (min)
Line Contact _ current mesh	3120	23762	98168	2.8
Line Contact _old mesh	5984	40382	167512	5
Circular Contact _ current mesh	6156	43566	180420	7.5
Circular Contact _ old mesh	24968	106766	452032	24.75

In order to evaluate the ability of the current model in predicting the RCF lives, 33 microstructure domains for line contact were generated using the Voronoi tessellation procedure. The simulation parameters were set identical to Bomidi et al. [78] (e.g. $P_{max}= 2\ GPa$). The damage rate law for elasticity (Equation (4.5)) was utilized in this comparison to predict the RCF life in

such a low pressure. Please note, Bomidi et al. [78] could not simulate RCF life for point contacts due to the significant computational effort required. However, with the meshing strategy developed for this investigation, RCF life for circular contacts is possible. Figure 4.12 illustrates the initial and final life results for a line contact obtained from the previous [78] and current models. The fatigue lives correlate well with the numerical results from Bomidi et al. [78].

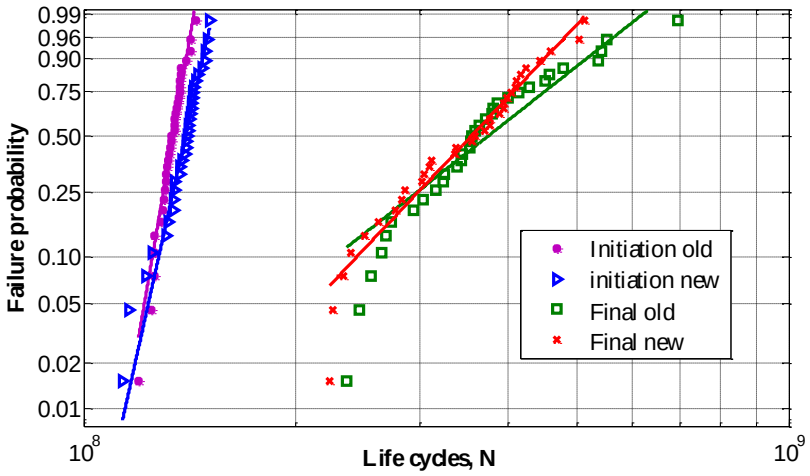

Figure 4.12: Comparison of RCF lives between previous and current models for line contacts

The L_{10} life and the Weibull slope for both models are listed in Table 4.9. The predicted L_{10} life and the calculated Weibull slope of the initial and final lives were close to the previous model [78]. As described earlier, the larger the slope, the lower the scatter. Therefore, the estimated fatigue lives of the 3D model demonstrate less scatter than the range typically observed in RCF experiments (0.7 - 3.5) [126]. This difference could attribute to the assumptions of the analytical model. The material in the simulation was assumed free of any inclusions, defects, and micro voids and only geometric variation in microstructure topology characterized the fatigue life scatter. Therefore, the RCF life comparison verifies that the model's predictions were not affected significantly by implementing the new strategy to enhance the computational efficiency.

Table 4.9: Statistical comparison of initiation and final life prediction between new and old mesh

Test Type	Previous Model	New Model
Number of Domains	33	33
Max Hertzian Pressure (GPa)	2	2
Half Contact Width (μm)	50	50
Weibull Slope (initial)	27.9	21.49
L_{10} Life (initial)	1.25E+08	1.28E+08
Weibull Slope (final)	3.75	5.02
L_{10} Life (final)	2.27E+08	2.44E+08

In order to predict the RCF life of specimens used in the TBTA at high load, the FE model was used to simulate the operating conditions of the experimental investigation. As described earlier, the loading conditions considered for this investigation, induces plastic deformation on the test specimen. The accumulations of the plastic strains caused a variation in contact width during fatigue cycles as depicted in Figure 4.5. The maximum pressures (Figure 4.6) calculated from the measured contact width were implemented in the 3D model to represent the variation in contact pressure distribution as shown in Figure 4.9. Furthermore, the residual stresses resulting from plastic strains were included in the simulation using Equation (4.7). In order to characterize the fatigue life dispersion of the AISI 52100 specimens, 33 random microstructure domains were constructed for circular contact. The estimated life distribution of the circular domains at high load compared to the experiments is depicted in Figure 4.13.

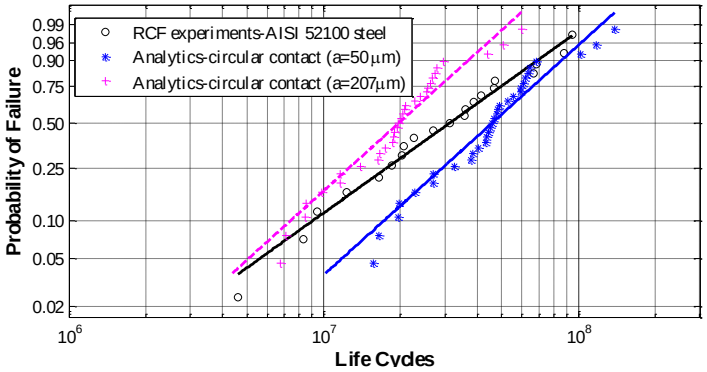

Figure 4.13: Comparison of RCF lives of the efficient 3D model (a= 50 μm) and modified predicted RCF life using ISO 281 (a=207 μm) with experiments at high load (5 GPa)

Table 4.3 contains the Weibull parameters for analytical and experimental results. The L_{10} life and the Weibull slopes for the analytical RCF lives are 1.72E+07 and 1.91 respectively. This predicted RCF life cannot be compared with experimental results. Since the contact widths used in these simulations were chosen to be smaller than the actual contact widths in the experiments in order to save computational effort. At the start of the simulation, the contact width of 50 microns was used. For the subsequent load passes, the contact width was increased by the same ratio as observed in the experiments and P_{max} used in the simulation (Figure 4.9) was set to the same as those calculated from the experiments (Figure 4.6).

In order to compare the analytical results to the experiments, the estimated fatigue lives from the 3D model need to be modified to consider the actual size of contact width. Therefore, a relationship between half contact width (a) and basic life rating (L_{10}) for a fixed maximum Hertzian pressure (P_{max}) for thrust ball bearing was formulated using the ISO 281 standard [145].

The equation for calculating half contact width (a) between two spheres in contact is defined by;

$$a = \left(\frac{3WD'}{2E'}\right)^{\frac{1}{3}} \quad \rightarrow \quad W = \frac{2a^3E'}{3D'} \tag{4.8}$$

$$D' = \frac{2r_1r_2}{r_1 + r_2} \quad , \quad \frac{1}{E'} = \frac{1-\nu_1^2}{E_1} + \frac{1-\nu_2^2}{E_2} \tag{4.9}$$

where W is applied load, D' is the equivalent diameter, r_1 and r_2 are the radius of spheres and E' is the equivalent stiffness. Substituting W from Equation (4.8) into Equation (4.1) gives

$$P_{max} = \frac{E'a}{\pi D'} \tag{4.10}$$

From Equations (4.1) and (4.10), the half contact width "a" is proportional to applied force (W) and the equivalent diameter (D') for a constant P_{max}.

$$W \propto a^2 \quad , \quad D' \propto a \tag{4.11}$$

Now, the basic life rating (L_{10} life) for ball bearing is defined as [145]

$$L_{10} = \left(\frac{C_a}{P_a}\right)^3 \tag{4.12}$$

where C_a is basic dynamic load rating and P_a is dynamic equivalent load. C_a for a thrust ball bearing is given by;

$$C_a = b_m f_c Z_1^{\frac{2}{3}} D_w^{1.8} \tag{4.13}$$

where D_w is the ball diameter, Z_1 is the number of balls, b_m is the bearing type factor, and f_c is a coefficient determined from processing accuracy and material of bearing parts. Considering a thrust bearing that the radial dimensions of all components are scaled equally, the only variable in Equation (4.13) changes with the bearing size is D_w and the rest of the terms remain constant. Equation (4.14) demonstrates the relationship between C_a and half contact width (a) by considering Equation (4.11).

$$C_a \propto D_w^{1.8}, \qquad D_w \propto D' \qquad C_a \propto a^{1.8} \tag{4.14}$$

The other parameter used in Equation (4.12) is dynamic equivalent load (P_a). Based on RCF experiments in TBTA and the contact geometry between flat specimen (lower race of thrust ball bearing) and the balls, the P_a is the load (W) applied to the contact. Therefore, the dynamic equivalent load (P_a) is proportional to half contact width (a) using Equation (4.11)

$$P_a = W \qquad \rightarrow \qquad P_a \propto a^2 \tag{4.15}$$

Using these relationships in Equation (4.12) the relationship between L_{10} and half contact width "a" with fixed P_{max} can be written as;

$$L_{10} = \left(\frac{C_a}{P_a}\right)^3 \quad \rightarrow \qquad L_{10} \propto \left(\frac{a^{1.8}}{a^2}\right)^3 \quad \rightarrow \quad L_{10} \propto \left(\frac{1}{a}\right)^{0.6} \tag{4.16}$$

Hence, for the same P_{max}, the L_{10} lives are shorter for the larger Hertzian contact size. In this study, Equation (4.16) was utilized to modify the predicted fatigue life from 3D model. It is worth mentioning that, the initial contact geometry was used to calculate the life factor in this simulation. The initial maximum pressure was the same in the experiment and simulation (P_{max}=

4.2 GPa), and the half of the contact width in the simulation and experiments were respectively 50μm and 207μm. However, other contact width values provide the same life factor at each specific fatigue cycle because the ratio of the contact width in the simulation to the experiments for the corresponding cycle was constant. Figure 4.13 illustrates the modified life distribution compared to the experimental RCF lives. It can be observed that the estimated lives of circular domains are in good agreement with the experimental results.

4.5 Summary and Conclusions

The objectives of this study were to analytically investigate RCF of machine components subjected to high loads and corroborate the numerical and experimental results. A thrust bearing test apparatus was designed and developed to characterize the rolling contact fatigue behavior of through hardened steels. The TBTA was used to conduct RCF experiments on AISI 52100 specimens at a high load (~5 GPa) for different numbers of fatigue cycles. The experimental results indicated widening of the track width during RCF cycles, which causes a decrease in the contact pressure. These variations of contact width and pressure are caused by the accumulation of plastic deformation due to fatigue cycles. The experimental results obtained from TBTA are in a good agreement with previously published results.

A 3D elastic-plastic FE model based on the damage mechanics was developed to predict the RCF lives of AISI 52100 steel specimens at high load conditions. In order to compare the analytical and experimental results, the variation of contact pressure distribution and the residual stresses due to plastic strains were implemented in the simulation. Because of the circular contact geometry between the balls and flat specimens, the 3D model was modified to develop a computationally efficient RCF model for circular contact. The estimated RCF lives of through hardened domains corroborated well with the experimental results at high load conditions.

Experimental and analytical results suggest that the evolution of contact width is due to the plastic strains accumulation. This evolution has a significant influence on RCF lives of specimens by reducing the contact pressure and increasing compressive residual stresses induced by the plastic strain at high load conditions. Consequently, in order to accurately predict fatigue lives at high loads, it is critical to include the variation of contact width and pressure in the calculation, modeling and simulation.

5. A 3D FINITE ELEMENT MODEL FOR INVESTIGATING EFFECTS OF REFURBISHING ON ROLLING CONTACT FATIGUE

5.1 Introduction

The fatigue life due to the surface defects is significantly shorter as compared to the subsurface originated spalling in rolling-element bearings (REBs). In order to allow bearings to reach the useful estimated life and their critical failure mode (subsurface initiated spalling) [105], surface defects in components of bearings can be restored. In order to repair bearings, NASA proposed to grind the used bearings surfaces in the mid-1970s [98–100]. Since then, bearing restoration and refurbishment has become prevalent and has been applied in various applications such as aerospace, off-highway and construction equipment [101]. The bearing repair can be an effective method to bearing life. The new bearings replacement cost can be saved approximately 60% by using restored bearings. Furthermore, another advantage is the reduction of lead times for custom-made bearings [101].

Among different repair levels, level III which is explained in chapter 3 is more favorable because it improves significantly the RCF lives of REBs with lower costs. Furthermore, damaged surfaces caused by operating conditions can be repaired using level III repair. Therefore, this level of repair can prevent surface-initiated pitting which is a typical industrial bearing failure mode [104] and it allows for subsurface damages to play an important role after refurbishing and the refurbished bearings last to the ultimate failure mode (the subsurface-initiated spalling) due to the penetration of the damage below the maximum allowable grinding depth in bearings. However, the lack of information on the effects of the repairing process on bearing life has restricted the widespread implementation of bearing refurbishment.

Most of the refurbished bearings were studied and tested by specific industries for particular applications, therefore this experimental information cannot be generalized [106]. Furthermore, the analytical modeling of repaired bearings has also been quite limited. One of the first models to estimate the RCF life of refurbished bearing was proposed by Coy et al. [107]. In this model, the Lundberg-Palmgren equation was extended to calculate RCF damage of the outer race of repaired bearings using the grinding depth of refurbishment and the prior service time [108]. Then, Zaretsky [109] modified this model using maximum shear stress criteria to calculate the fatigue

damage of the inner and outer races and rolling elements as well. Kotzalas et al. [106] included the entire stress field and used the ISO 281:2007 standard to develop an analytical model. Since the nature of these models is empirical, they considered the fatigue life scatter using the Weibull probability distribution function without offering significant insights into the physical mechanisms responsible for RCF. Further, these models are assumed constant Weibull distributions for restored bearings obtained from the experimental original bearings.

Paulson et al. [105] recently proposed a two-dimensional elastic FE model to study RCF of refurbished bearings using continuum damage mechanics. In this model [105], the Weibull parameters for a group of bearings were calculated by incorporating microstructure topology using Voronoi tessellations. This model was extended to analyze the rolling contact fatigue behavior of case carburized refurbished bearings in a line contact [113]. In the model [113], the plasticity effects were included to determine the stresses and strains accurately in the contact area under high loads. It was illustrated that the refurbishment could extend the remaining bearings lives. Moreover, the fatigue life enhancement was higher for refurbished case carburized bearings with larger case depth compared to the repaired through hardened bearings. Golmohammadi et al. [146] conducted RCF experiments on refurbished case carburized steel to study the fatigue failure. They also proposed a novel idea [111] to predict the RCF life and spall formation in the circular contact utilizing a 2D line contact refurbished model and correlated the analytical experimental results. It was found that the relation between the grinding depth, the contact geometry and the material case depth were the key factors that affect the fatigue lives of refurbished case carburized steel. Their models were two-dimensional and used to predict the RCF life after refurbishment.

In general, the shape of Hertzian contact geometry is elliptical. However, the loading can be approximated as infinitely wide in the cases with a large ellipticity ratio which is applicable to the Hertzian line contact geometry. Therefore, the 3D elliptical Hertzian pressure distribution is required in order to simulate an elliptical contact in rolling contact fatigue accurately. Furthermore, the topology of material microstructure geometry is not planar. Hence, it is essential to avoid the limitations of a 2D framework in order to more accurately predict the RCF life of refurbished bearings.

In the current work, a 3D FE model was developed to study the refurbishment effects on rolling contact fatigue behavior of the through-hardened material in a circular contact geometry.

Please note that, simulating an elliptical contact has a further requirement that the one side of the 3D domain be sufficiently large in order to have enough Voronoi grains under the contact pressure distribution which causes a significant computational cost. Therefore, circular contact was investigated in order to reduce the computational cost and simplify the problem [78,88] . The material degradation from fatigue failure was simulated using continuum damage mechanics. In this model, Voronoi tessellation was used to represent the randomness of material microstructure in order to capture the fatigue life scatter. In order to predict RCF life of refurbished domains, fatigue lives of 3D pristine domains under circular contact were determined using the numerical model. After that, the damage state of each element was calculated at a specific fatigue cycle. Refurbishment process was applied on the pristine domains by removing a layer of material from the top surface while the calculated damage values were preserved in domains as an initial damage state of refurbished domains. Then restored domains were subjected to RCF loading to predict the fatigue life after refurbishing. A parametric study was investigated to analyze the effects of grinding depth, initial fatigue cycles and applied load.

5.2 Modeling Approach

In the current study, a 3D finite element model was developed to investigate the effects of refurbishing on RCF based on the continuum damage mechanics. In the subsequent sections, the modeling of material microstructure, the FE model used to simulate a rolling pass, the fatigue damage model for through hardened steel, and the refurbishment simulation are explained. The detailed description of the FE model is presented in Slack et al. [112], Weinzapfel et al. [77,88], Paulson et al. [105].

5.2.1 Material Microstructure Topology Model

The steel microstructure is modeled using Voronoi tessellation [84] to characterize the randomness and geometric disorder of the microstructure and to obtain the probabilistic failure and account for the scatter in rolling contact fatigue lives typically observed in RCF experiments [47,79,80,88,112]. Please note, Voronoi tessellation is well accepted as an approach to model the topology of the material grain structure to a good degree of accuracy [85,147,148] and it has been widely used in the fatigue simulation [86,87,89,114,149,150]. In Voronoi tessellation, a set of random seed points are generated in the Euclidian space. This space is then distributed into many

regions which all points of a specific region are closer to the seed point of that region than any other seed points. These divided regions are called Voronoi grains. The grain and grain boundaries in the material microstructure are defined by Voronoi tessellation [47,54,77,87,151]. The measured average grain size of bearing steel is 10 microns and therefore, that is used as the diameter of the Voronoi grains in this study [114]. In order to decrease computational expenses, random Voronoi grains were only meshed in the representative volume element (RVE) where is the critically stressed area during a rolling pass [78,93]. Cubic Voronoi tessellations with constant strain tetrahedron (CST) elements are used in the regions beyond the RVE. The Tetrahedral elements used in the RVE are 10-node quadratic tetrahedron elements (C3D10). Outside RVE region, a 4-node linear tetrahedron element (C3D4) is used in this study. A tie constraint was implemented between these two regions in order to ensure continuity in solution [78]. The dimension of the 3D model is listed in Table 5.1. Previous investigators, typically chose the depth of an RVE as half of Hertzian contact width (1a) [47,78,87], which is usually done for computational efficiency. However, in this investigation, the depth of RVE was increased to 2.5a in order to provide adequate microstructural depth for refurbished domains [105,146]. After the 3D domain was generated, the Voronoi grains were divided into tetrahedral elements using the proposed meshing strategy [152] for efficient finite element. Due to the variation of Voronoi grains shapes, angles and the number of polygon sides, constant mesh size is not used in this study. However the accuracy of the calculated internal stresses using the generated mesh was evaluated and validated [152]. The 3D domains used in this study for circular contact is illustrated in Figure 5.1.

Table 5.1: 3D Model dimensions for a point contact domain

Dimension	Microstructure topology region (RVE region)	Simulation domain
X (length)	(-1.55a, 1.55a)	(-4a, 4a)
Y (width)	(0, 1.55a)	(0, 3a)
Z (depth)	(-2.5a, 0)	(-4a, 0)

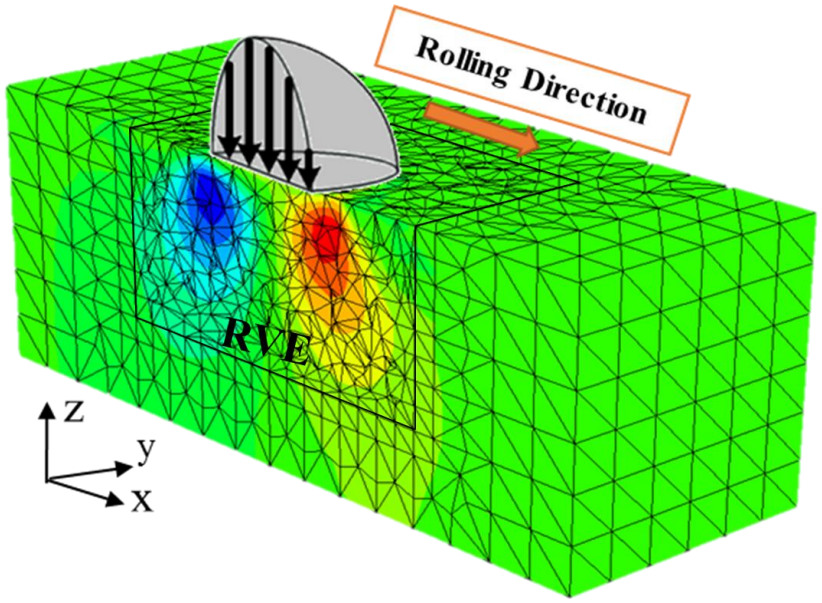

Figure 5.1: 3D Microstructure topology model for a circular contact domain

5.2.2 Simulation of a rolling pass

A 3D FE model was developed to simulate the contact between a ball and raceway in an REB using ABAQUS software. The Hertzian contact pressure was applied to the surface of ABAQUS FE Model as a normal stress component using the user subroutine UTRACLOAD. In order to simulate a rolling pass, the Hertzian pressure distribution was translated over the top surface from $-2a$ to $2a$ (a is the half-contact width) in 21 discrete steps in the rolling direction. The normal and shear components of the surface traction are defined by Equations (5.1) and (5.2), respectively.

$$p_z(x,y) = P_{max}\sqrt{1-\left(\frac{x-x_c}{a}\right)^2-\left(\frac{y-y_c}{a}\right)^2} \tag{5.1}$$

$$t_{xy}(x,y) = \mu_s|p_z(x,y)| \tag{5.2}$$

where (x_c, y_c) is the coordinate of the center of the Hertzian pressure distribution, P_{max} is the maximum Hertzian pressure and μ_s is the constant coefficient of friction. The coefficient of friction was defined as 0.05 to take into account the well lubricated nature of the contact [82,83]. All displacements at the lower side of the 3D domain are fixed. In order to accurately model the response of a semi-infinite elastic half space, the side boundaries in the rolling direction were periodicity constrained [92,152]. Please note that only half of the domain was simulated due to

the symmetry to reduce significantly the computational costs. The boundary conditions of the 3D microstructure model are listed in Table 5.2.

Table 5.2: 3D Model boundary conditions for a circular contact domain

Extent					
-X	+X	-Y	+Y	-Z	+Z
Periodic	Periodic	(Y=0) Symmetric	Fixed	Fixed	Surface traction

5.2.3 Fatigue damage model

In the current investigation, cracks initiation and propagation due to material degradation during rolling contact fatigue were simulated using the continuum damage mechanics [45,46]. CDM attempts to capture the influence of damage on the mechanical response of a material to model the microscopic mechanism of fatigue failure. In CDM, a damage variable *D* is presented in the constitutive equations to describe the current state of damage in the material. The damage variable has a range from 0 (undamaged) till 1 (fully damaged). In the microstructure model, when the damage of the element reaches the critical value (D_c=1), intergranular debonding (cracks) are generated using a mesh partitioning (MP) procedure [88]. In the MP procedure, the mesh geometry is divided along the grain boundary faces of the critically damaged elements by duplicating nodes and reestablishing the element connectivity. This procedure is repeated after each loading cycle and damage and cracks grow through the material microstructure. When the first crack reaches the top surface, final failure occurs and simulation ends. In MP procedure, a coulomb friction model is defined on the crack surfaces in order to prevent grains interpenetrating. This model is implemented in ABAQUS using a surface-to-surface contact pairs with a coefficient of friction of 0.4 [47,78,88], and a hard pressure-overclosure relationship.

In high cycle fatigue, the damage evolution of a point in the material is determined by an appropriate rate law. When the materials are under elastic conditions, the evolution of damage is a function of the state of stress. In rolling contact fatigue, the shear stress reversal resolved along the grain boundaries is assumed to be the critical stress component responsible for the damage fatigue [1,26,62,75]. The damage rate law under rolling contact loading is

$$\frac{dD}{dN} = \left[\frac{\Delta\tau}{\tau_{r0}(1-D)}\right]^{m} \tag{5.3}$$

where $\Delta\tau$ is the shear stress range along the Voronoi grain boundaries, N is the number of cycles, τ_{r0} and m are material parameters that determined from experiments. τ_{r0} is the resistance stress [48] that represents the ability of a material to resist the damage accumulation. Since the critical stress in rolling contact fatigue and torsional fatigue is the shear stress, the fatigue damage parameters can be evaluated using the experimental torsion SN curve. Figure 2.3 illustrates the torsion SN curve for through-hardened AISI 52100 bearing steel [97]. Using the same procedure as [47,80,88,105], the material parameters (τ_{r0} and m) of AISI 52100 are determined and listed in Table 5.3.

Table 5.3: Material parameters used in this simulation

Material property	Value
Material grain diameter (μm)	10
Elastic modulus (GPa)	200
Poisson's ratio	0.3
τ_{r0} (GPa)	5.979
m	11.1
Coefficient of friction	0.05
Half contact width (μm)	50

In this study, the simultaneous solution of the damage evolution equation and constitutive relationships are required for each element. In order to implement the numerical modeling of the RCF damage equations, a modified version of the jump-in-cycles algorithm outlined by Lemaitre [45] was employed. In this approach, the stress field is assumed to be constant over a finite number of cycles in a block i, ΔN_i. During this loading block, the damage of each element is also assumed to be constant and equal to D_e^i. Therefore, the damage evolution is piecewise linear with respect to the number of cycles as depicted in Figure 5.2. Please note that the shape of the damage evolution curve is determined from the numerical simulations due to the stress-damage coupling. In each block of cycles i, the stress solution is calculated for the current state of the body based on the material model, damage accumulation history and cracks due to broken joints from the previous

block of cycles. The damage evolution rate and maximum strain energy release rate for each element are calculated. After calculating the damage evolution rate for all elements, the element experiencing the maximum damage evolution rate is chosen as the most critical for the current block of cycles. The increment in damage ΔD is assumed to be constant over the block of cycles so the number of cycles in the current loading block is determined by dividing ΔD by the maximum damage evolution rate. Damage increment, ΔD, has to be selected large enough to reduce the computational time reasonably but small enough so that the coupling between damage and stress remains valid. The value of 0.2 is chosen for the damage increment in this study based on previous investigations [47,80,88,113]. For a detailed description of this algorithm, please refer to [79,80,88,144]. Please note that all the elements are considered undamaged at the beginning of the simulation.

5.2.4 Domain refurbishment

There are two main steps in the simulation of the domain refurbishment. The first step is to designate the fatigue cycles that refurbishing occurs (refurbishing cycles) and assign the correlative damage state of each element in the domain. The next step is to grind the surface of the pristine microstructure domain at the specific refurbishing depth. Each step is explained in the following sections to illustrate a better understanding of the numerical implementation of this procedure.

5.2.4.1 Initial damage state of refurbished domains

In order to predict the RCF life of the refurbished bearing, it is essential to determine the fatigue cycles prior to refurbishing and determine the corresponding damage for all elements in the domain. In order to determine the initial fatigue cycles prior to refurbishing, 33 random microstructural domains were subjected to RCF until the first crack reached the surface. Then, the L_{10} life of pristine domains was determined. The initial fatigue cycles or refurbishing cycles (N_{ref}) was defined as a percentage of the pristine life.

During RCF simulation, the damage evolution with respect to fatigue cycles of each pristine domain was determined. Figure 5.2 illustrates the damage growth for an element in the domain. Using this result, the damage value for each element is linearly interpolated at the given refurbished cycles. It is to be noted that Figure 5.2 is piecewise linear due to using the jump-in-

cycles method mentioned in the previous section. When the given refurbished cycles (N_{ref}) is between 0 and the fully damaged fatigue cycle (N_{crit}), the damage value is less that one. However, N_{ref} can be greater than N_{crit} and damage cannot go beyond one, therefore the element damage value is set to one. The accumulated damage of each element in the domain is calculated at refurbishing cycles and used as an initial damage value when the RCF simulation is begun for the refurbished domain.

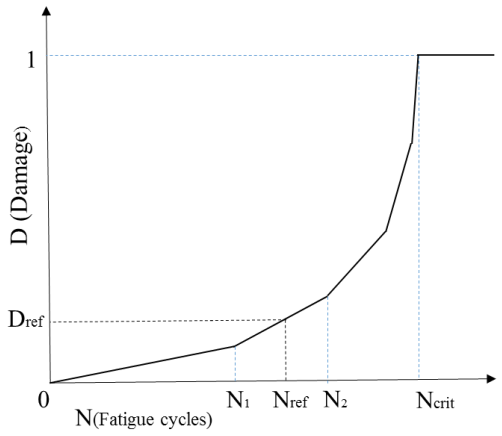

Figure 5.2: Damage evaluation curve and interpolated damage at refurbishing cycle

5.2.4.2 Simulation of refurbishing process

The refurbishing processes were duplicated by removing a top layer of the microstructure domain. In this process, the first step was to pass a plane through the Voronoi domain at the refurbishing depth. Some Voronoi grains were completely below the cut plane, some grains were entirely above that and others were crossed by the cut plane (partial grains). Therefore, there were three types of Voronoi grains in this approach. After recognizing these types, the first type was preserved in the domain and the second type was eliminated while the third type was modified to remove a section of partial grains that were beyond the cut plane. In order to modify the partial grains, a cutting Voronoi algorithm was developed. In this algorithm, geometric features of the Voronoi grains such as faces, edges, vertices were specified. Faces of a Voronoi grain are polygon surfaces on the periphery of the grain. The unique edges and vertices of the grain faces were designated as edges and vertices of the Voronoi grain.

The cutting algorithm was implemented in four steps approach on each partial Voronoi grain. First, vertices above the cut plane were duplicated and moved down along the edges of

Voronoi grain until they reached the intersection between the edges and the cut plane. Figure 5.3 illustrates this approach for a partial Voronoi grain. After that, the centroids of each new Voronoi grain were determined using the modified geometry. Then, new elements were generated on the upper boundary of partial grains at the cut plane using the efficient meshing strategy [152] mentioned in previous sections. Finally, the short edges algorithm [92] was applied to eliminate the shortest edges of the refurbished Voronoi grain in an attempt to generate a more uniform mesh and reduce the computational costs of the model. These procedures were implemented on each Voronoi grain to generate a refurbished domain. Figure 5.4 demonstrates an isotropic and front view of a section of the refurbished and original 3D microstructure. When the refurbishing process was modeled, the RCF damage simulation was resumed using the refurbished domain to estimate the fatigue life after refurbishing. The accumulated damage before refurbishing is preserved to account for the initial fatigue cycles of the simulation.

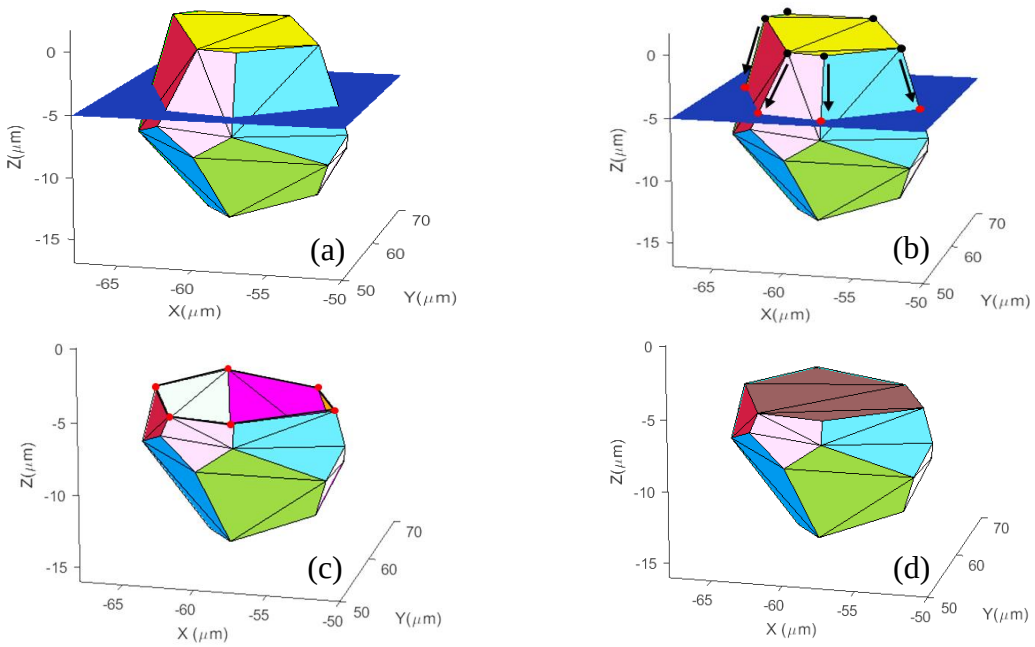

Figure 5.3: refurbishing process on a partial Voronoi grain (a) Pristine grain (b) moving down nodes above the cutting surface along the edges of grain faces (c) refurbished grain without top boundaries (d) refurbished grain

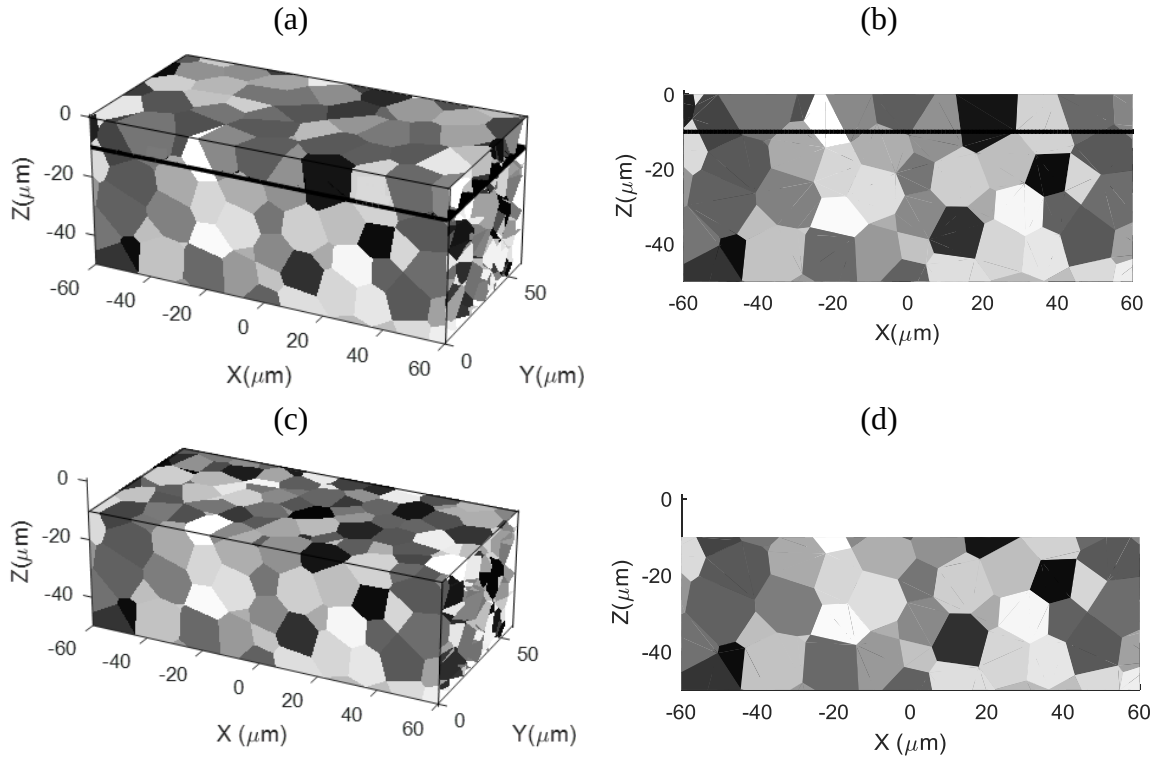

Figure 5.4: Pristine 3D microstructure (a) isotropic view, (b) front view and 3D Microstructure after refurbishing (c) isotropic view, (d) front view.

5.3 Results and Discussion

The 3D FE model developed was used to simulate the rolling contact fatigue of refurbished ball bearings made from through hardened steel. The variations of grinding depths and running times prior to the refurbishment were studied to evaluate their influences on the bearings RCF life and spall formation. Simulations are required to conduct for at least 30 unique domains to maintain a 94% lower confidence limit for a Weibull distribution for the fatigue life [151,153]. Hence, 33 random microstructure domains were generated to study fatigue life scatters of refurbished domains using the Voronoi tessellation procedure. It is essential to compare the current numerical results with experimental data and the solution of previously published models for pristine materials. In order to achieve that, 33 random Voronoi domains were used in the current model to predict the L_{10} life of pristine through hardened domains in a circular contact at different maximum contact pressures. Figure 5.5 illustrates the variation of L_{10} life for different contact pressures using the two parameters Weibull analyses for the current and the previously developed models [75,79,80,88,108] alongside the experimental data of the bearing fatigue tests [154]. Please note

that the significant scatter in the experimental fatigue life at the same load level can be due to many unknown factors, e.g. bearing application, lubricant cleanliness, etc. The results demonstrate that there is a good general agreement between the numerical models [75,79] calibrated using fatigue experimental results from 1950s era steel and the Lundberg-Palmgren model [108]. The experimental data presented by Harris and Barnsby [154] demonstrates an enhancement in the obtained fatigue life due to using bearings manufactured in the late 1960s from cleaner steels. Weinzapfel et al. [88], Bomidi et al. [80] and the current model which are based on the modern bearing steel properties corroborate better with the experimental data [154]. It should be noted that the predicted fatigue lives of the current model are higher than previous models [80,88] due to the different contact pressure distribution used in the line contact and the circular contact.

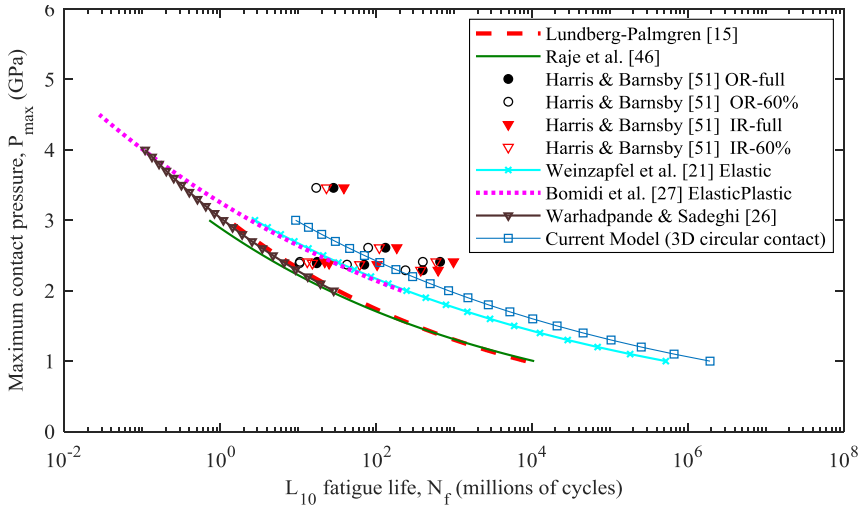

Figure 5.5: Variation of L_{10} life with contact pressures

After comparing the numerical results using current model with experimental data [154] for pristine materials, the developed 3D model for circular contact was used to predict the fatigue life for refurbished bearings. In this model, the half-contact width (a) was assumed constant at 50 μm and Maximum Hertzian pressure (P_{max}) was changed from 2.0 GPa to 3.0 GPa to analyze the fatigue performance of steel under different loads. First, the fatigue simulations were performed on 33 pristine domains to predict L_{10} life. Then microstructure domains were refurbished at 6, 12.5, and 25 μm (0.125a, 0.25a, 0.5a) below the original top surface. The fatigue cycles before

the refurbishing process were selected at 50% and 90% of the L_{10} life cycles of the pristine domains. The simulation parameters and material properties are listed in

Table 5.3. In order to calculate the L_{10} life of through hardened steel in a circular contact, a two-parameter Weibull distribution was used. The L_{10} lives of pristine domains at 2 and 3GPa were 8.62E+8 and 9.53E+6 cycles respectively and the Weibull slopes were 4.36 and 3.86 respectively listed in Table 5.4. Please note that the typical observed Weibull slope from RCF experiments are in the range of 0.7 to 3.5 [126]. Lower Weibull slope demonstrates higher scatters in the fatigue life. The predicted Weibull slopes are larger than the experimental range and consequently represent lower life scatters. The reason is that the 3D FE model assumed the microstructure domains were free of inclusions or other random defects and material properties were isotropic.

Table 5.4: Life prediction of pristine and refurbished domains

P_{max}	Domain	50% L_{10} cycles before refurbishment				90% L_{10} cycles before refurbishment			
		Weibull Slope	L_{10} Life (cycles)	Total L_{10} life (cycles)	life ratio $\frac{L10_{Tot}}{L10_{Pris}}$	Weibull Slope	L_{10} Life (cycles)	Total L_{10} life (cycles)	life ratio $\frac{L10_{Tot}}{L10_{Pris}}$
2 GPa	Pristine	4.36	8.62E+8	8.62E+8	1	4.36	8.62E+8	8.62E+8	1
	0.125a $_{ref}$	4.06	5.48E+8	9.58E+8	1.11	2.68	3.11E+08	1.05E+9	1.22
	0.25a $_{ref}$	2.62	6.99E+8	1.11E+9	1.29	3.29	4.30E+08	1.17E+9	1.36
	0.5a $_{ref}$	4.51	1.07E+9	1.48E+9	1.72	3.94	9.09E+08	1.65E+9	1.91
3 GPa	Pristine	3.86	9.53E+6	9.53E+6	1	3.86	9.53E+6	9.53E+6	1
	0.125a $_{ref}$	3.19	5.53E+6	1.00E+7	1.05	2.27	3.21E+06	1.13E+6	1.19
	0.25a $_{ref}$	3.15	7.51E+6	1.20E+7	1.26	2.46	4.05E+6	1.22E+7	1.28
	0.5a $_{ref}$	4.45	1.19E+7	1.64E+7	1.72	3.97	1.08E+7	1.89E+7	1.98

In order to investigate the effects of fatigue cycles before refurbishment, the accumulated damage up to 50% and 90% of $L_{10pristine}$ life was obtained at both loads. After preserving the damage accumulation, each domain was refurbished at the three grinding depths (0.125*a*, 0.25*a*, and 0.5*a*) as explained in the previous section. Figure 5.6 demonstrates the accumulated damage of the RVE region at 50% and 90% of $L_{10pristine}$ cycles in pristine and refurbished conditions of the same Voronoi domain with different grinding depths at 2GPa. It can be observed that most of the

damage areas of the pristine domain for both initial fatigue cycles are focused at the depth between 0.25*a* and 0.5*a* from the top surface. This behavior is expected because the critical depth in rolling contact fatigue of a circular contact is located at 0.35*a* from the top surface where the maximum shear stress reversal occurred. The damage values of the pristine and refurbished domains after 50% of $L_{10pristine}$ cycles are smaller than the domains after 90% of $L_{10pristine}$ cycles because the domain was subjected to fewer fatigue cycles. The range of damage of refurbished domains with grinding depths of 0.125*a* and 0.25*a* (6 and 12.5 μm) is almost the same and resembling the pristine domain damage at both fatigue cycles. Because the most damaged element in the pristine domain is usually near the critical depth (0.35*a*) that is below these grinding depths. Therefore, refurbished domains with a grinding depth smaller than 0.35*a* have a most damaged element below the regrind surface. However, most of the damage values were removed from the refurbished domain with the grinding depth of 0.5*a* and therefore the retained damage range is lower in this case.

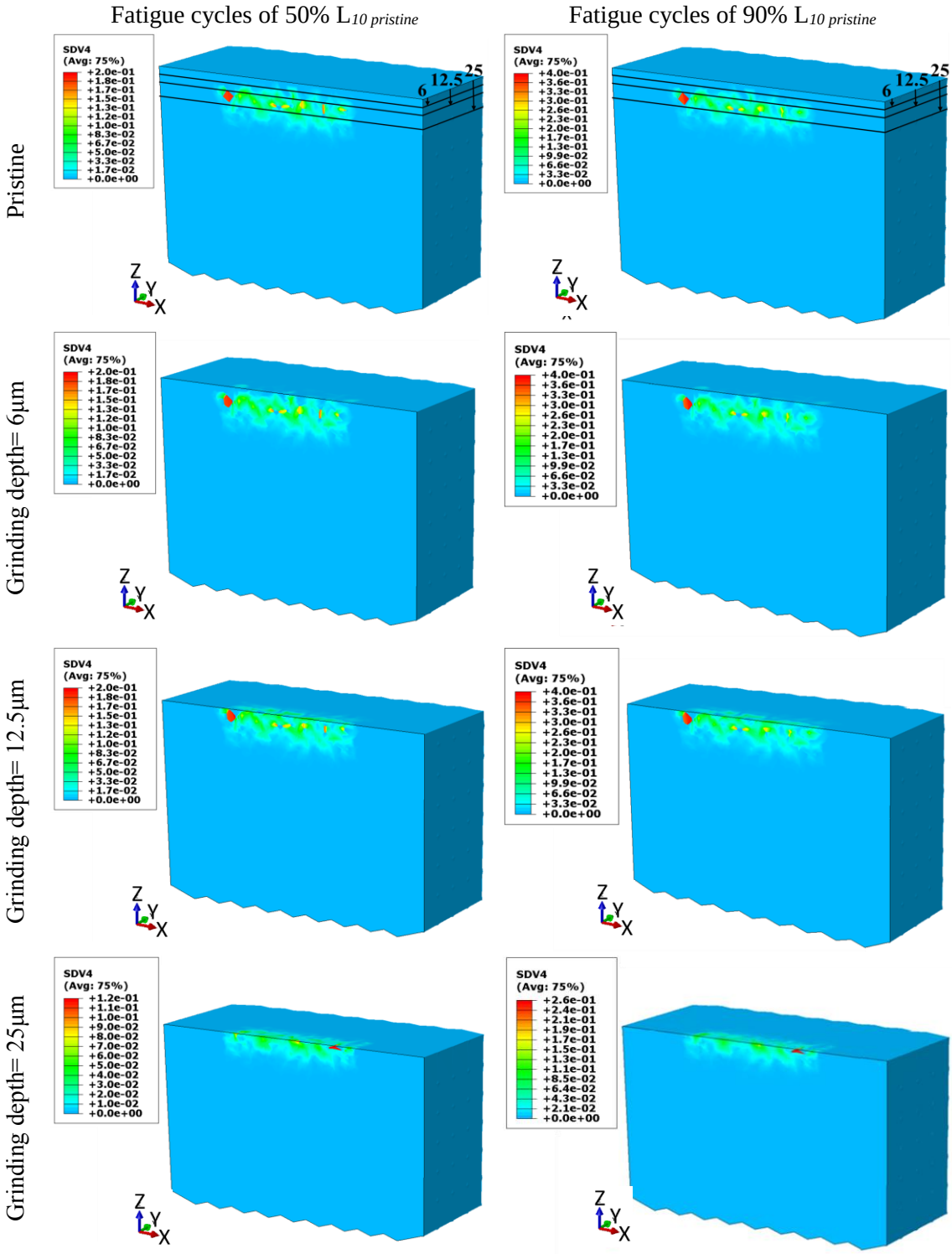

Figure 5.6: Accumulated damage in the RVE region at different fatigue cycles before refurbishing for a pristine and refurbished domain with different grinding depths at P_{max}= 2GPa

After generating the regrind domains with initial damage, the RCF cycling of refurbished domains was simulated to determine the RCF lives using the 3D damage model. Figure 5.7 illustrates the predicted lives of pristine and refurbished domains in a circular contact at 2GPa after 50% and 90% of $L_{10pristine}$ cycles prior to refurbishing. Please note that the calculated life for restored domains is the remaining life after refurbishment. For both initial fatigue cycles, RCF lives enhance with deeper grinding depths. Refurbished domains with 6 μm (0.125a) grinding depth has the lowest life in this study due to the extent of initial damage of refurbished domains. Most of the damage remained in the restored domain with 0.125a grinding depth as shown in Figure 5.6. By removing more materials from the surface, more damaged elements due to the initial fatigue cycles are eliminated leading to increase fatigue life. The predicted L_{10} lives of refurbished domains with the grinding depth of 25 μm (0.5a) after 50% and 90% of $L_{10pristine}$ cycles at 2GPa are longer than others because as shown in Figure 5.6 the part of the material critically damaged prior to refurbishment are removed at this grinding depth which is greater than the critical depth, 0.35a. Therefore, refurbished domains with these conditions behave similarly to pristine domains under rolling contact fatigue. Table 5.4 list the L_{10} life and Weibull slope of pristine and refurbished domains at different scenarios. As explained above, the range of the Weibull slope typically observed in RCF experiments is 0.7–3.5 [126] however the experimental data presented by Harris and Barnsby [154] for bearings manufactured from carbon vacuum-degassed AISI 52100 steel shows a range between 0.51 and 5.7 for Weibull slopes which include the model's estimations for pristine and refurbished lives. It should be noted that the reason that predicted Weibull slopes are closer to the upper range is the assumption of free of any inhomogeneities in the simulation. In the current model, it was assumed that only geometric variation in microstructure topology was considered as a source of fatigue life scatter.

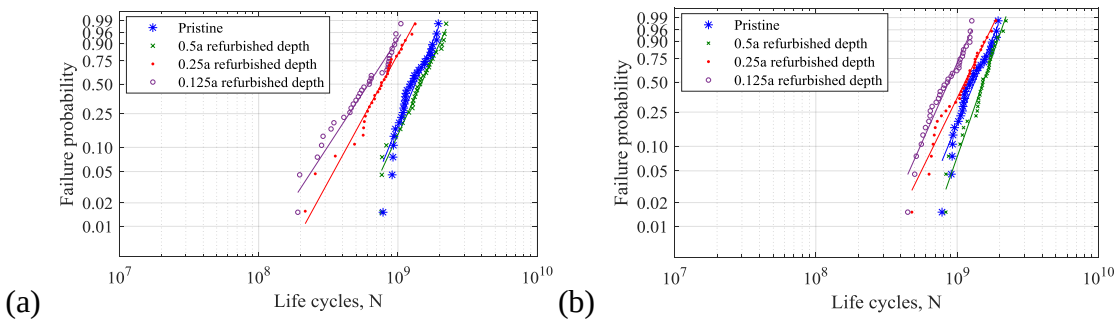

Figure 5.7: Fatigue life of pristine and refurbished domains at 2GPa with running time of (a) 90% L_{10} cycles before refurbishing (b) 50% L_{10} cycles before refurbishing

Furthermore, the results demonstrate that the remaining fatigue lives of restored domains after 50% of $L_{10pristine}$ cycles before refurbishing are more significant than 90% of $L_{10pristine}$ cycles for the grinding depths of 0.125a and 0.25a. For the grinding depths beyond the critical depth, the life differences are negligible at different initial fatigue cycles. These results can be clarified by evaluating the state of accumulated damage prior to refurbishing indicated in Figure 5.6. However, the total life of refurbished domains, the summation of fatigue cycles before and after refurbishing, are larger at the initial 90% of $L_{10pristine}$ cycles. The life ratio which is the ratio of the total L_{10} life of refurbished domains with respect to L_{10} life of pristine domains demonstrates the performance of refurbishment. Evaluating of this parameter reveals the refurbishment process can extend the total fatigue life of bearings at both initial fatigue cycles and also at various grinding depths. These results are in a good qualitative agreement with numerical observations from the literature [105,113,146].

Increasing load causes severe damage in pristine domains leading to reduce the fatigue life. Figure 5.8 depicts the predicted lives for pristine and refurbished domains at 3GPa under different initial fatigue cycles. Results demonstrate that refurbished domains at P_{max}= 3GPa behaved similarly to restored domains at P_{max}= 2GPa since microstructure domains were in the elastic region under both loads. It can be observed that the fatigue lives at P_{max}= 3GPa are improved by removing more materials from the surface. Furthermore, remaining fatigue life after refurbishment is higher at less initial fatigue cycles (50% of $L_{10pristine}$) however, their total lives are lower comparing to refurbished domains with the initial 90% of $L_{10pristine}$ cycles. Table 5.4 contains the remaining and total L_{10} lives of pristine and refurbished domains at 3GPa under different grinding depths and initials fatigue cycles. The results indicate that the RCF lives were extended due to the

refurbishing process for all of the scenarios. However, life enhancement is lower at a higher load. The reason is that pristine domains subjected to a higher load have greater damage values prior to refurbishment. Hence, the larger initial damage state of restored domains causes a reduction in the predicted RCF life.

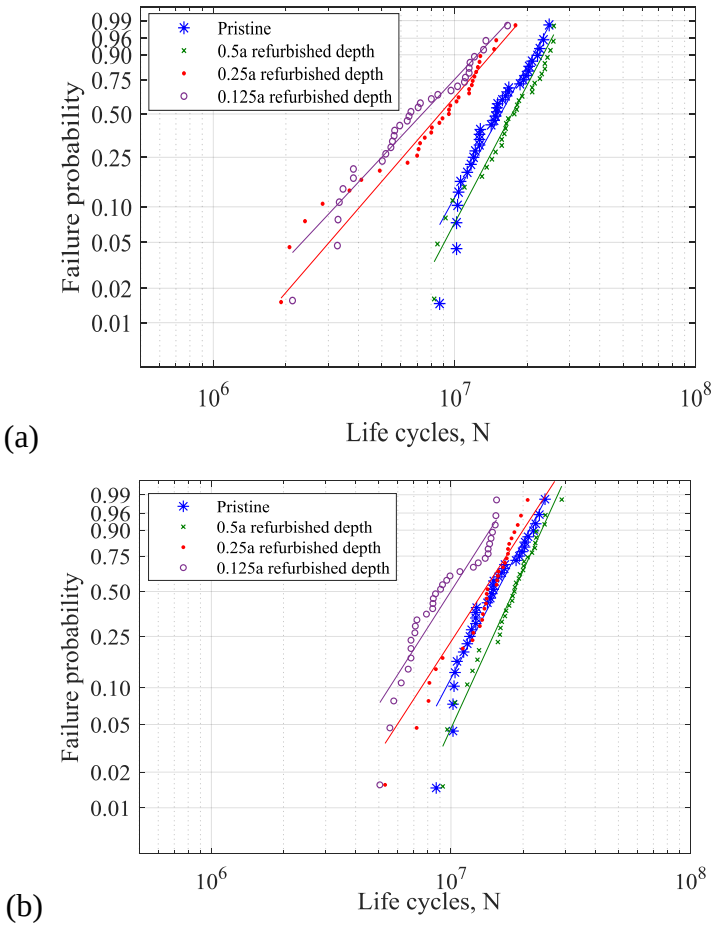

Figure 5.8: Fatigue life of pristine and refurbished domains at 3GPa with running time of (a) 90% L_{10} cycles before refurbishing (b) 50% L_{10} cycles before refurbishing

Figure 5.9 indicates the crack profile of pristine and refurbished conditions of the various cases at y=0 under 2GPa for the same microstructure domain. It can be observed that the cracks profile of refurbished domains at both initial fatigue cycles, 50% and 90% of $L_{10pristine}$, are similar. Therefore, the amount of initial damages in refurbished domains have only significant effects on fatigue life. Furthermore, crack shapes of refurbished domains with the grinding depth of 6μm (0.125*a*) is nearly close to the cracks below of grinding line at 6μm in the pristine domain. The

reason is that shallow grinding depth did not change the location of critical depth dreadfully. Moreover, in this case, the refurbished domain preserved most of the damage value similar to pristine domains as shown in Figure 5.6. However, by increasing the refurbished depth, new grain microstructures of the refurbished domain were subjected to shear stress reversal. Therefore, the crack initiation and propagation of the refurbished domain with 12.5 and 25μm grinding depths are not the same as the pristine domain and they behaved as new microstructure domains.

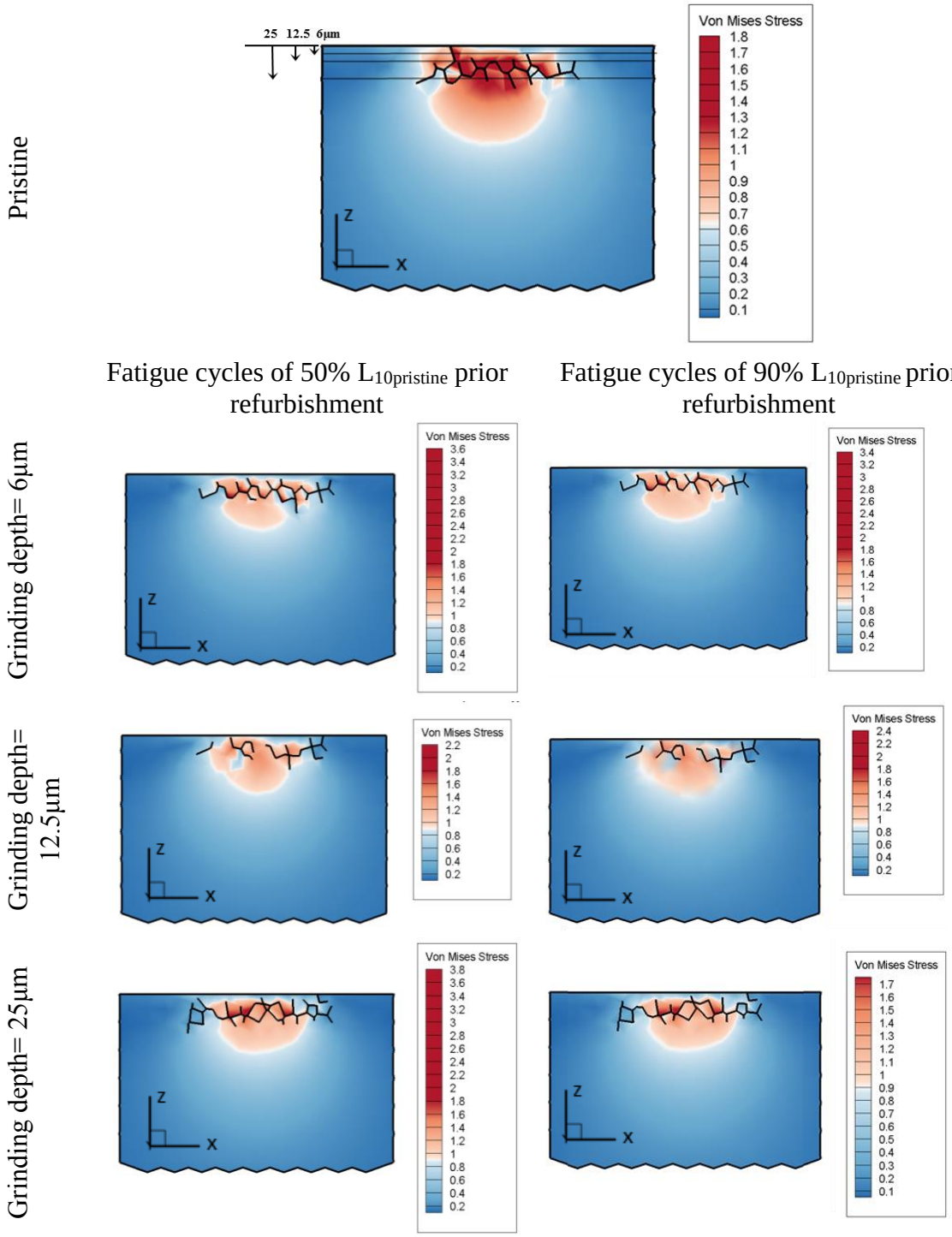

Figure 5.9: Final pattern of Crack profile of one domain in pristine and refurbished conditions at y =0 with different grinding depths under different fatigue cycles before refurbishment at P_{max} =2 GPa

5.4 Summary and Conclusions

This study presents a 3D finite element model to evaluate the RCF lives and spall formations of refurbished AISI 52100 through hardened steel in a circular contact. Continuum damage mechanics was used in this FE model to simulate the progressive degradation of a material due to fatigue damage. In order to capture the fatigue life variations due to the randomness of material microstructure, Voronoi tessellations were implemented in this simulation. Refurbishing process was simulated by passing a surface at different depths (0.125a, 0.25a and 0.5a) through Voronoi domains and removing material microstructure above the cut surface while the damage values due to the fatigue cycles before refurbishing were retained in the rest of the domain below the cut surface. Then, the refurbished domains were subjected to the RCF loading until a crack reached the surface designated as a final failure. A parametric study was conducted to investigate the performance of fatigue behavior of refurbished domains under various grinding depths, fatigue cycles prior to refurbishing, and applied loads. The numerical results demonstrated that refurbishment enhanced the estimated useful life for various scenarios. It is found that the greater grinding depths improved RCF life due to removing more damaged materials from domains. Furthermore, the remaining useful lives of refurbished domains were longer with lower initial fatigue cycles (50% of $L_{10pristine}$) since a small amount of damage was retained in domains before refurbishing. Although the total lives of restored domains were greater at higher initial fatigue cycles (90% of $L_{10pristine}$). These results are qualitatively consistent with previously proposed refurbishing models. Moreover, the life extension decreased at higher loads. Additionally, crack profiles of refurbished domains with higher grinding depths are completely different from original domains since new material microstructures below the regrind surface were exposed to RCF loading. Consequently, a method that can extend the life expectancy of through hardened ball bearings is a well-designed refurbishment process. Based on this investigation, the perfect refurbishing approach in a circular contact is to regrind the surface with a minimum depth of 0.35a and closer to the L_{10} life.

6. SUMMARY, CONCLUSION AND RECOMMENDATIONS FOR FUTURE RESEARCH

6.1 Summary and Conclusions

In chapter two, a coupled multibody elastic-plastic finite element (FE) model was developed to investigate the effects of surface defects, such as dents on rolling contact fatigue (RCF). The coupled Voronoi FE model was used to determine the contact pressure acting over the surface defect, internal stresses, damage, etc. In order to determine the shape of a dent and material pile up during the over rolling process, a rigid indenter was pressed against an elastic plastic semi-infinite domain. Continuum damage mechanics (CDM) was used to account for material degradation during RCF. Using CDM, spall initiation and propagation in a line contact was modelled and investigated. A parametric study using the model was performed to examine the effects of dent sharpness, pile up ratio and applied load on the spall formation and fatigue life. The spall patterns were found to be consistent with experimental observations from the open literature. Moreover, the results demonstrated that the dent shape and sharpness had a significant effect on pressure and thus fatigue life. Higher dent sharpness ratios significantly reduced the fatigue life.

In chapter three, the effects of refurbishing on rolling contact fatigue (RCF) in case carburized AISI 8620 steel were experimentally and analytically investigated. A thrust bearing test apparatus (TBTA) was designed and developed to simulate RCF. Initial RCF tests were conducted on AISI 8620 steel specimens to determine the baseline for pristine. Then new specimens were exposed to fatigue cycles equal to 90% of the L_{10} life of the pristine material. These specimens were then refurbished to the depths of 0.13b and 1.27b (b is the half width of Hertzian contact). The refurbished specimens were then subjected to RCF cycles in the TBTA until a spall appeared on the surface. The experimental results of refurbished specimens indicated a significant amount of fatigue life after refurbishing for both grinding depths. Moreover, it was observed that the remaining useful life of the refurbished test specimens was extended by increasing the depth of the regrinding.

For the analytical investigation, a two-dimensional elastic-plastic finite element model was developed to estimate RCF life for pristine and refurbished specimens of case carburized steel.

The characteristics of case carburized materials (e.g., variations in hardness and residual stresses) were incorporated in the 2D finite element model. In the present study, a continuum damage mechanics approach was employed to determine fatigue damage accumulation in original and refurbished domains. The results obtained from the experimental and FEA models for pristine and refurbished case carburized steel are in good agreement for both grinding depths.

In chapter four, the objectives of this investigation were to develop a 3D efficient elastic-plastic finite element model to characterize the rolling contact fatigue behavior of through hardened steel at high loads (~5 GPa) and to corroborate analytical and experimental results. The efficient FE model developed for this investigation was coupled with the continuum damage mechanics to simulate rolling contact fatigue (RCF). The new computationally efficient approach developed uses Delaunay mesh to reduce the number of elements without compromising the accuracy of stress distribution induced during a rolling contact pass. In order to validate the newly developed approach, the results obtained from the current 3D model for line contact were corroborated to previously published results. The fatigue lives obtained from the new model are consistent with the previously published model predictions and empirical observations. In order to simulate the RCF for high load conditions, the increase in the contact width observed in the experiments and consequently the decrease in the contact pressure with loading cycles were implemented in the model. Furthermore, the damage evolution law was modified to incorporate the compressive residual stresses induced by the plastic deformation. The L_{10} life and the scatter in the fatigue lives obtained from the model correlated well with the experimental results. As a part of this investigation, a Thrust Bearing Test Apparatus (TBTA) was used to simulate RCF. RCF experiments were conducted on through hardened AISI 52100 steel flat specimens at high contact stress levels (5 GPa) to induce plastic deformation. The results demonstrated that the contact width increased as the cycles increased due to plastic strain accumulation. The results from FE model corroborate well with experimental results obtained from TBTA.

In chapter five, a three-dimensional finite element (FE) model was developed to investigate the effects of refurbishing on rolling contact fatigue (RCF) behavior of through hardened bearing steel in a circular contact. In this investigation, the material degradation due to fatigue in original and refurbished domains was modeled using the continuum damage mechanics (CDM). Material damage, crack initiation and propagation in a circular contact are modeled to estimate the fatigue life of original and refurbished domains using CDM. RCF lives of pristine domains were predicted

to define the baseline for the through-hardened steel. Then, a layer of material was removed to simulate the refurbishment while the accumulated damage for a set number of contact cycles is preserved in the domain. The refurbished domains are subjected to RCF cycles using the 3D FEM model until a crack reached the surface indicating final life. A parametric study was conducted to evaluate the influence of material removal depth, loading cycles before refurbishing, the applied load on the RCF life and the spall formation in the circular contact. The model results demonstrated that refurbishing increased the fatigue life. Higher fatigue cycles before refurbishing and greater regrinding depth enhanced the total fatigue life. Furthermore, as expected, increasing the applied load reduced the fatigue life extension of restored domains.

6.2 Recommendations for Future Research

The fatigue damage models for surface and subsurface failures developed in this dissertation have indicated an excellent capacity for estimating the rolling contact fatigue behavior of REBs by taking into account the microstructure topology, contact configuration and the mechanical properties of the material. Simulating all aspect of reality is challenging, therefore; these models had some simplifying assumptions which were crucial to developing a computationally feasible modeling approach. Some of the major assumptions are homogenous, isotropic material and idealized Hertzian contact pressure. In reality, the pressure distribution between contacting bodies is determined by the body's geometry, speed, lubricant viscosity, applied load, temperature, surface roughness etc. Furthermore, other factors such as material degradation due to fatigue, plastic strain accumulations, crack propagation change the pressure profile during the time. These variations, in some cases, can considerably influence the state of stress and strains in the material causing a significant change in fatigue lives of REBs. Hence, there is a great opportunity to enhance the fatigue damage models stated in this dissertation in order to achieve an accurate tool to predict the fatigue failure of machine components.

6.2.1 A Coupled Multibody 3D FE Model to Study RCF under High Applied Loads

The importance of contact area variations due to plastic deformation under high applied loads was described in Chapter 4. In that chapter, the variations of contact width observed in RCF experiments as shown in Figure 6.1 and the corresponding calculated contact pressure during fatigue cycles were implemented in the 3D FE simulation in order to predict the RCF life under

high loading conditions. One of the limitations of the developed model is the dependency of numerical analysis on the experimental results. Further, the profile of contact pressure was assumed Hertzian which is not applicable when the surfaces plastically deform. In order to avoid these limitations, a coupled multibody 3D elastic-plastic FE model can be developed to obtain the contact variations due to plastic deformation in RCF at high applied loads. The 3D multibody model may consist of two bodies in contact, the ball and the raceway in rolling element bearings. The coupled FE model can then be used to determine accurately the contact pressure profile and the plastic strains accumulation over the rolling process to capture the variation of contact configurations during loading cycles. The calculated stresses and strains can be employed in the fatigue model to predict RCF life under high loads using CDM. This model can also be used to study the effects of surface defects, material defects, inclusion sizes, and refurbishing process on rolling contact fatigue [155] under high applied loads.

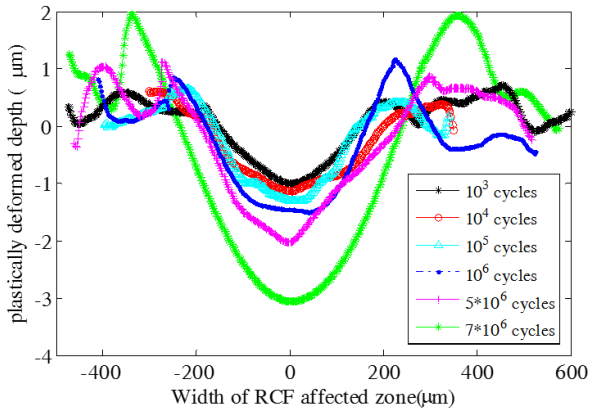

Figure 6.1: Experimental RCF track profile at different test cycles

6.2.2 Dynamic analysis of RCF with the effects of surface defects

As explained in Chapter 1, one of the dominant failure modes of rolling contact fatigue is the surface-initiated failure. The primary cause of surface-initiated fatigue cracks in rolling element bearings is surface defects. More than 90 percent of all bearing failures result from discrete surface discontinuities such as scratches and dents [109]. The initiated surface cracks propagate to form macro cracks and to generate large surface defects generally referred to as spalls. Therefore, it is essential to investigate this failure and its influence on RCF. In Chapter 2, the effects of surface defects on rolling contact fatigue were studied using the developed coupled 2D

elastic-plastic FE model. In that study, the simulation was assumed in a quasi-statics condition which simplified the analyses in order to obtain a fundamental understanding of the model. However, these surface defects bring dynamic instabilities in the region where the ball or roller is in contact with the surface dent profile [156]. When a rolling element rotates over the dented surface, it leaves the surface due to the dent pile up then it impacts the surface in the other side of the dent profile. Therefore, it is important to consider the effects of the dynamic contact force as depicted in Figure 6.2 on the RCF with the effects of surface defects. Further, the dynamic effects cause the spall to form in a specific distance from the dent shoulder as experimentally observed in Figure 6.3 [50]. Therefore, the developed model in Chapter 2 can be extended to include the dynamic effects of ball motion over the dented surface in order to predict the fatigue life and spall formation accurately. Moreover, the effects of different speed and various slide to roll ratio can be studied using this model.

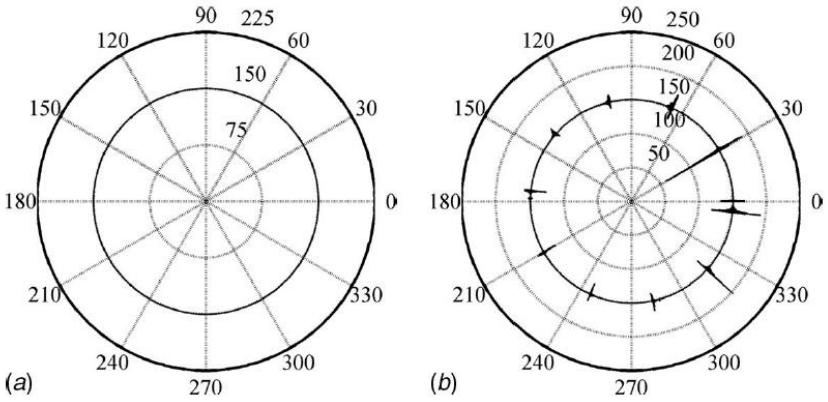

Figure 6.2: Contact force (N, radial axis) between ball-race at angle (deg) about bearing axis: a) without dent; b) with dent [156]

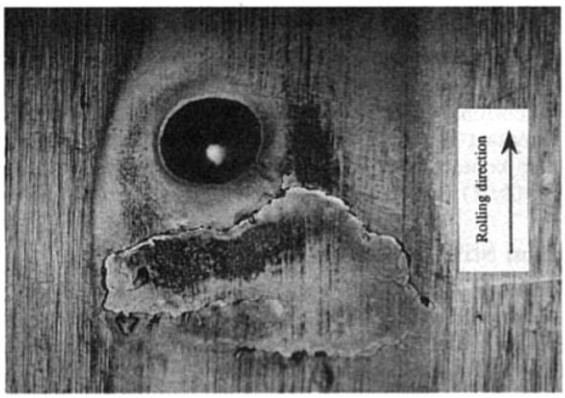

Figure 6.3: Experimental result for a dent-initiated spall in a dry contact [50]

REFERENCES

[1] Littmann WE. The Mechanism of Contact Fatigue. NASA Spec Report, SP-237 n.d.

[2] Littmann WE, Widner RL. Propagation of Contact Fatigue from Surface and Subsurface Origins. J Basic Eng 1966;88:624–36.

[3] Sadananda K, Ramaswamy D-N V. Role of crack tip plasticity in fatigue crack growth. Philos Mag A 2001;81:1283–303.

[4] Lou B, Han L, Lu Z, Liu S, Shen F. The rolling contact fatigue behaviors in carburized and hardened steel. Fatigue 90 Proc. Fourth Int. Conf. Fatigue Fatigue Threshold., 1990, p. 627–32.

[5] Nelias D, Ville F. Detrimental effects of debris dents on rolling contact fatigue. J Tribol 2000;122:55–64.

[6] Bower AF. The Influence of Crack Face Friction and Trapped Fluid on Surface Initiated Rolling Contact Fatigue Cracks. J Tribol 1988;110:704. doi:10.1115/1.3261717.

[7] Johnson KL, Johnson KL. Contact mechanics. Cambridge university press; 1987.

[8] Fitzsimmons B, Clevenger HD. Contaminated lubricants and tapered roller bearing wear. ASLE Trans 1977;20:97–107.

[9] Perrotto J. Effect of abrasive contamination on ball bearing performance. 34 th Annu. Meet., 1979, p. 1979.

[10] Loewenthal SH, Moyer DW. Filtration effects on ball bearing life and condition in a contaminated lubricant. J Lubr Technol 1979;101:171–6.

[11] Needelman WM. Filtration for wear control. Chapter ASME Wear Control Handbook, ASME Press New-York 1980:507–82.

[12] Loewenthal SH, Moyer DW, Needelman WM. Effects of ultra-clean and centrifugal filtration on rolling-element bearing life. J Lubr Technol 1982;104:283–91.

[13] Ioannides E, Beghini E, Bergling G, Goodall J. Cleanliness and its importance for bearing performance. Ball Bear J 1993:8–15.

[14] Webster MN, Ioannides E, Saules RS. The effect of topographical defects on the contact stress and fatigue life in rolling element bearings. Mech Surf Distress Glob Stud Mech Local Anal Surf Distress Phenom 1985:207–21.

[15] Sayles RS, Ioannides E. Debris damage in rolling bearings and its effects on fatigue life. J Tribol 1988;110:26–31.

[16] Tallian TE. Prediction of rolling contact fatigue life in contaminated lubricant: Part II-Experimental. J Lubr Technol 1976;98:384–92.

[17] Lorosch H-K. Research on longer life for rolling-element bearings. Lubr Eng 1985;41:37–43.

[18] Ai X. Effect of debris contamination on the fatigue life of roller bearings. Proc Inst Mech Eng Part J J Eng Tribol 2001;215:563–75.

[19] Ai X, Nixon HP. Fatigue life reduction of roller bearings due to debris denting: Part I-Theoretical modeling. Tribol Trans 2000;43:197–204.

[20] Vieillard C, Kadin Y, Morales-Espejel GE, Gabelli A. An experimental and theoretical study of surface rolling contact fatigue damage progression in hybrid bearings with artificial dents. Wear 2016;364:211–23.

[21] Makino T, Neishi Y, Shiozawa D, Kikuchi S, Okada S, Kajiwara K, et al. Effect of defect shape on rolling contact fatigue crack initiation and propagation in high strength steel. Int J Fatigue 2016;92:507–16.

[22] Matsunaga H, Komata H, Yamabe J, Fukushima Y, Matsuoka S. Effect of size and depth of small defect on the rolling contact fatigue strength of bearing steel JIS-SUJ2. Procedia Mater Sci 2014;3:1663–8.

[23] Da Mota V, Moreira P, Ferreira LAA. A study on the effects of dented surfaces on rolling contact fatigue. Int J Fatigue 2008;30:1997–2008.

[24] Gao N, Dwyer-Joyce RS, Beynon JH. Effects of surface defects on rolling contact fatigue of 60/40 brass. Wear 1999;225:983–94.

[25] Nelias D, Jacq C, Lormand G, Dudragne G, Vincent A. New methodology to evaluate the rolling contact fatigue performance of bearing steels with surface dents: application to 32CrMoV13 (nitrided) and M50 steels. J Tribol 2005;127:611–22.

[26] Tallian TE. The Failure Atlas For Hertz Contact Machine Elements. Mech Eng 1992;114:66.

[27] Ueda T, Mitamura N. Mechanism of dent initiated flaking and bearing life enhancement technology under contaminated lubrication condition: Part I: Effect of tangential force on dent initiated flaking. Tribol Int 2008;41:965–74.

[28] Dommarco RC, Bastias PC, Rubin CA, Hahn GT. The influence of material build up around artificial defects on rolling contact fatigue life and failure mechanism. Wear 2006;260:1317–23.

[29] Ville F, Nelias D. An Experimental Study on the Concentration and Shape of Dents Caused by Spherical Metallic Particles in EHL Contacts{\copyright}. Tribol Trans 1999;42:231–40.

[30] Coulon S, Jubault I, Lubrecht AA, Ville F, Vergne P. Pressure profiles measured within lubricated contacts in presence of dented surfaces. Comparison with numerical models. Tribol Int 2004;37:111–7.

[31] Kang YS, Sadeghi F, Hoeprich MR. A finite element model for spherical debris denting in heavily loaded contacts. J Tribol 2004;126:71–80.

[32] Nikas GK. A mechanistic model of spherical particle entrapment in elliptical contacts. Proc Inst Mech Eng Part J J Eng Tribol 2006;220:507–22.

[33] Lubrecht AA, Dwyer-Joyce RS, Ioannides E. Paper IV (iii) Analysis of the Influence of Indentations on Contact Life. Tribol. Ser., vol. 21, Elsevier; 1992, p. 173–81.

[34] Coulon S. Prediction of the lifetime of punctual contacts lubricated in the presence of indentations. Villeurbanne, INSA, 2001.

[35] Ai X, Lee SC. Effect of slide-to-roll ratio on interior stresses around a dent in EHL contacts. Tribol Trans 1996;39:881–9.

[36] Ioannides E, Harris TA. A new fatigue life model for rolling bearings. J Tribol 1985;107:367–77.

[37] Ko CN, others. Debris denting-The associated residual stresses and their effect on the fatigue life of rolling bearing: An FEM analysis. Tribol. Ser., vol. 14, Elsevier; 1989, p. 199–207.

[38] Hamer JC, Sayles RS, Ioannides E. Particle deformation and counterface damage when relatively soft particles are squashed between hard anvils. Tribol Trans 1989;32:281–8.

[39] Lubrecht A. Surface Damage--Comparison of Theoretical and Experimental Endurance Lives of Rolling Bearings. Proc. Japan Int. Tribol. Conf., 1990, p. 185–90.

[40] Coulon S, Ville F, Lubrecht AA. An abacus for predicting the rolling contact fatigue life reduction due to debris dents. Tribol. Ser., vol. 40, Elsevier; 2002, p. 283–93.

[41] Biboulet N, Lubrecht AA, Houpert L. Contact pressure in indented elastohydrodynamic lubrication contacts. Proc Inst Mech Eng Part J J Eng Tribol 2008;222:415–21.

[42] Biboulet N, Houpert L, Lubrecht AA. Contact stress and rolling contact fatigue of indented contacts: Part I, numerical analysis. Proc Inst Mech Eng Part J J Eng Tribol 2013;227:310–8.

[43] Ai X, Cheng HS. The influence of moving dent on point EHL contacts. Tribol Trans 1994;37:323–35.

[44] Howell MB, Rubin CA, Hahn GT. The effect of dent size on the pressure distribution and failure location in dry point frictionless rolling contacts. J Tribol 2004;126:413–21.

[45] Lemaitre J. A Course on Damage Mechanics 1992.

[46] Chaboche J-L. Continuum damage mechanics: Part II—Damage growth, crack initiation, and crack growth. J Appl Mech 1988;55:65–72.

[47] Jalalahmadi B, Sadeghi F. A Voronoi FE fatigue damage model for life scatter in rolling contacts. J Tribol 2010;132:21404.

[48] Xiao Y-C, Li S, Gao Z. A continuum damage mechanics model for high cycle fatigue. Int J Fatigue 1998;20:503–8.

[49] Memon IR, Cui D, Zhang X. Fatigue life prediction of 3-D problems by damage mechanics-finite element additional load method. Fatigue'99 Seventh Int. Fatigue Congr., 1999, p. 827–32.

[50] Xu G, Sadeghi F, Hoeprich MR. Dent initiated spall formation in EHL rolling/sliding contact. J Tribol 1998;120:453–62.

[51] Xu G, Sadeghi F. Spall initiation and propagation due to debris denting. Wear 1996;201:106–16.

[52] Xu G, Sadeghi F, Cogdell JD. Debris denting effects on elastohydrodynamic lubricated contacts. J Tribol 1997;119:579–87.

[53] Miller KJ. A historical perspective of the important parameters of metal fatigue and problems for the next century. Proc. 7th Int. Fatigue Congr., 1999, p. 15–39.

[54] Warhadpande A, Sadeghi F. Effects of surface defects on rolling contact fatigue of heavily loaded lubricated contacts. Proc Inst Mech Eng Part J J Eng Tribol 2010;224:1061–77.

[55] Bower AF, Johnson KL. The influence of strain hardening on cumulative plastic deformation in rolling and sliding line contact. J Mech Phys Solids 1989;37:471–93.

[56] Johnson KL. The mechanics of plastic deformation of surface and subsurface layers in rolling and sliding contact. Key Eng. Mater., vol. 33, 1989, p. 17–34.

[57] Mura T, Nakasone Y. A theory of fatigue crack initiation in solids. J Appl Mech 1990;57:1.

[58] Cheng W, Cheng HS, Mura T, Keer LM. Micromechanics modeling of crack initiation under contact fatigue. J Tribol 1994;116:2–8.

[59] Sadeghi F, Jalalahmadi B, Slack T., Raje N, Arakere NK. A review of rolling contact fatigue. J Tribol 2009;131:041403.

[60] ISO 281: Rolling bearings — Dynamic load ratings and rating life. ISO Stand 2007;3. doi:10.5594/J09750.

[61] Lundberg G, Palmgren A. Dynamic Capacity of Roller Bearings. Acta Polytech Mech Eng Ser R Swedish Acad Eng Sci 1952;2:96–127.

[62] Lundberg G, Palmgren A. Dynamic capacity of rolling bearings. J Appl Mech ASME 1949;16:165–72.

[63] Chalsma J, Zaretsky E V. Design for life, plan for death. Mach Des 1994;66:57–9.

[64] Tallian TE. Simplified contact fatigue life prediction model—Part II: New model. ASME J Tribol 1992;114:214–22.

[65] Harris TA, McCool JI. On the accuracy of rolling bearing fatigue life prediction. Trans Soc Mech Eng J Tribol 1996;118:297–310.

[66] Keer, LM, Bryant M. A pitting model for rolling contact fatigue. ASME J Lubr Technol 1983;105:198–205.

[67] Bhargava V, Hahn G, Rubin C. Rolling contact deformation and microstructural changes in high strength bearing steel. Wear 1989.

[68] Vincent A, Lormand G, Lamagnere P, Gosset L, Girodin D, Dudragne G, et al. From white etching areas formed around inclusions to crack nucleation in bearing steels under rolling contact fatigue. Bear. steels into 21st century, ASTM International; 1998.

[69] Lormand G, Meynaud P, Vincent A, Baudry G, Girodin D, Dudragne G. From Cleanliness to Rolling Fatigue Life of Bearings—A New Approach. Bear. Steels Into 21st Century, ASTM International; 1998.

[70] Jiang Y, Sehitoglu H. A model for rolling contact failure. Wear 1999.

[71] Raje N, Sadeghi F, Rateick R. A numerical model for life scatter in rolling element bearings. J 2008.

[72] McDiarmid D. A general criterion for high cycle multiaxial fatigue failure. Fatigue Fract Eng Mater 1991.

[73] McDiarmid D. A shear stress based critical-plane criterion of multiaxial fatigue failure for design and life prediction. Int J Fatigue 1995.

[74] Susmel L, Lazzarin P. A bi- parametric Wöhler curve for high cycle multiaxial fatigue assessment. Fract Eng Mater … 2002.

[75] Raje N, Sadeghi F, Rateick RG. A statistical damage mechanics model for subsurface initiated spalling in rolling contacts. J Tribol 2008;130:42201.

[76] Jalalahmadi B, Sadeghi F. A Voronoi finite element study of fatigue life scatter in rolling contacts. J Tribol 2009;131.

[77] Weinzapfel N, Liebel A, Sadeghi F, Bakolas V. A 3D Finite Element Study of Fatigue Life Dispersion in Rolling Line Contacts. J Tribol 2011;133:042202–042202. doi:10.1115/1.4005000.

[78] Bomidi JAR, Weinzapfel N, Sadeghi F, Liebel A, Weber J. An Improved Approach for 3D Rolling Contact Fatigue Simulations with Microstructure Topology. Tribol Trans 2013;56:385–99. doi:10.1080/10402004.2012.754072.

[79] Warhadpande A, Sadeghi F, Kotzalas MN, Doll G. Effects of plasticity on subsurface initiated spalling in rolling contact fatigue. Int J Fatigue 2012;36:80–95. doi:10.1016/j.ijfatigue.2011.08.012.

[80] Bomidi JAR, Sadeghi F. Three-Dimensional Finite Element Elastic–Plastic Model for Subsurface Initiated Spalling in Rolling Contacts. J Tribol 2013;136:11402. doi:10.1115/1.4025841.

[81] Harris TA. Rolling Bearing Analysis. Wiley: New York; 2001.

[82] Mihailidis A, Retzepis J, Salpistis C, Panajiotidis K. Calculation of friction coefficient and temperature field of line contacts lubricated with a non-Newtonian fluid. Wear 1999;232:213–20.

[83] Mihallidis A, Salpistis C, Drivakos N, Panagiotidis K. Friction behavior of FVA reference mineral oils obtained by a newly designed two-disk test rig. Int. Conf. Power Transm., vol. 3, 2003.

[84] Okabe A. Spatial tessellations. Wiley Online Library; 1992.

[85] Mucklich F, Ohser J, Schneider G. The characterization of homogeneous polyhedral microstructures applying the spatial Poisson-Voronoi tesselation compared to the standard DIN 50601. Zeitschrift Fur Met 1997;88:27–32.

[86] Slack T, Sadeghi F. Cohesive zone modeling of intergranular fatigue damage in rolling contacts. Tribol Int 2011;44:797–804.

[87] Warhadpande A, Jalalahmadi B, Slack T, Sadeghi F. A new finite element fatigue modeling approach for life scatter in tensile steel specimens. Int J Fatigue 2010;32:685–97.

[88] Weinzapfel N, Sadeghi F. Numerical modeling of sub-surface initiated spalling in rolling contacts. Tribol Int 2013;59:210–21.

[89] Ahmadi A, Mirzaeifar R, Moghaddam NS, Turabi AS, Karaca HE, Elahinia M. Effect of manufacturing parameters on mechanical properties of 316L stainless steel parts fabricated by selective laser melting: A computational framework. Mater Des 2016;112:328–38.

[90] Ahmadi A, Sadeghi F. Experimental and numerical investigation of torsion fatigue of a nickel-based alloy at elevated temperature. Mater Sci Eng A 2019;751:263–70.

[91] Singh K, Sadeghi F, Correns M, Blass T. A microstructure based approach to model effects of surface roughness on tensile fatigue. Int J Fatigue 2019;129:105229.

[92] Weinzapfel N, Sadeghi F, Bakolas V. An approach for modeling material grain structure in investigations of Hertzian subsurface stresses and rolling contact fatigue. J Tribol 2010;132:41404.

[93] Walvekar AA, Sadeghi F. Rolling contact fatigue of case carburized steels. Int J Fatigue 2017;95:264–81.

[94] Ghosh A, Leonard B, Sadeghi F. A stress based damage mechanics model to simulate fretting wear of Hertzian line contact in partial slip. Wear 2013;307:87–99.

[95] Schlicht H, Schreiber E, Zwirlein O. Fatigue and failure mechanism of bearings. Fatigue Eng Mater Struct 1986;1:85–90.

[96] Harris TA, Yu WK. Lundberg-Palmgren fatigue theory: considerations of failure stress and stressed volume. J Tribol 1999;121:85–9.

[97] Shimizu S, Tsuchiya K, Tosha K. Probabilistic Stress-Life (PSN) Study on Bearing Steel Using Alternating Torsion Life Test. Tribol Trans 2009;52:807–16.

[98] Bull HL, Hanau H. Bearing restoration—A users viewpoint. Bear Restor by Grinding, H Hanau, Etal, Eds, USAAVS COM-TR-76-27, US Army Aviat Syst Command 1976:59–66.

[99] Hanau H. Restoration by Grinding of Aircraft Ball and Roller Bearings—A Manufacturer's Viewpoint. Bear Restor by Grind 1976:1–23.

[100] Parker RJ, Zaretsky E V, Chen SM. Evaluation of ball and roller bearings restored by grinding 1976.

[101] Alexander J. Bearing repair provides valuable alternative to bearing replacement for heavy industries. South Carolina Timken Ind Serv Cent 2011.

[102] Zaretsky E V, Branzai E V. Model Specification for Rework of Aircraft Engine, Power Transmission, and Accessory/Auxiliary Ball and Roller Bearings 2007.

[103] Bearing repair services offer a cost-effective alternative to expensive replacement. World Minim Equip 2009:48–50.

[104] Cunningham JS, Morgan MA. Review of aircraft bearing rejection criteria and causes. Lubr Eng 1979;35:435–41.

[105] Paulson NR, Evans NE, Bomidi JAR, Sadeghi F, Evans RD, Mistry KK. A finite element model for rolling contact fatigue of refurbished bearings. Tribol Int 2015;85:1–9.

[106] Kotzalas MN, Eckels MR. Repair as an option to extend bearing life and performance. SAE Trans 2007:276–84.

[107] Coy JJ, Zaretsky E V, Cowgill GR. Life analysis of restored and refurbished bearings 1977.

[108] Lundberg G, Palmgren A. Dynamic Capacity of Rolling Bearings. Acta Polytech Mech Eng Ser R Swedish Acad Eng Sci 1947;1:1–52.

[109] Zaretsky E V, Branzai E V. Effect of rolling bearing refurbishment and restoration on bearing life and reliability. Tribol Trans 2005;48:32–44.

[110] Zaretsky E V, Parker RJ, Anderson WJ. NASA Five-Ball Fatigue Tester—Over 20 Years of Research. Roll. Contact Fatigue Test. Bear. Steels, ASTM International; 1982.

[111] Walvekar AA, Morris D, Golmohammadi Z, Sadeghi F, Correns M. A Novel Modeling Approach to Simulate Rolling Contact Fatigue and Three-Dimensional Spalls. J Tribol 2018;140:31101.

[112] Slack T, Sadeghi F. Explicit finite element modeling of subsurface initiated spalling in rolling contacts. Tribol Int 2010;43:1693–702.

[113] Paulson NR, Golmohammadi Z, Walvekar AA, Sadeghi F, Mistry K. Rolling contact fatigue in refurbished case carburized bearings. Tribol Int 2017;115:348–64.

[114] Bomidi JAR, Weinzapfel N, Slack T, Moghaddam SM, Sadeghi F, Liebel A, et al. Experimental and numerical investigation of torsion fatigue of bearing steel. J Tribol 2013;135:31103.

[115] Erdogan M, Tekeli S. The effect of martensite particle size on tensile fracture of surface-carburised AISI 8620 steel with dual phase core microstructure. Mater Des 2002;23:597–604.

[116] Boyer H. Case hardening of steel. ASM Int 1987 1987:319.

[117] Klecka MA, Subhash G, Arakere NK. Microstructure--property relationships in M50-NiL and P675 case-hardened bearing steels. Tribol Trans 2013;56:1046–59.

[118] Branch NA, Subhash G, Arakere NK, Klecka MA. A new reverse analysis to determine the constitutive response of plastically graded case hardened bearing steels. Int J Solids Struct 2011;48:584–91.

[119] Choi IS, Dao M, Suresh S. Mechanics of indentation of plastically graded materials—I: Analysis. J Mech Phys Solids 2008;56:157–71.

[120] Cahoon JR. An improved equation relating hardness to ultimate strength. Metall Mater Trans B 1972;3:3040.

[121] Pavlina EJ, Van Tyne CJ. Correlation of yield strength and tensile strength with hardness for steels. J Mater Eng Perform 2008;17:888–93.

[122] Reti T. Residual stresses in carburized, carbonitrided, and case-hardened components. Handb Residual Stress Deform Steel 2002:189–208.

[123] Parrish G, Harper GS. Production Gas Carburising: The Pergamon Materials Engineering Practice Series. Elsevier; 2013.

[124] Chaboche JL. Continuum damage mechanics: Part I— general concepts. J Appl Mech 1988;55:59–64.

[125] Shen Y, Moghadam SM, Sadeghi F, Paulson K, Trice RW. Effect of retained austenite--compressive residual stresses on rolling contact fatigue life of carburized AISI 8620 steel. Int J Fatigue 2015;75:135–44.

[126] Harris TA, Kotzalas MN. Rolling Bearing Analysis: Essential Concepts of Bearing Technology, (2007) n.d.

[127] Budynas RG, Nisbett JK, others. Shigley's mechanical engineering design. vol. 8. McGraw-Hill New York; 2008.

[128] Moyar GJ, Sinclair GM. Cumulative plastic deformation in rolling contact. J Basic Eng 1963;85:105–12.

[129] Radhakrishnan VM, Ramanathan S. Plastic deformation in rolling contact. Wear 1975;32:211–21.

[130] Lorösch H-K. Influence of load on the magnitude of the life exponent for rolling bearings. Roll. contact fatigue Test. Bear. steels, ASTM International; 1982.

[131] Bhattacharyya A, Pandkar A, Subhash G, Arakere N. Cyclic constitutive response and effective S--N diagram of M50 NiL case-hardened bearing steel subjected to Rolling Contact Fatigue. J Tribol 2015;137:41102.

[132] Bhattacharyya A, Subhash G, Arakere N. Evolution of subsurface plastic zone due to rolling contact fatigue of M-50 NiL case hardened bearing steel. Int J Fatigue 2014;59:102–13.

[133] Donzella G, Gerosa R, Petrogalli C, Rivolta B, Silva G, Beretta M. Evaluation of the residual stresses induced by shot peening on some sintered steels. Procedia Eng 2011;10:3399–404.

[134] Merwin JE, Johnson KL. An analysis of plastic deformation in rolling contact. Proc Inst Mech Eng 1963;177:676–90.

[135] Warhadpande A, Sadeghi F, Evans RD, Kotzalas MN. Influence of plasticity-induced residual stresses on rolling contact fatigue. Tribol Trans 2012;55:422–37.

[136] Hahn GT, Bhargava V, Rubin CA, Chen Q, Kim K. Analysis of the rolling contact residual stresses and cyclic plastic deformation of SAE 52100 steel ball bearings. J Tribol 1987;109:618–26.

[137] Voskamp AP. Material response to rolling contact loading. ASME, Trans J Tribol 0742-4787) 1985;107:359–64.

[138] Voskamp AP, Österlund R, Becker PC, Vingsbo O. Gradual changes in residual stress and microstructure during contact fatigue in ball bearings. Met Technol 1980;7:14–21.

[139] Voskamp AP. Microstructural changes during rolling contract fatigue: Metal fatigue in the subsurface region of deep groove ball bearing inner rings 1997.

[140] Paulson NR, Bomidi JAR, Sadeghi F, Evans RD. Effects of crystal elasticity on rolling contact fatigue. Int J Fatigue 2014;61:67–75.

[141] Bijak-Żochowski M, Marek P. Residual stress in some elasto-plastic problems of rolling contact with friction. Int J Mech Sci 1997;39:15–32.

[142] Muro H, Tsushima N. Microstructural, microhardness and residual stress changes due to rolling contact. Wear 1970;15:309–30.

[143] Jackson R, Chusoipin I, Green I. A finite element study of the residual stress and deformation in hemispherical contacts. Trans ASME-F-Journal Tribol 2005;127:484–93.

[144] Walvekar AA, Paulson N, Sadeghi F, Weinzapfel N, Correns M, Dinkel M. A New Approach for Fatigue Damage Modeling of Subsurface-Initiated Spalling in Large Rolling Contacts. J Tribol 2017;139:11101.

[145] Barnsby RM. Life ratings for modern rolling bearings: a design guide for the application of international standard ISO 281/2. vol. 1. American Society of Mechanical Engineers; 2003.

[146] Golmohammadi Z, Sadeghi F, Walvekar A, Saei M, Mistry KK, Kang YS. Experimental and analytical investigation of effects of refurbishing on rolling contact fatigue. Wear 2017;392:190–201.

[147] Ito O, Fuller Jr ER. Computer modelling of anisotropic grain microstructure in two dimensions. Acta Metall Mater 1993;41:191–8.

[148] Espinosa HD, Zavattieri PD. A grain level model for the study of failure initiation and evolution in polycrystalline brittle materials. Part I: Theory and numerical implementation. Mech Mater 2003;35:333–64.

[149] Golmohammadi Z, Sadeghi F. A Coupled Multibody Finite Element Model for Investigating Effects of Surface Defects on Rolling Contact Fatigue. J Tribol 2019;141:41402.

[150] Ahmadi A, Moghaddam NS, Elahinia M, Karaca HE, Mirzaeifar R. Finite element modeling of selective laser melting 316l stainless steel parts for evaluating the mechanical properties. ASME 2016 11th Int. Manuf. Sci. Eng. Conf., 2016, p. V002T01A003--V002T01A003.

[151] Vijay A, Paulson N, Sadeghi F. A 3D finite element modelling of crystalline anisotropy in rolling contact fatigue. Int J Fatigue 2018;106:92–102.

[152] Golmohammadi Z, Walvekar A, Sadeghi F. A 3D efficient finite element model to simulate rolling contact fatigue under high loading conditions. Tribol Int 2018;126:258–69.

[153] Thoman DR, Bain LJ, Antler CE. Maximum likelihood estimation, exact confidence intervals for reliability, and tolerance limits in the Weibull distribution. Technometrics 1970;12:363–71.

[154] Harris TA, Barnsby RM. Life ratings for ball and roller bearings. Proc Inst Mech Eng Part J J Eng Tribol 2001;215:577–95.

[155] Golmohammadi Z, Sadeghi F. A 3D Finite Element Model for Investigating Effects of Refurbishing on Rolling Contact Fatigue. Tribol Trans 2019:1–14.

[156] Ashtekar A, Sadeghi F, Stacke L-E. A new approach to modeling surface defects in bearing dynamics simulations. J Tribol 2008;130:41103.